J. Fluid Mech. (1980), *vol.* 96, *part* 3, *pp.* 515–583
Printed in Great Britain

Convection in a compressible fluid with infinite Prandtl number

By GARY T. JARVIS† AND DAN P. McKENZIE

Department of Geodesy and Geophysics, University of Cambridge, Madingley Rise, Madingley Road, Cambridge CB3 0EZ

(Received 22 August 1978 and in revised form 6 April 1979)

An approximate set of equations is derived for a compressible liquid of infinite Prandtl number. These are referred to as the anelastic-liquid equations. The approximation requires the product of absolute temperature and volume coefficient of thermal expansion to be small compared to one. A single parameter defined as the ratio of the depth of the convecting layer, d, to the temperature scale height of the liquid, H_T, governs the importance of the non-Boussinesq effects of compressibility, viscous dissipation, variable adiabatic temperature gradients and non-hydrostatic pressure gradients. When $d/H_T \ll 1$ the Boussinesq equations result, but when d/H_T is $O(1)$ the non-Boussinesq terms become important. Using a time-dependent numerical model, the anelastic-liquid equations are solved in two dimensions and a systematic investigation of compressible convection is presented in which d/H_T is varied from 0·1 to 1·5. Both marginal stability and finite-amplitude convection are studied. For $d/H_T \leqslant 1{\cdot}0$ the effect of density variations is primarily geometric; descending parcels of liquid contract and ascending parcels expand, resulting in an increase in vorticity with depth. When $d/H_T > 1{\cdot}0$ the density stratification significantly stabilizes the lower regions of the marginal state solutions. At all values of $d/H_T \geqslant 0{\cdot}25$, an adiabatic temperature gradient proportional to temperature has a noticeable stabilizing effect on the lower regions. For $d/H_T \geqslant 0{\cdot}5$, marginal solutions are completely stabilized at the bottom of the layer and penetrative convection occurs for a finite range of supercritical Rayleigh numbers. In the finite-amplitude solutions adiabatic heating and cooling produces an isentropic central region. Viscous dissipation acts to redistribute buoyancy sources and intense frictional heating influences flow solutions locally in a time-dependent manner. The ratio of the total viscous heating in the convecting system, Φ, to the heat flux across the upper surface, F_u, has an upper limit equal to d/H_T. This limit is achieved at high Rayleigh numbers, when heating is entirely from below, and, for sufficiently large values of d/H_T, Φ/F_u is greater than 1·00.

1. Introduction

Since the early experiments of shallow layer convection by Bénard (1901) and the first theoretical description by Rayleigh (1916), the laminar flow of heated fluids has attracted both geophysical and astrophysical interest. In his marginal stability calculations Rayleigh made use of a set of assumptions, attributed to Boussinesq (1903, pp. 157–176), in which the thermodynamic parameters were taken to be

† Present address: Department of Physics, University of Toronto, Toronto, Ontario, Canada M5S 1A7.

0022–1120/80/4372–8270 $02.00

constant and the fluid was assumed incompressible, except when considering the body force term in the equation of motion; the buoyancy force due to thermal expansion of the fluid was retained as this force drives the flow. The use of these assumptions proved quite successful in early attempts to understand empirical marginal stability results (Rayleigh 1916; Jeffreys 1928, 1930; Low 1929; Schmidt & Milverton 1935; Schmidt & Saunders 1938; Pellew & Southwell 1940). Indeed the 'Boussinesq approximation' has since been employed in the vast majority of marginal stability and finite-amplitude convection studies.

Spiegel & Veronis (1960) gave criteria for the applicability of the Boussinesq approximation to compressible fluids. In particular for a compressible liquid in which convection extends over a depth range d, and in which adiabatic compression and decompression occur, the ratio of d to the temperature scale height, H_T, must be small compared to unity ($d/H_T \ll 1$). The scale height H_T represents the vertical distance over which a parcel of liquid must be moved in order to change its temperature by adiabatic expansion or compression by a factor of e and is defined as

$$H_T = C_p/g\alpha, \tag{1}$$

where C_p is the specific heat at constant pressure, g the gravitational acceleration and α the volume coefficient of thermal expansion. Mihaljan (1962) and Malkus (1964) developed rigorous mathematical justifications of the Boussinesq approximation, demonstrating that it is a self-consistent lowest-order approximation to the full equations of fluid flow. Malkus (1964), for example, performed a two-parameter expansion of the hydrodynamic equations and showed that the Boussinesq equations result when the two parameters $\Delta T^*/T_0$ and d/H_T are both small. (ΔT^* represents the temperature increase in excess of an adiabatic reference temperature and T_0 is a reference temperature.)

Although the Boussinesq approximation is valid for a number of physically interesting convecting systems, it is not applicable to studies of deep convection in, for example, planetary mantles, stellar interiors and the atmosphere. In such deep layers d is comparable to H_T and the influence of viscous dissipation, variable adiabatic temperature gradients and density gradients (effects of order d/H_T) may not be neglected. The basic hydrodynamic equations [(3)–(6) below] must be solved retaining all the relevant non-Boussinesq terms.

The Boussinesq condition on d/H_T was relaxed by Ogura & Phillips (1962) and Gough (1969) in their one-parameter expansions for deep gaseous layers. These expansions lead to the anelastic equations for a gas provided the relative potential temperature fluctuation (Ogura & Phillips 1962) or the square of the Mach number M (ratio of convective velocity to sound velocity) (Gough 1969) is small. In the anelastic approximation $\partial\rho/\partial t = 0$ (where ρ is density and t is time) and consequently acoustic modes do not exist. In the limit of shallow layers the anelastic-gas equations reduce to the Boussinesq equations.

In this paper we will consider an approximate set of equations for an infinite Prandtl number Newtonian fluid in which it is assumed that $d = O(H_T)$ and that $\alpha T \ll 1$, where T is the absolute temperature. (The Prandtl number is the ratio of the kinematic viscosity to the thermal diffusivity and gives a measure of the relative importance of viscous and inertial forces. For the Earth's mantle the Prandtl number is at least 10^{22}, essentially infinite.) In gases $\alpha \approx 1/T$ (where T is absolute temperature)

and hence αT is $O(1)$. The condition that αT be small thus restricts the application of this study to liquids and creeping solids for which α is generally small and only weakly dependent on T. For the liquids considered below, it can be shown that $M^2 \ll 1$ and accordingly elastic waves are ignored. The approximate set of equations derived in § 2 below is therefore referred to as the anelastic–liquid equations. These equations have the virtue of being simpler than the anelastic–gas equations and allow us to extend our understanding of finite-amplitude convection in infinite Prandtl number fluids into the compressible domain in a mathematically consistent manner.

Turcotte *et al.* (1974) included the non-Boussinesq effects of dissipative heating and adiabatic gradients in their study of incompressible steady-state convection. The effect of increasing d/H_T in their study was to reduce the vertical heat transport. This was attributed to the corresponding increase of the adiabatic gradient. We will show that, when all the non-Boussinesq effects are retained, the variation of the adiabatic gradient has the dominant effect on the solutions for $d/H_T \leqslant 1{\cdot}0$ but that density gradients become important when $d/H_T > 1{\cdot}0$.

The energetics of convection in compressible liquids were studied by Hewitt, McKenzie & Weiss (1975) and Backus (1975). These authors concluded that the ratio of the overall rate of viscous heating Φ to the total heat flux emerging from the system F_u is bounded above by the expression $(T_{\max} - T_{\min})/T_{\min}$, where $T_{\max}$ and $T_{\min}$ are the maximum and minimum temperatures in the system. Hewitt *et al.* (1975) showed further that the ratio Φ/F_u is independent of Rayleigh number and proportional to d/H_T. [The Rayleigh number is the dimensionless parameter defined in (50) below.] Hence for $T_{\max} > 2T_{\min}$, or $d/H_T > 1$, Φ may be greater than F_u. Although Φ/F_u may be regarded as the efficiency of conversion of heat into mechanical energy within the convecting layer (Malkus 1973), the heat generated by dissipation remains within the system and Φ/F_u is therefore not constrained by thermodynamic efficiency considerations to be less than unity. Hewitt *et al.* (1975) derived the following relation for a vigorously convecting system in which most of the heat is carried by convection:

$$E = \Phi/F_u \doteqdot (d/H_T)[1 - \tfrac{1}{2}r], \tag{2}$$

where r is the ratio of heat generated by internal heat sources to the total flux through the layer. When heating is entirely from below, $E \doteqdot d/H_T$. Equation (2) was verified by Hewitt *et al.* in the Boussinesq limit of $d/H_T = 0{\cdot}117$ by numerical calculations for a Newtonian fluid with infinite Prandtl number. That this result continues to hold true in the range $d = O(H_T)$ will be demonstrated in this paper.

In the geophysical context, lower-mantle or mantle-wide convection would occur with a value of $d/H_T \doteqdot 0{\cdot}5$ if the scale height H_T did not vary significantly with depth. When phase changes in the upper mantle occur, adiabatic temperature and mean density distributions experience abrupt changes in gradient and the locally defined scale height also changes, primarily due to sudden variations in α. In such cases a mean scale height can be determined from the total change in density across the layer of interest. Taking values of density equal to 3·3 g/cm^3 at the top of the mantle, 4·4 g/cm^3 at 700 km depth and 5·5 g/cm^3 at the core–mantle boundary (Press 1970) and using the definition of an adiabatic–hydrostatic density distribution given in (15) below, mean values of d/H_T are 0·3 for upper-mantle convection (0–700 km) and 0·6 for mantle-wide convection. However, uncertainties in the values and variations

of the physical parameters of the deep mantle are sufficiently large to preclude the usefulness of detailed Earth modelling. A general study of compressible convection in an infinite Prandtl number fluid is likely to be more profitable; general aspects of the physics of compressible flow thus revealed might then be applied in theoretical interpretation and speculation. The latter approach has been taken in this study.

A two-dimensional time-dependent numerical model has been developed for infinite Prandtl number Newtonian fluids in order to investigate the effects of compressibility, viscous dissipation, adiabatic heating and non-hydrostatic pressure gradients on the flow, energetics and stability of deep convecting layers. This model represents a further development of that described by McKenzie, Roberts & Weiss (1974) for incompressible liquids. Comparisons between results of the compressible and incompressible models will be made to illustrate the effects of increasing the value of d/H_T. The approximations and assumptions involved in the mathematical formulation of the compressible problem are outlined in the following section. A linear stability analysis of the governing equations is then briefly discussed in § 3 and results of the nonlinear finite-amplitude modelling are presented in § 4 for the range of values $0{\cdot}1 \leqslant d/H_T \leqslant 1{\cdot}5$.

2. Mathematical formulation

The relevant equations describing time-dependent laminar convection derive from the principles of conservation of mass, momentum and energy. These may be written as

$$\frac{\partial \rho}{\partial t} + \nabla . (\rho \mathbf{u}) = 0, \tag{3}$$

$$\rho \left(\frac{\partial \mathbf{u}}{\partial t} + \mathbf{u} . \nabla \mathbf{u} \right) = -\nabla P + \rho \mathbf{g} + \frac{\partial}{\partial x_j} \tau_{ij}, \tag{4}$$

$$\rho C_p \left\{ \frac{\partial T}{\partial t} - \frac{\alpha T}{\rho C_p} \frac{\partial P}{\partial t} + \mathbf{u} . [\nabla T - (\nabla T)_s] \right\} = \nabla . (K \nabla T) + H + \tau_{ij} \frac{\partial u_i}{\partial x_j}, \tag{5}$$

where ρ is the density, t time, $\mathbf{u}$ the velocity vector, P pressure, τ_{ij} the deviatoric stress tensor, $(\nabla T)_s$ the adiabatic temperature gradient, K thermal conductivity and H the rate of internal heat generation. Summation over repeated indices is implied in the terms involving the stress tensor. The term $(\nabla T)_s$ in (5) is given by

$$(\nabla T)_s = \frac{\alpha T}{\rho C_p} \nabla P. \tag{6}$$

Equations (3)–(5) must be supplemented with an equation of state, usually of the form

$$\rho = \rho(T, P). \tag{7}$$

In a Newtonian fluid, the deviatoric stress tensor τ_{ij} is related to the velocity field through the dynamic viscosity η, and 'second' or 'bulk' viscosity η_2, as

$$\tau_{ij} = \eta \left(\frac{\partial u_i}{\partial x_j} + \frac{\partial u_j}{\partial x_i} - \tfrac{2}{3} \delta_{ij} \frac{\partial u_k}{\partial x_k} \right) + \eta_2 \delta_{ij} \frac{\partial u_k}{\partial x_k}. \tag{8}$$

The bulk viscosity, associated with rapid changes in volume, depends on the relative

rates of volume change and molecular relaxation processes (Landau & Lifshitz 1959). Since volume changes in mantle convection occur over times greater than 10^7 years, η_2 is assumed to be unimportant and the last term in (8) is ignored. For infinite Prandtl number fluids, inertial forces are ignored and the left-hand side of (4) vanishes. Substituting from (8), (4) may therefore be written as

$$0 = -\nabla P + \rho \mathbf{g} + \frac{\partial}{\partial x_i}\eta\left(\frac{\partial u_i}{\partial x_j}+\frac{\partial u_j}{\partial x_i}\right) - \tfrac{2}{3}\nabla\eta(\nabla.\mathbf{u}). \tag{9}$$

The fluids considered in this study have the following physical and thermodynamic parameters assumed constant throughout: g, C_p, α, K, η (defined above) and Γ (Gruneisen's parameter). The latter is defined as

$$\Gamma = \frac{\alpha K_s}{\rho C_p} = \frac{\alpha K_T}{\rho C_v}, \tag{10}$$

where K_s and K_T are the isentropic and isothermal moduli of bulk compressibility and C_v is the specific heat at constant volume. These assumptions are made to simplify the mathematics and to reduce the number of variables of the problem. Since $\eta = \rho\nu$ (where ν is the kinematic viscosity) and ρ varies, either η or ν or both must also vary. Choosing η to be constant allows a simple expansion of the viscous force term in (9) and determines ν as η/ρ. For most liquids, Γ is approximately constant and of order 1. Assuming Γ to be constant eliminates the bulk moduli as independent parameters.

A reference state with hydrostatic pressure, P_H, and adiabatic temperature distribution T_s, is considered. Provided that fluid motions cause only small departures from this reference state, the equation of state may be written as a linear Taylor expansion of ρ about the reference state density distribution ρ_r as

$$\rho(T,P) = \rho_r[1-\alpha(T-T_s)+K_T^{-1}(P-P_H)], \tag{11}$$

where $\alpha = \rho_r^{-1}(\partial\rho_r/\partial T)_P$, and $K_T = \rho_r(\partial P/\partial\rho_r)_T$. An expression for the reference density distribution ρ_r is readily derived by considering the gradient of $\rho_r(S,P_H)$, S being the entropy per unit mass:

$$\nabla\rho_r(S,P_H) = \left(\frac{\partial\rho_r}{\partial S}\right)_{P_H}\nabla S + \left(\frac{\partial\rho_r}{\partial P_H}\right)_S \nabla P_H. \tag{12}$$

Since the reference state is adiabatic $\nabla S = 0$, and since $\nabla P_H = (0, 0, -\rho_r g)$, (12) reduces to

$$\frac{1}{\rho_r}\frac{d\rho_r}{dz} = -g\left(\frac{\partial\rho_r}{\partial P_H}\right)_S = -g\rho_r/K_s. \tag{13}$$

Using (10), (13) may be written as

$$\frac{1}{\rho_r}\frac{d\rho_r}{dz} = -\frac{g\alpha}{\Gamma C_p} = -\frac{1}{H_T\Gamma}, \tag{14}$$

which expresses the well-known Adams–Williamson relation for a chemically homogeneous adiabatic density distribution under hydrostatic pressure (Birch 1952). Since Γ is assumed constant, (14) may be integrated over z to give

$$\rho_r(z) = \rho_0 \exp(d-z)/H_T\Gamma, \tag{15}$$

where $\rho_0 = \rho_r(z = d)$ is the value of ρ_r at the upper surface. Substitution of (15) into (11) gives the equation of state

$$\rho(T, P) = \rho_0 \exp[(d-z)/H_T \Gamma][1 - \alpha(T - T_s) + K_T^{-1} P_1], \tag{16}$$

where $P_1 = P - P_H$.

2.1. *Dimensionless variables*

For ease of numerical manipulation, all physical variables are converted into dimensionless form. Following the approach of McKenzie *et al.* (1974), characteristic values of depth, temperature, density, velocity and time [d, $T_1 = 1/\mathrm{K}$, ρ_0, $U = g\alpha T_1 d^2/\nu_0$ (where $\nu_0 = \eta/\rho_0$ is the value of ν at the upper surface) and $\tau = d/U$ respectively] were chosen and all variables were expressed in terms of these units. The resulting dimensionless (primed) variables are

$$\left.\begin{aligned} (x', z') = (x, z)/d, \quad \rho_r' = \rho_r/\rho_0 = \exp[(1-z')D/\Gamma], \quad \rho' = \rho/\rho_0, \\ T' = (T - T_0)/T_1, \quad t' = t/\tau, \quad P_1' = P_1 d/U\eta = P_1 \alpha T_1 \rho_0 g d, \end{aligned}\right\} \tag{17}$$

where $D = d/H_T$ and T_0 is the temperature of the upper boundary. The scaling of P_1 is derived by considering the horizontal component of (9) and comparing the non-hydrostatic pressure gradient and viscous force terms. The dimensionless thermal diffusivity, energy generation rate and box width are

$$\kappa_0' = \kappa_0 \nu_0/g\alpha T_1 d^3, \quad \epsilon_0' = \epsilon_0 \nu_0/g\alpha T_1^2 d, \quad \lambda = L/d, \tag{18}$$

where L is the dimensional box width and $\epsilon_0 = H/\rho_0 C_p$.

2.2. *The anelastic–liquid approximation*

All equations in this section will be expressed in terms of the dimensionless variables defined above, with primes suppressed. In this notation, the equation of state (16) becomes

$$\rho = \rho_r[1 - \mu(T - T_s) + \mu(\rho_0 g d/K_T) P_1], \tag{19}$$

where $\mu = \alpha T_1$. Thus to order μ, $\rho = \rho_r$ and (as in the Boussinesq approximation) for $\mu \ll 1$ slight deviations in ρ from the reference state value may be ignored, except in the body force term of the momentum equation, where the temperature and pressure dependence of ρ will be seen to provide the driving force for the flow. For simplicity we have chosen $T_1 = 1$ °K. In the geophysical case, $\alpha \approx 10^{-5}$ °K^{-1} for mantle-type materials and the condition $\mu \ll 1$ can therefore accommodate a large range of values of T_1. Using (10), K_T may be expressed in terms of Γ and (19) may be written as

$$\rho = \rho_r\{1 - \mu(T - T_s) + \mu(D/\rho_r \Gamma)[1 + \mu \Gamma T_0 \exp\{(1-z)D\}] P_1\}. \tag{20}$$

Elastic waves are eliminated from the hydrodynamic equations by setting $\partial\rho/\partial t = 0$ in (3). This is permissible when $M^2 \ll 1$. By balancing buoyancy and viscous forces, we obtain a characteristic velocity as $U = g\alpha T_1 d^2/\nu_0$, while the velocity of sound is given by $C = (1{\cdot}8 K_s/\rho)^{\frac{1}{2}} = (1{\cdot}8 C_p \Gamma/\alpha)^{\frac{1}{2}}$. Hence

$$M^2 = U^2/C^2 = (d/H_T)\mu R^*/(1{\cdot}8 Pr) = O(\mu Pr^{-1}) \ll 1,$$

where R^*, which has the form of a Rayleigh number, is the inverse of the dimensionless thermal diffusivity. The dimensionless continuity equation may therefore be written as

$$\nabla . \rho \mathbf{u} = 0. \tag{21}$$

Assuming $\mu \ll 1$, all terms of order μ compared to other terms in the same equation can be ignored. Hence, from (20), to order μ, $\nabla . \rho_r \mathbf{u} = 0$ or

$$\nabla . [\mathbf{u} \exp(-zD/\Gamma)] = 0. \tag{22}$$

Restricting the flow to the x, z plane, (22) shows that $\mathbf{u} \exp(-zD/\Gamma)$ is solenoidal and hence may be represented by a stream function ψ such that

$$\mathbf{u} \exp(-zD/\Gamma) = (-\partial\psi/\partial z, 0, \partial\psi/\partial x). \tag{23}$$

Thus from (23) we obtain the velocity as

$$\mathbf{u} = (u, 0, w) = \left(-e^{zD/\Gamma} \frac{\partial\psi}{\partial z}, 0, e^{zD/\Gamma} \frac{\partial\psi}{\partial x} \right), \tag{24}$$

where u and w are the x and z components respectively of $\mathbf{u}$.

The stream function ψ can be related to the vorticity field $\boldsymbol{\omega}$ through (24) since $\boldsymbol{\omega} = \nabla \times \mathbf{u}$. Thus, assuming that the velocity does not vary in the y direction, $\boldsymbol{\omega}$ has a y component only, ω, such that

$$\nabla^2\psi + (D/\Gamma)\, \partial\psi/\partial z = -\omega e^{-zD/\Gamma}. \tag{25}$$

Vorticity is related to the temperature and non-hydrostatic pressure by taking the curl of the (dimensionless) momentum equation and substituting from (20) for ρ; thus

$$\nabla^2\omega = \rho_r \frac{\partial T}{\partial x} - \frac{D}{\Gamma}(1 + \mu\Gamma T_0 e^{(1-z)D}) \frac{\partial P_1}{\partial x} \tag{26}$$

or, to order μ,

$$\nabla^2\omega = e^{(1-z)D/\Gamma} \frac{\partial T}{\partial x} - \frac{D}{\Gamma} \frac{\partial P_1}{\partial x}. \tag{27}$$

This equation is similar to its counterpart in the Boussinesq formulation, the differences being the non-hydrostatic pressure term and the scaling factor $\exp((1-z)D/\Gamma)$, which accounts for the hydrostatic compression of the liquid. From the x component of the momentum equation we have

$$\frac{\partial P_1}{\partial x} = \nabla^2 u + \frac{1}{3} \frac{D}{\Gamma} \frac{\partial w}{\partial x}, \tag{28}$$

which enables the pressure term in (27) to be eliminated; thus the vorticity equation becomes

$$\nabla^2\omega = e^{(1-z)D/\Gamma} \frac{\partial T}{\partial x} - \frac{D}{\Gamma} \left(\nabla^2 u + \frac{D}{3\Gamma} \frac{\partial w}{\partial x} \right). \tag{29}$$

In the thermal energy equation (5), the term $\partial P/\partial t$ may be written as $\partial P_1/\partial t$ since the hydrostatic component is time-independent, and the viscous dissipation term, $\tau_{ij} \partial u_i/\partial x_j$, can be expressed in terms of ψ through the use of (24) and the dimensionless form of (8); this yields the dimensionless energy equation

$$\rho \frac{\partial T}{\partial t} - \mu D T \frac{\partial P_1}{\partial t} = -\nabla . T\rho\mathbf{u} - \rho D(T + T_0) w + \mu D T \mathbf{u} . \nabla P_1 + \kappa_0 \nabla^2 T + \epsilon_0 + D e^{2zD/\Gamma} \times \left[\left(2 \frac{\partial^2\psi}{\partial x \partial z} + \frac{D}{\Gamma} \frac{\partial\psi}{\partial x} \right)^2 + \left(\frac{\partial^2\psi}{\partial x^2} - \frac{\partial^2\psi}{\partial z^2} - \frac{D}{\Gamma} \frac{\partial\psi}{\partial z} \right)^2 + \frac{1}{3} \left(\frac{D}{\Gamma} \frac{\partial\psi}{\partial x} \right)^2 \right] \tag{30}$$

or, to order μ,

$$e^{(1-z)D/\Gamma} \frac{\partial T}{\partial t} = -\nabla . [T e^{(1-z)D/\Gamma} \mathbf{u}] - D e^{(1-z)D/\Gamma} (T + T_0) w + \kappa_0 \nabla^2 T + \epsilon_0 + D e^{2zD/\Gamma} \times \left[\left(2 \frac{\partial^2\psi}{\partial x \partial z} + \frac{D}{\Gamma} \frac{\partial\psi}{\partial x} \right)^2 + \left(\frac{\partial^2\psi}{\partial x^2} - \frac{\partial^2\psi}{\partial z^2} - \frac{D}{\Gamma} \frac{\partial\psi}{\partial z} \right)^2 + \frac{1}{3} \left(\frac{D}{\Gamma} \frac{\partial\psi}{\partial x} \right)^2 \right]. \tag{31}$$

Anelastic–liquid equations ($\mu \ll 1$)	Boussinesq equations ($\mu, D \ll 1$)
(A1) $\nabla^2\omega = \rho_r \frac{\partial T}{\partial x} - \frac{D}{\Gamma}\left(\nabla^2 u + \frac{1}{3}\frac{D}{\Gamma}\frac{\partial w}{\partial x}\right)$	(B1) $\nabla^2\omega = \partial T/\partial x$
(A1a) $\rho_r = e^{(1-s)D/\Gamma}$	
(A2) $\nabla^2\psi + \frac{D}{\Gamma}\frac{\partial \psi}{\partial z} = -\omega e^{-sD/\Gamma}$	(B2) $\nabla^2\psi = -\omega$
(A3) $\rho_r \frac{\partial T}{\partial t} = -\nabla . T\rho_r \mathbf{u} - D\rho_r(T+T_d)\, w + \kappa_0 \nabla^2 T + \varepsilon_0 + \phi$	(B3) $\partial T/\partial t = -\nabla . T\mathbf{u} + \kappa_0 \nabla^2 T + \varepsilon_0$
(A3a) $\phi = De^{2sD/\Gamma}\left[\left(2\frac{\partial^2\psi}{\partial x \partial z} + \frac{D}{\Gamma}\frac{\partial \psi}{\partial x}\right)^2 + \left(\frac{\partial^2\psi}{\partial x^2} - \frac{\partial^2\psi}{\partial z^2} - \frac{D}{\Gamma}\frac{\partial \psi}{\partial z}\right)^2 + \frac{1}{3}\left(\frac{D}{\Gamma}\frac{\partial \psi}{\partial x}\right)^2\right]$	
(A4) $\mathbf{u} = e^{sD/\Gamma}(-\partial\psi/\partial z, 0, \partial\psi/\partial x)$ or $\nabla . \mathbf{u} = Dw/\Gamma$	(B4) $\mathbf{u} = (-\partial\psi/\partial z, 0, \partial\psi/\partial x)$ or $\nabla . \mathbf{u} = 0$

TABLE 1. A comparison of anelastic–liquid and Boussinesq equations

In the Boussinesq limit D approaches zero and (31) reduces to the expression for incompressible flow (Hewitt *et al.* 1975).

The coupled thermal energy and momentum equations (5) and (9) are now replaced by (25), (29) and (31) which together with (24), for given initial and boundary conditions, completely determine the velocity and temperature fields as functions of space and time. Thus when $\mu \ll 1$ non-hydrostatic pressure fluctuations are ignored everywhere except in the body force term in the equation of motion, wherein buoyancy is generated entirely by terms of order μ. Table 1 summarizes the equations derived above and juxtaposes the corresponding Boussinesq equations. In the limit of vanishingly small d/H_T, the anelastic–liquid equations reduce to the Boussinesq equations.

2.3. *Model boundary conditions*

'Free' horizontal boundaries are assumed (i.e. normal velocities and tangential stresses vanish) and ψ is assumed to be an odd function of x and periodic with period 2λ. This implies mirror symmetry about vertical planes at $x = 0, \pm\lambda, \pm 2\lambda$, etc. and the numerical calculations are therefore confined to the dimensionless rectangular region $0 \leqslant x \leqslant \lambda$ and $0 \leqslant z \leqslant 1$. The temperature at the upper boundary ($z = 1$) and the heat flux across the lower boundary ($z = 0$) are held constant. These conditions imply

$$\left.\begin{aligned} &\psi = 0, \quad \omega = 0 && \text{at} \quad z = 0, 1 && \text{and} \quad x = 0, \lambda, \\ &T = T_0 \text{ (a constant)} && \text{at} \quad z = 1, \\ &\frac{\partial T}{\partial x} = 0 && \text{at} \quad x = 0, \lambda, \\ &\frac{\partial T}{\partial z} = F \text{ (a constant)} && \text{at} \quad z = 0, \end{aligned}\right\} \tag{32}$$

where F is the dimensionless heat flux supplied to the base of the layer. In terms of dimensional variables (in parentheses) F is given by

$$F = -(F_b d)/(\kappa_0 \rho_0 C_p T_1), \tag{33}$$

where F_b is the dimensional flux across the bottom boundary.

The Nusselt number is usually defined as the ratio of the heat flux through the convecting system to the heat flux which would exist in a purely conducting state characterized by the same parameters. However, because of the constant flux bottom boundary condition, this definition always yields a value of unity. In this case it is the mean temperature of the layer, rather than the heat flux across it, which changes when convection begins. Accordingly we define a modified Nusselt number N as

$$N = \bar{T}_{\text{cond}}/\bar{T}, \tag{34}$$

where $\bar{T}_{\text{cond}}$ is the mean temperature which would exist in the absence of convection and $\bar{T}$ is the actual mean temperature. For conduction solutions (34) gives $N = 1{\cdot}0$.

3. The linear problem: onset of convection

The purpose of this section is to determine the conditions for marginal stability in a compressible liquid governed by the anelastic–liquid equations derived above. The results of this study can then be used as a test of the nonlinear solutions in the limit of weak convection.

Jeffreys (1926, 1928) extended Rayleigh's (1916) initial work on marginal stability and introduced a dimensionless number, now generally referred to as the Rayleigh number, which combines the relevant physical and geometrical variables:

$$R = g\alpha\beta d^4/(\kappa\nu), \tag{35}$$

where β is the magnitude of the temperature gradient across the layer. The critical value of this number, R_c, which must be exceeded before convection can occur, is independent of the fluid properties. Jeffreys (1930) also considered the marginal stability of compressible fluids. In particular he showed that if β is interpreted as the magnitude of the temperature gradient in excess of the adiabatic gradient, then the condition for the onset of convection in a compressible fluid is the same as in an incompressible fluid. This approach is useful in gases (Spiegel 1971; Graham 1975) for which $\alpha T \approx 1$ and the adiabatic gradient $-g/C_p$ is constant [see (6)]. However, when α is a constant (as in the present study), the adiabatic gradient is proportional to T and decreases in magnitude from bottom to top across the layer. Consequently the Rayleigh number is not uniquely defined for such a liquid layer. Furthermore $(\kappa\nu)^{-1} = \rho^2 C_p (K\eta)^{-1}$ and ρ varies across the layer. Choosing the mean density $\bar{\rho}$ as a representative value of ρ, we can simply define

$$R_0 = \frac{g\alpha\beta_0 d^4}{\kappa_0 \nu_0}\left(\frac{\bar{\rho}}{\rho_0}\right)^2, \tag{36}$$

where β_0 is the magnitude of the imposed temperature gradient. R_0 is a uniquely defined dimensionless parameter of the system and may be interpreted as a non-dimensional temperature gradient. It has the same form as the classical Rayleigh number and accounts for the density variation across the layer. It does not, however, give a true indication of the stability of the layer when compared to the usual value of the critical Rayleigh number (385 for the boundary conditions of this study).

In this section we will determine the critical values of R_0 for the onset of convection, for discrete values of the ratio d/H_T. Due to the stabilizing influence of the adiabatic gradients and the density stratification, we can expect the critical value of R_0 to increase with compressibility.

3.1. *Perturbation equations*

We consider small perturbations to a basic steady state and write

$$\left.\begin{aligned}\mathbf{u} &= \mathbf{u}_b + \mathbf{u}',\\ T &= T_b + T',\end{aligned}\right\} \tag{37}$$

where $\mathbf{u}'$ and T' are small quantities and the subscript b refers to the basic state. When the basic state corresponds to the conduction solution, we have

$$\left.\begin{aligned}\mathbf{u}_b &= (u_b, 0, w_b) = (0, 0, 0),\\ \kappa_0 d^2 T_b/dz^2 &= -\epsilon_0.\end{aligned}\right\} \tag{38}$$

Substituting (37) and (38) into the dimensionless energy, momentum and continuity equations, and linearizing with respect to the small quantities $\mathbf{u}'$ and T' yields

$$\rho\,\partial T'/\partial t = -\rho w'\,dT_b/dz - \rho D(T_b + T_0)\,w' + \kappa_0 \nabla^2 T', \tag{39}$$

$$\nabla^2 \omega' = \rho\frac{\partial T'}{\partial x} - \frac{D}{\Gamma}\left(\nabla^2 u' + \frac{1}{3}\frac{D}{\Gamma}\frac{\partial w'}{\partial x}\right), \tag{40}$$

$$\nabla . \mathbf{u}' = w' D/\Gamma, \tag{41}$$

where $\rho = \exp[(1-z)\,D/\Gamma]$, u' and w' are the x and z components of $\mathbf{u}'$ and we again use the notation $D = d/H_T$.

We represent the two-dimensional temperature and velocity perturbations as

$$\left.\begin{aligned}T'(x,z,t) &= \theta(z)\exp(ikx + \sigma t),\\ \mathbf{u}'(x,z,t) &= [U(z), 0, W(z)]\exp(ikx + \sigma t),\end{aligned}\right\} \tag{42}$$

where $\theta(z)$, $U(z)$, and $W(z)$ are complex vertical eigenfunctions of the temperature and velocity component perturbations, σ is a complex eigenvalue referred to as the growth rate and k is a real variable referred to as the wavenumber. Chandrasekhar (1961) proved that the imaginary part of σ is always zero for the Rayleigh–Bénard problem and hence that σ may be treated as a real variable. However this cannot be shown for more complicated problems such as internally heated or compressible liquids, and Skilbeck (1976) has found complex growth rates in internally heated liquids. Consequently we retain the complex form of σ in our calculations. If the dimensionless horizontal half-wavelength of the perturbation (the ratio of the width of the cell to the depth of the layer) is represented by λ', then the wavenumber is defined as $k = \pi/\lambda'$.

Considering liquids heated entirely from below ($\epsilon_0 = 0$), $d_z T_b$ may be written as $-\beta_0$, a constant, and $T_b = (1-z)\,\beta_0$ [see (38)]. Thus with $\boldsymbol{\omega}' = \nabla \times \mathbf{u}'$, substitution of (42) into (39)–(41) yields

$$\rho\sigma\theta = \rho W\beta_0 - \rho D[T_0 + (1-z)\,\beta_0]\,W + \kappa_0(d_z^2 - k^2)\,\theta, \tag{43}$$

$$(d_z^2 - k^2)\,(-ikW + d_z U) = \rho ik\theta - \frac{D}{\Gamma}\left[(d_z^2 - k^2)\,U + \frac{D}{3\Gamma}ikW\right], \tag{44}$$

$$ikU + d_z W = (D/\Gamma) W, \tag{45}$$

where d_z has been written in place of d/dz.

Equations (43)–(45) are solved numerically using the propagator matrix technique (Gilbert & Backus 1966). Details of the numerical procedure are described in appendix A. By incorporating a search scheme into the computer programs, the possible values of any one parameter can be determined as a function of the others. Of particular interest are neutral curves for marginal stability (the behaviour of β_0, and therefore of R_0, *versus* k when σ is equal to zero) and growth rate curves (the behaviour of σ *vs.* k).

3.2. *Results*

Neutral curves, R_0 *vs.* k, are shown in figure 1 for the limiting case of $D \to 0$ and for values of D equal to 0·117, 0·25, 0·50 and 1·00. Curves for the latter three values are labelled A, B and C respectively and have the same values of κ_0 as for the corresponding series of non-linear models (see table 8). For $D \to 0{\cdot}0$ and $D = 0{\cdot}117$, $\kappa_0 = 0{\cdot}00436$. Values of Γ and T_0 were 1·1 and 273 respectively for all cases.

The fundamental curves for $D \to 0{\cdot}0$ and $D = 0{\cdot}117$ are shown in order to emphasize the point that in the compressible formulation R_0 does not represent the classical Rayleigh number; since the adiabatic gradient is included in its definition, R_0 will be larger than the classical Rayleigh number even in 'incompressible' liquids. It is only in the limit of $D \to 0{\cdot}0$, when the compressible equations reduce to the Boussinesq equations, that R_0 has the same meaning as the Rayleigh number. (Nevertheless the minimum of R_0, for $D = 0{\cdot}117$, occurs at almost the same value of k as for $D \to 0{\cdot}0$.) When $D \to 0{\cdot}0$, R_0 has a minimum value of 385 at $k = 1{\cdot}76$ in agreement with previous calculations (e.g., McKenzie *et al.* 1974; Skilbeck 1976).

Curves for the three most unstable modes are shown in figure 1 for the remaining values of D. The number of internal nodes, n, in the vertical velocity eigenfunction is indicated at points on the curves. At low values of D, the fundamental (i.e. most unstable) mode has no internal nodes and each successive higher mode has one additional node. At larger values of D, however, zero-node disturbances are inhibited; at $D = 0{\cdot}50$, $n = 1$ for the fundamental mode (in the range of wavenumbers $\pi \leqslant k \leqslant 3\pi$) and at $D = 1{\cdot}00$, $n = 2$ or 3.

This may be understood by considering figure 2 which shows examples of temperature and entropy profiles, and vertical-velocity eigenfunction structures, at values of $D = 0{\cdot}25$, 0·50 and 1·00. The unstable upper regions are shown as zones of superadiabatic temperature gradient or negative entropy gradient. The stabilizing effect of the adiabatic gradient increasing in magnitude with depth, and with D, is clearly seen in the velocity perturbation eigenfunction structure. The zone of large amplitudes is concentrated upwards as D increases and small countercells occur, at large D, in the gravitationally stable lower zone. The uppermost cells are driven by thermal instability while the lower cells are driven by viscous coupling to the upper cells. The uppermost cells extend well into the stable zone; in the finite-amplitude solutions discussed in § 4, the gravitationally unstable zone itself extends to the bottom of the layer at large values of R_0. We will define these two effects as 'overshooting' and 'penetration' respectively. It is noteworthy that the upper cells in figure 2 never overshoot beyond the point of zero entropy change. (If S_d is the value of S at the

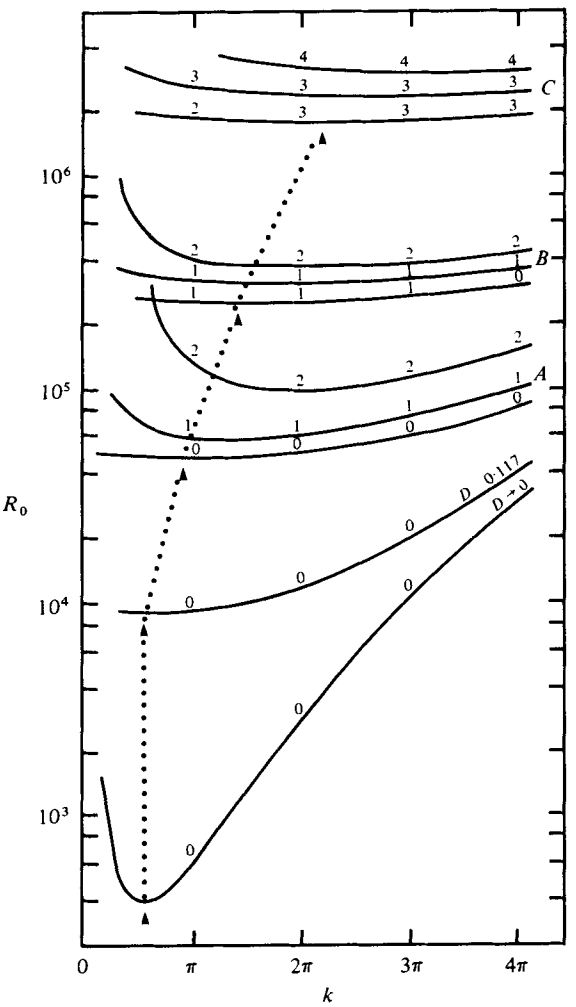

FIGURE 1. Neutral curves (loci of zero growth rate) for various values of D. Curves for the fundamental mode only are shown for $D \to 0{\cdot}0$ and $D = 0{\cdot}117$. Curves for the three most unstable modes are shown for $D = 0{\cdot}25$ (curves A), $D = 0{\cdot}50$ (curves B) and $D = 1{\cdot}00$ (curves C). Numbers on the curves indicate the number of internal nodes in the vertical velocity eigenfunction. Arrowheads indicate the critical value of R_0 at each value of D.

deepest point of overshooting and $S_{\max}$ the maximum value of S, then for $D = 0{\cdot}50$ and $D = 1{\cdot}00$ we have $S_d/S_{\max} = 0{\cdot}30$ and $0{\cdot}25$ respectively.)

The lowest value of R_0 on the fundamental neutral curve, for each value of D, is referred to as the critical value and is written here as $R_c^0(D)$; the corresponding critical wavenumber is written $k_c(D)$. The critical points $[R_c^0(D), k_c(D)]$ are indicated on figure 1 with small arrows, and tabulated in table 2; the dotted line joining these points on figure 1 illustrates a general trend of increasing critical wavenumber with increasing D. This effect is presumably due to the shallower depths of the unstable regions at large values of D, the horizontal wavelength being reduced in a shallower layer.

In a layer of unrestricted horizontal dimension, the onset of convection should occur

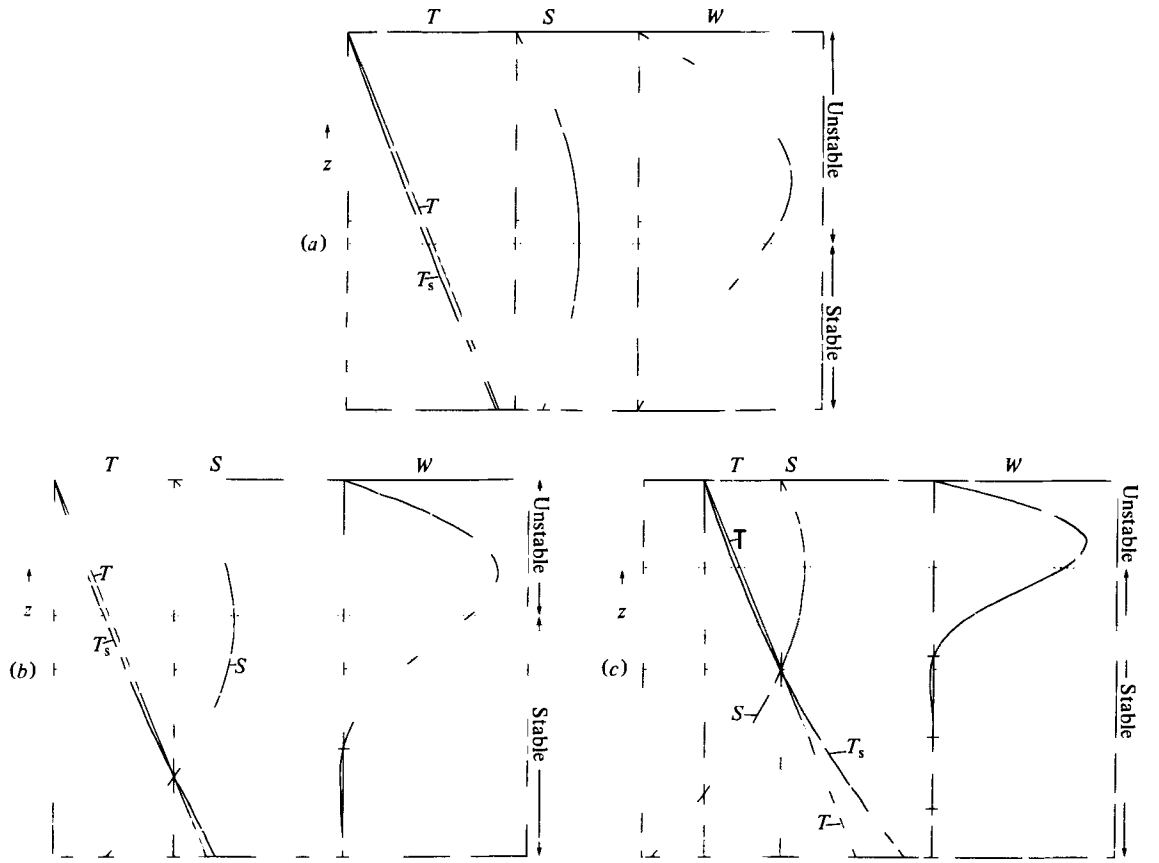

FIGURE 2. Vertical profiles of temperature T, adiabatic temperature T_s, entropy S, and vertical velocity eigenfunction W, at points on fundamental neutral curves: (*a*) $D = 0{\cdot}25$, $k = \pi$, $R_0 = 4{\cdot}87 \times 10^4$; (*b*) $D = 0{\cdot}50$, $k = 2\pi$, $R_0 = 2{\cdot}62 \times 10^5$; (*c*) $D = 1{\cdot}00$, $k = 2\pi$, $R_0 = 1{\cdot}84 \times 10^6$. The temperature difference across the layer, β_0, varies from one case to the next and T scales have been adjusted accordingly. Entropy is measured relative to the surface value. W is plotted with arbitrary amplitude. Bars on the z axes of the W profiles indicate the location of internal nodes. The horizontal line divides gravitationally stable and unstable regions.

D	R_c^0	k_c	Δz^{-1}
0·00	384·70	1·76	25
0·117	9109·2	1·79	25
0·25	48751	2·90	25
0·50	260116	4·46	100
1·00	1897970	6·92	200

TABLE 2. Critical values of R_0, k and the spatial increment of the numerical solution Δz

at the critical points indicated on figure 1. However, in the nonlinear numerical solutions discussed in the following sections, all streamlines are confined to a horizontal extent equal to the depth of the layer and, consequently, an integral number of rolls must fit within this region. Possible values of λ' are therefore restricted to

	$k = \pi$		$k = 2\pi$		$k = 3\pi$		$k = 4\pi$		
D	R_0	n	R_0	n	R_0	n	R_0	n	Δz^{-1}
0·00	586·8	0	2846	0	10597	0	29632	0	25
0·117	9310	0	11690	0	19915	0	40124	0	25
0·25	48697	0	51133	0	60212	0	82199	0	25
0·50	261487	1	262230	1	275994	1	307377	0	100
1·00	1897320	2	1842120	3	1856880	3	1920230	3	200

TABLE 3. Discrete values of R_0 at $k = m\pi$ for $m = 1, 2, 3$ and 4, corresponding number of internal nodes (n) in $W(z)$, and the spatial increment of the numerical solution, Δz

$1, \frac{1}{2}, \frac{1}{3}, \ldots$ and hence possible values of k are π, 2π, $3\pi \ldots$. Accordingly, it is the lowest value of R_0 at these discrete values of k which is of interest for comparison with the nonlinear results. Table 3 summarizes the values of R_0 and n occurring at $k = \pi$, 2π, 3π and 4π on the most unstable of each set of curves. At $D = 0{\cdot}0$, $0{\cdot}117$ and $0{\cdot}25$, $k_c = \pi$ and $n = 0$; that is, one roll occupying the whole box is the most unstable mode. At $D = 0{\cdot}50$, $k_c = \pi$ and $n = 1$; two cells, one above the other, fill the box. However the minimum of R_0 occurs almost midway between $k = \pi$ and $k = 2\pi$, which results in R_0 differing by less than $0{\cdot}3\,\%$ at these two points. As seen below (§ 4.2.2) a two-roll wide *marginal* flow persists in the nonlinear model $B1$ (presumably due to the restrictive influence of the side walls). In this case the nonlinear solution must be compared to the linear predictions at $k = 2\pi$. At $D = 1{\cdot}0$, $k_c = 2\pi$ with $n = 3$; the pattern is two rolls wide and four rolls deep. (The flat appearance of the upper curves in figure 1 is exaggerated by the use of a logarithmic scale for R_0; table 3 gives a clearer indication.)

Growth rate curves, σ *vs.* k, are useful in establishing the correct sequence of the various modes. For a given value of R_0, the numerical scheme searches (in the neighbourhood of initial estimates) for possible values of σ at specified values of k. To ensure that no modes are missed, initial values of σ are supplied at $k = 0$, at which point all possible values can be determined independently.

In the limit of $k = 0$, (43)–(45) combine to give

$$(\kappa_0 d_z^2 - \rho\sigma)\{\rho^{-1}[d_z^4 - (D/\Gamma)^2 d_z^2]\}\, W = 0, \tag{46}$$

or, defining

$$Q(z) = \rho^{-1}[d_z^4 - (D/\Gamma)^2 d_z^2]\, W, \tag{47}$$

(46) can be written as

$$(d_z^2 - \rho\sigma')\, Q(z) = 0, \tag{48}$$

where we have written σ' for σ/κ_0. $Q(z)$ is a horizontally uniform temperature perturbation. From the equation of motion (44) and the boundary conditions on θ, we have $d_z Q = 0$ at $z = z_0$, and $Q = 0$ at $z = z_1$, as boundary conditions on Q. Solving the relatively simple eigenvalue problem posed in (48) yields the possible values of σ' at $k = 0$. In the limit of $D \to 0$, $\rho = 1{\cdot}0$ and $Q(z)$ has a solution of the form

$$Q = A \cos(-\sigma)^{\frac{1}{2}} z, \tag{49}$$

with $\sigma' = -(n - \frac{1}{2})^2 \pi^2$ for $n = 1, 2, 3, \ldots$. For finite D, however, $\rho = \exp[(1-z)D/\Gamma]$ and no such simple expression exists. Qualitatively, since $\rho(z)$ is greater than or equal to one for all z, we can expect the magnitude of the eigenvalues σ' to decrease

i	$D \to 0{\cdot}00$	$D = 0{\cdot}25$	$D = 0{\cdot}50$	$D = 1{\cdot}00$
1	$-2{\cdot}47$	$-2{\cdot}1$	$-1{\cdot}8$	$-1{\cdot}3$
2	$-22{\cdot}2$	$-19{\cdot}7$	$-17{\cdot}4$	$-13{\cdot}6$
3	$-61{\cdot}6$	$-54{\cdot}8$	$-48{\cdot}7$	$-38{\cdot}1$
4	$-120{\cdot}4$	$-107{\cdot}3$	$-95{\cdot}4$	$-74{\cdot}9$

TABLE 4. Values of σ_i' at $k = 0$, for $i = 1, 2, 3$ and 4

with increasing D. The first four values of σ' computed from (48) at each value of D are listed in table 4. These are used as estimates at low values of k (e.g. $k = 0{\cdot}01$) and the search program follows the $\sigma'(k)$ curves out in small steps dk.

Figure 3 shows examples of growth rate curves for the first four modes. It is clear from figure 3(a) that the points ($R_0 = 1{\cdot}86 \times 10^6$, $k = 4{\cdot}5$) and ($R_0 = 1{\cdot}86 \times 10^6$, $k = 9{\cdot}8$) lie on the neutral curve of the most unstable mode at $D = 1{\cdot}00$. We have plotted only the real part of σ', denoted Re (σ'), on this diagram. Inspection of (43)–(45) shows however that, for every eigenvalue σ, its complex conjugate σ^* is also an eigenvalue with corresponding eigenfunctions U^*, W^* and θ^*, the complex conjugates of U, W and θ. Thus when σ is complex two *distinct* modes may have equal real parts and their growth rate curves will appear to merge on diagrams such as those shown in figure 3. Complex values of σ were a common feature in this study; an example is shown in figure 3(b) wherein the upper two curves merge for $0{\cdot}25 \leqslant k \leqslant 0{\cdot}55$. No complex growth rates were encountered when Re $[\sigma(k, R_0)]$ first became positive and therefore no overstable marginal solutions were found; the principle of exchange of stabilities is obeyed. However there is nothing inherent in the mathematics to guarantee that σ will be real whenever Re $(\sigma) > 0$.

Table 3 presents the principal results of this section. To compare these data with the nonlinear solutions, refer to figures 11 (a), 12 (a) and 13 (a) which show low Rayleigh number solutions for the three series of nonlinear models. The number of internal nodes, n, in the vertical velocity/streamfunction and the wavenumber, k, are tabulated for each of these solutions in table 5. Comparison of tables 3 and 5 shows agreement on the structure of marginal convection (i.e. the same value of n for equal values of k). The critical values of R_0 at wavenumbers corresponding to those in table 5 have been converted into critical values of heat flux and plotted as large solid circles on the 'conduction' line in figure 16. The close agreement of these points with extrapolations of the three curves labelled A, B and C is a measure of the consistency between the linear and the nonlinear solutions.

3.3. *Accuracy of the numerical results*

The values of $\sigma'(k = 0)$, listed in table 4, are indicated as solid circles on the $k = 0$ axis in figures 3(a) and 3(b). These agree closely with the values determined by the search program at low k. Having established the eigenvalues at $k = 0$ it is straightforward to integrate (46) numerically to compute the shape of the eigenfunction $W(z)$. This has been done and compared with $W(z)$ as computed from the propagator matrix [equation (70)] at $k = 0{\cdot}01$, for the first four modes at each value of D. Corresponding eigenfunctions agree in every case with a maximum discrepancy at any point of 3% and a mean of less than 1%.

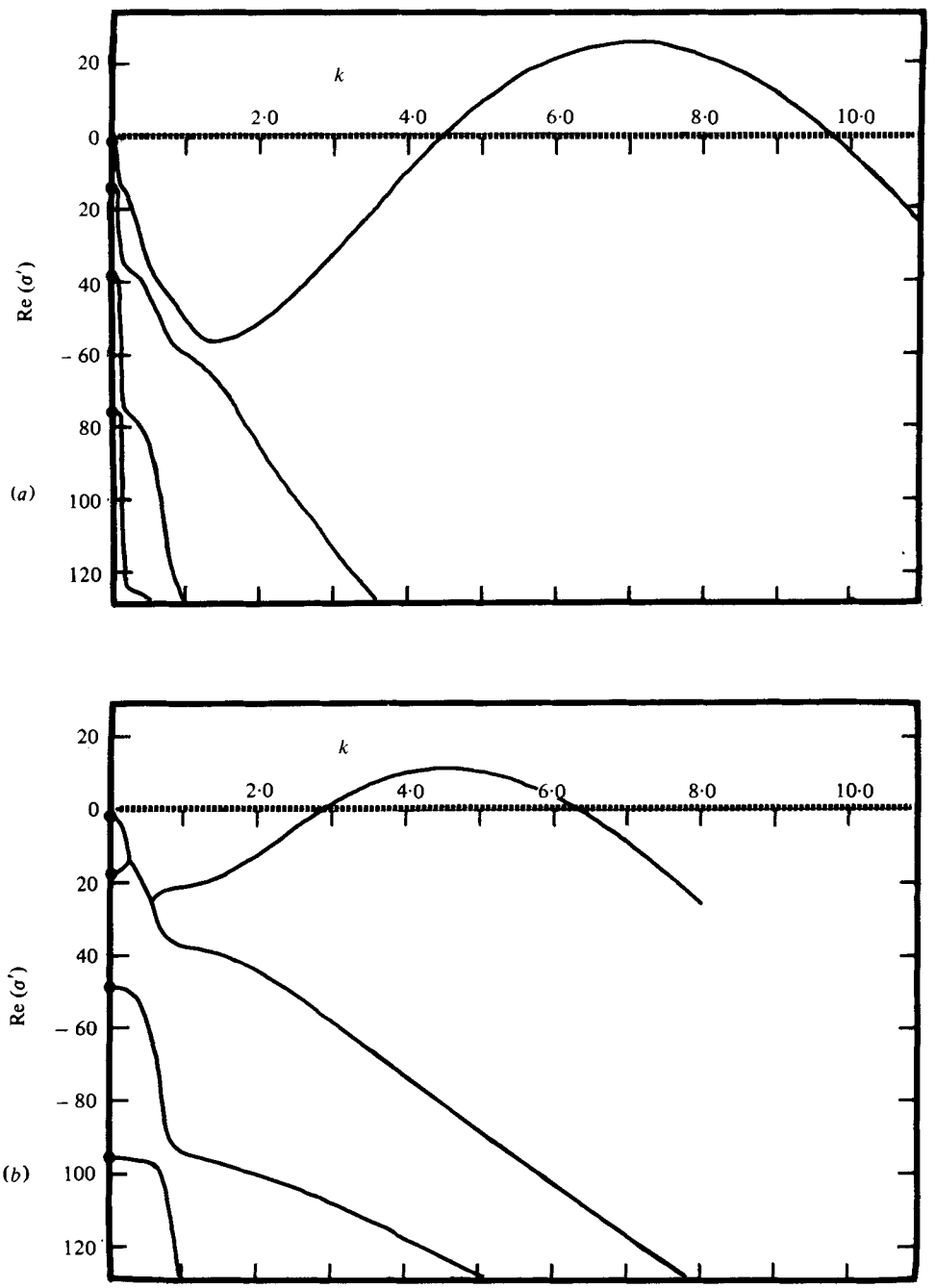

FIGURE 3. (*a*) Growth rate curves for $R_0 = 1{\cdot}86 \times 10^6$, $D = 1{\cdot}00$. Curves for the first four modes are shown. Large solid circles on the Re (σ') axis are the values of $\sigma'(k = 0)$ predicted by solving (59) and tabulated in table 3. (*b*) Growth rate curves for $R_0 = 2{\cdot}62 \times 10^5$, $D = 0{\cdot}50$. The first and second modes have complex values of σ' for $0{\cdot}25 \leqslant k \leqslant 0{\cdot}55$. The most unstable mode has Re (σ') > 0 and Im (σ') $= 0$ for $2{\cdot}90 \leqslant k \leqslant 6{\cdot}28$.

Series	D	n	k
A	0·25	0	π
B	0·50	1	2π
C	1·00	3	2π

TABLE 5. Cell structure of nonlinear marginal convection solutions

A similar linear stability analysis was performed by Peltier (1972) who included the non-Boussinesq feature of adiabatic temperature gradients proportional to temperature. His results are in qualitative agreement with those presented above. However a direct comparison is not possible since Peltier used rigid boundaries with fixed temperatures, and ignored compressibility and non-hydrostatic pressures. Furthermore T_0 was taken to be 0 °K in Peltier's analysis so that the stabilizing influence of the adiabatic gradients was minimized; with this surface temperature no internal nodes in the vertical velocity are found until $D > 2{\cdot}25$.

As a final check of our numerical results, we have run four cases using the same boundary conditions as Peltier and suppressing the density variation and non-hydrostatic pressure fluctuations. Resultant values of R_c^0, k_c and n (the number of internal nodes in the vertical velocity eigenfunction) for values of D covering the range studied by Peltier are listed in column 2 of table 6. These may be compared with Peltier's figures listed in column 1 of table 6. At the largest value of D, the two values of R_c^0 differ by approximately 5%, values of k_c by 1·5% and the eigenfunction structure is the same. At $D = 1{\cdot}0$, the upper limit in our study, the two numerical schemes agree to within 0·2%. The divergence of the two numerical schemes at larger D is presumably due to differences in the numerical integration procedures employed. These checks give us confidence in the accuracy of the numerical scheme.

3.4. *Influence of density variations and non-hydrostatic pressure*

The separate effects of variable density and non-hydrostatic pressure gradients are also shown in table 6 (columns 4 and 5 respectively). The stabilizing effect of variable density (compare columns 3 and 4) remains relatively small for $D \leqslant 1{\cdot}0$ ($\leqslant 12\%$) but becomes a major effect at $D = 3{\cdot}0$, increasing the critical value of R_0 tenfold. Inclusion of non-hydrostatic pressure gradients is also seen to increase stability (compare columns 3 and 5). This effect however remains relatively small even for D as large as 3·0 ($\leqslant 11\%$).

As emphasized by Peltier (1972), the effect of a non-zero surface temperature T_0 is to increase stability since the magnitude of the (stabilizing) adiabatic temperature gradient is proportional to the absolute temperature. At $D = 1{\cdot}0$, values of R_c^0 shown in table 3 (computed with $T_0 = 273$ °K) are two orders of magnitude larger than those in table 6. This marked difference cannot be due to the weakly stabilizing effects of density stratification and non-hydrostatic pressure, and thus demonstrates an extreme sensitivity of the calculations to the value of T_0. Non-zero surface temperatures also appear to minimize the significance of the non-hydrostatic pressure since, as discussed in § 4 below, when horizontal pressure gradients are suppressed, the values listed in table 3 are altered by less than 0·03% (in contrast to the 3% difference indicated in table 6).

	Peltier (1972) ($\rho = 1, T_0 = 0, P_1 = 0$)			Present study ($\rho = 1, T_0 = 0, P_1 = 0$)			($\rho = \rho(z), T_0 = 0, P_1 = 0$)			($\rho = 1, T_0 = 0, P_1 \neq 0$)			
D	R_c	k_c	n	R_c^0	k_c	n	R_c^0	k_c	n	R_c^0	k_c	n	Δz^{-1}
0·0	1707·6	3·12	0	1707·7	3·12	0	1708	3·12	0	1708	3·12	0	25
0·5	2275·3	3·13	0	2275·4	3·12	0	2321	3·12	0	2289	3·12	0	50
1·0	3390·3	3·13	0	3384·3	3·13	0	3795	3·13	0	3473	3·13	0	50
3·0	95625	6·05	1	91422	5·97	1	956260	6·16	3	101530	6·13	1	200

TABLE 6. Comparison of numerical schemes and effect of variable density and non-hydrostatic pressures.
(Δz is the spatial increment of the numerical solution.)

Before returning to the nonlinear problem we note that R_0 may also be written in terms of the thermometric heat flux across the layer, $f_0 = -\kappa_0 dT/dz = \kappa_0 \beta_0$. Thus

$$R_0 = \frac{g\alpha d^4}{\kappa_0^2 \nu_0} \left(\frac{\bar{\rho}}{\rho_0}\right)^2 f_0. \tag{50}$$

This definition is useful for the finite-amplitude convection models since f_0 is specified as a boundary condition at the lower boundary, whereas temperature gradients vary across the convecting layer. In the conductive limit (50) and (36) are identical. In the remainder of this paper, we will refer to R_0 as defined in (50) as the Rayleigh number.

4. Nonlinear model solutions

Given an initial temperature field the anelastic–liquid equations $(A1)$–$(A4)$, listed in table 1 above, can be solved cyclically to generate the temporal development of T, ω, ψ and $\mathbf{u}$. The finite-difference method used to solve these equations is described in appendix B. Equation $(A1)$ shows that vorticity is generated by horizontal gradients of temperature and pressure, the importance of the pressure gradient increasing with d/H_T. However, as discussed in appendix B, we find that the solution of a truncated version of $(A1)$,

$$\nabla^2 \omega = \rho_r \partial T/\partial x, \tag{51}$$

provides a close approximation to ω. Thus, as in Boussinesq fluids, vorticity is generated primarily by horizontal temperature gradients.

4.1. *In the Boussinesq limit*

As a preliminary study, a comparison is made between the incompressible model of McKenzie *et al.* (1974) and the present anelastic model in the Boussinesq range of $d/H_T \ll 1$. Two examples (figures 4, 5) are considered with $d/H_T = 0{\cdot}117$. The two Boussinesq models have $R_0 = 2{\cdot}4 \times 10^5$ and $R_0 = 1{\cdot}4 \times 10^6$, with no internal heating ($\epsilon_0 = 0$). The corresponding anelastic models with the same thermodynamic parameters have $R_0 = 2{\cdot}7 \times 10^5$ and $1{\cdot}6 \times 10^6$ respectively (the differences in R_0 between the Boussinesq and anelastic cases being due to the density variation in the anelastic models). The solutions are similar but, as expected, the isothermal core of the Boussinesq temperature solution is replaced by an adiabatic core in the anelastic case. To facilitate comparison of the temperature solutions, an (horizontally uniform) adiabatic temperature field was subtracted from the anelastic model temperatures. Contours of the resulting temperature fields (figures 4*c*, 5*c*) are very similar to those of the Boussinesq model. These results demonstrate that the incompressible-liquid solutions are accurate representations of compressible flow for the case $d/H_T = 0{\cdot}117$.

The mean temperature of the convection rolls is higher in the compressible solutions. This is due to the (slightly) reduced vigour of convection resulting from non-zero adiabatic temperature gradients. The importance of this effect diminishes as the heat flux, $F = -K\partial T/\partial z$, at the bottom boundary is increased. With the constant flux bottom boundary condition, a higher mean temperature corresponds to a lower convected heat transport and hence a smaller Nusselt number [see equation (34)]. In the anelastic cases shown in figures 4 and 5, the respective computed Nusselt numbers were 30 % and 14 % lower than in the corresponding Boussinesq solutions.

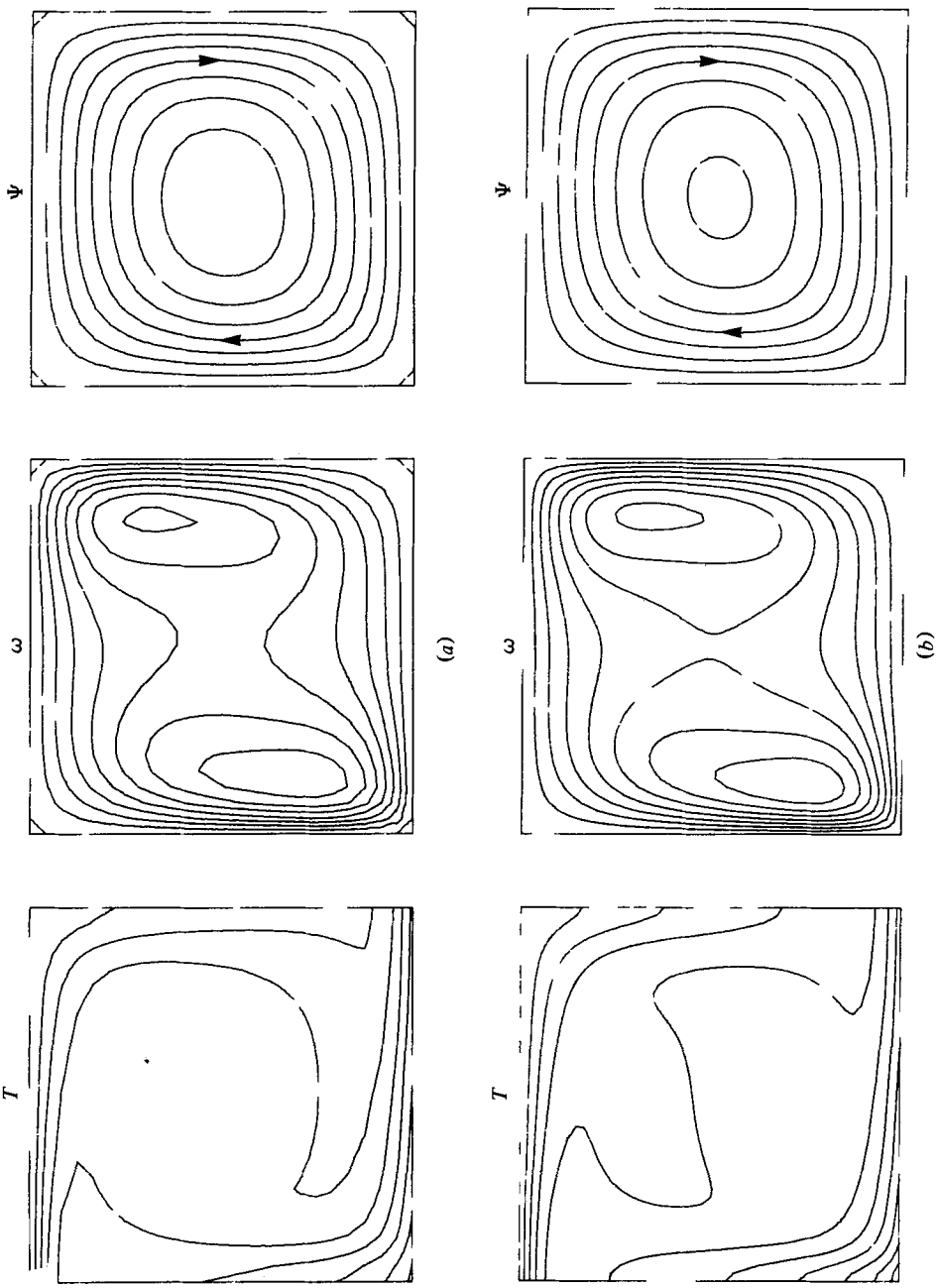

For legend see facing page.

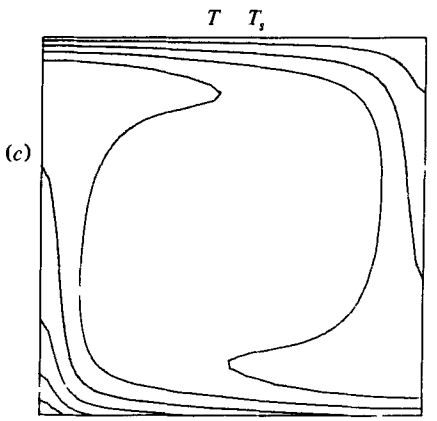

FIGURE 4. Comparison of Boussinesq and anelastic numerical solutions of dimensionless temperature, vorticity and stream function, for $d/H_T = 0{\cdot}117$. (*a*) Boussinesq solution from McKenzie *et al.* (1974); $R_0 = 2{\cdot}4 \times 10^5$. (*b*) Anelastic solution *Bous*1; $R_0 = 2{\cdot}7 \times 10^5$. The difference in values of R_0 in (*a*) and (*b*) is due to the density increase with depth in the anelastic case. All other parameters are the same for (*a*) and (*b*). (*c*) Temperatures resulting from the anelastic solution after subtracting an horizontally uniform reference adiabatic temperature field. The anelastic solution was computed on a 48×48 finite-difference grid. Contour levels: T, 0 (21·8) 218; ω, 0 (0·43) 3·01; ψ, 0 (0·021) 0·147. Values in parentheses indicate contour intervals. Contours of $T - T_s$ are plotted with the same interval as T.

Values of the ratio Φ/F were also computed from the two anelastic solutions. These were 0·107 and 0·113, in reasonable agreement with (2). The value of 0·107, for the lower Rayleigh number model, is lower than that predicted from (2) because not all of the heat is being carried by convection. In the higher Rayleigh number case, convection is more vigorous and agreement is better.

A point of great concern in all numerical modelling studies is the accuracy and internal consistency of the numerical solutions obtained. Outside the Boussinesq limit, solutions independent of those presented here are not available for comparison. The model must, therefore, rely upon internal checks. One such check requires that in a steady state the vertical energy flux F', defined as

$$F' = \langle \rho C_p T w \rangle + \langle -K\, \partial T/\partial z \rangle + \langle -\tau_{3j} u_j \rangle, \tag{52}$$

where $\langle\ \rangle$ denotes the horizontal average, be constant. The first two terms on the right-hand side of this equation represent the convected and conducted vertical heat transport respectively. The third term represents the vertical transport of energy by viscous forces and is $O(d/H_T)$. The maximum deviation of F' from the bottom value, F, is reported as a percentage of F for each model (typically 1–5 %) and denoted dF. For the anelastic models in figures 4 and 5, the respective values of dF are 1·04 % and 1·89 %.

A second internal check is provided by integrating the thermal energy equation in steady state over the volume V of the convecting region. This yields the relation

$$\int_V \tau_{ij}(\partial u_i/\partial x_j)\, dV = -\int_V \alpha T \mathbf{u}.\nabla P\, dV. \tag{53}$$

The left-hand integral in (53) represents the global rate of dissipative heating, while

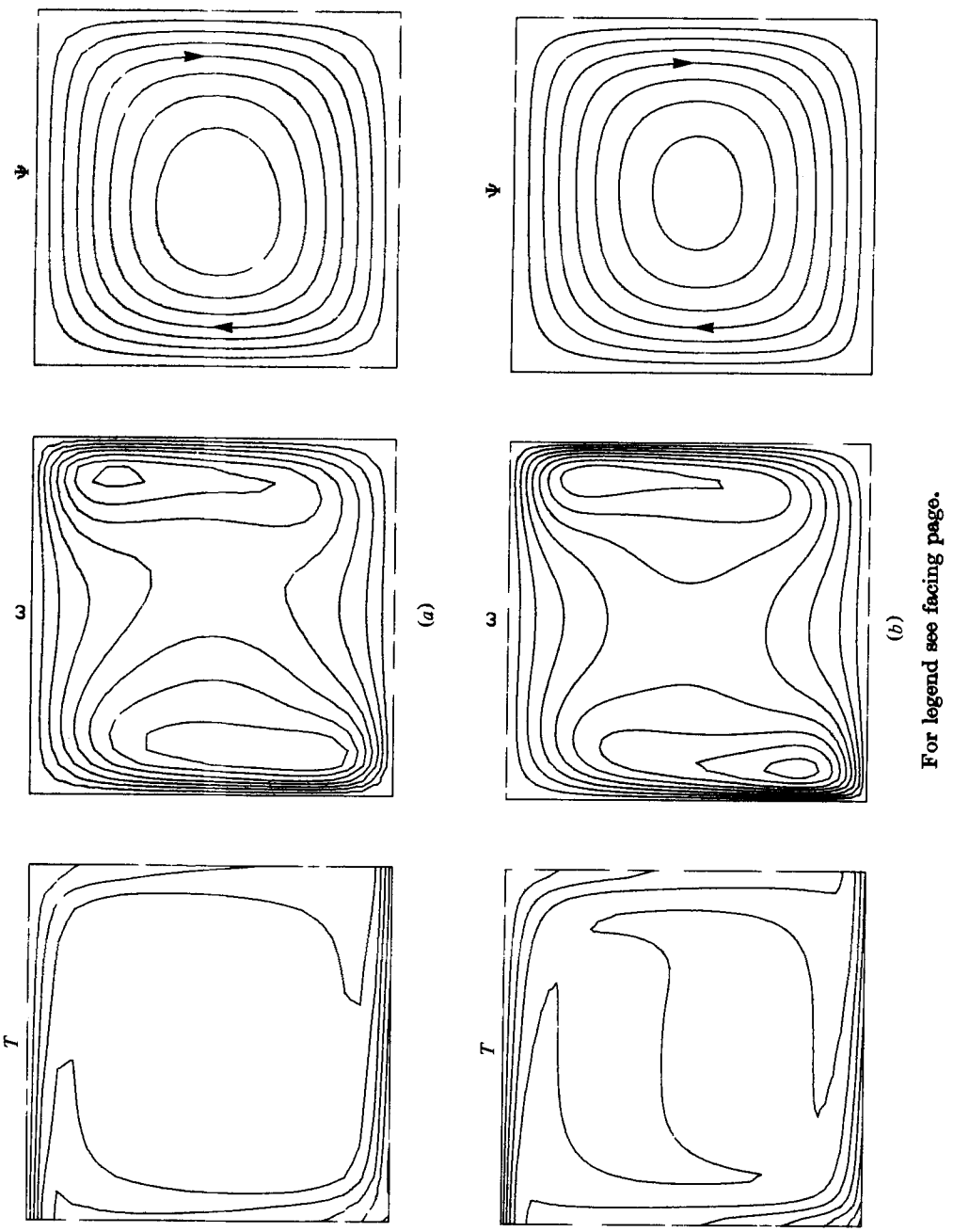

For legend see facing page.

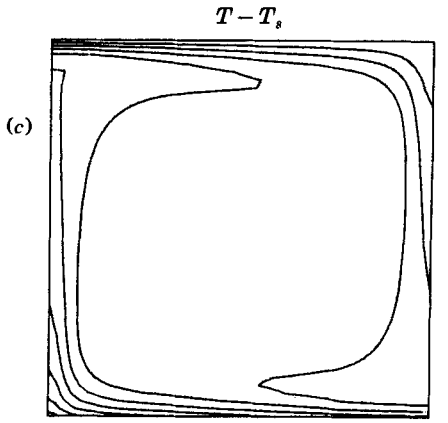

FIGURE 5. Comparison of Boussinesq and anelastic numerical solutions of dimensionless emperature, vorticity and stream function, for $d/H_T = 0{\cdot}117$. (*a*) Boussinesq solution from McKenzie *et al.* (1974); $R_0 = 1{\cdot}4 \times 10^6$. (*b*) Anelastic solution *Bous2*; $R_0 = 1{\cdot}6 \times 10^6$. (*c*) Superadiabatic temperature field computed from anelastic solution as in figure 4. Anelastic solution computed on a 48×48 finite-difference grid. Contour levels: T, 0 (75·0) 750; ω, 0 (1·063) 8·504; ψ, 0 (0·047) 0·329. Contours of $T - T_s$ are plotted with the same interval as T.

the right-hand integral represents the global rate at which work is done by the fluid in adiabatic volume changes. Thus in steady state, internal energy is provided by frictional heating at the same rate as it is absorbed by the compression work cycle.

In the hydrostatic approximation $\nabla P \approx \nabla P_H = -\rho_r g \hat{\mathbf{e}}_z$, where $\hat{\mathbf{e}}_z$ is a unit vector in the positive z direction, so that (53) becomes

$$\int_V \tau_{ij}(\partial u_i/\partial x_j)\,dV = \frac{A}{H_T}\int_z \langle \rho_r C_p T w\rangle\,dz, \tag{54}$$

where A is the area of the layer, and the integrand on the right-hand side is the horizontally averaged convected heat flux at height z. The left- and right-hand integrals of (54) were evaluated numerically from the solutions of all models. Since the viscous heating is a strongly localized function of space, while the work done in adiabatic volume changes is relatively uniform (figure 6), numerical integration of the right-hand side of (54) can be expected to be the more accurate. Consequently the deviation dV between the two volume integrals is reported as a percentage of the right-hand integral. For the models of figures 4 and 5 the respective values of dV are 0·23 % and 0·29 %. The accuracy and internal consistency of the model is thus considered to be satisfactory for small values of d/H_T.

Before leaving the Boussinesq limit, a fundamental difference between the anelastic and Boussinesq formulations should be remarked. This is the dependence of the anelastic solution on the temperature T_0 of the upper surface. T_0 appears in (*A* 3) because the adiabatic gradient is proportional to the absolute temperature, not the temperature relative to the upper boundary. The comparison of Boussinesq and anelastic solutions presented above justifies McKenzie *et al.*'s (1974) use of the Boussinesq equations to study convection in the upper mantle. The anelastic solutions were computed with $T_0 = 273$ °K. However since upper mantle convection occurs beneath rigid plates with basal temperatures of at least 900 °C (McKenzie & Weiss

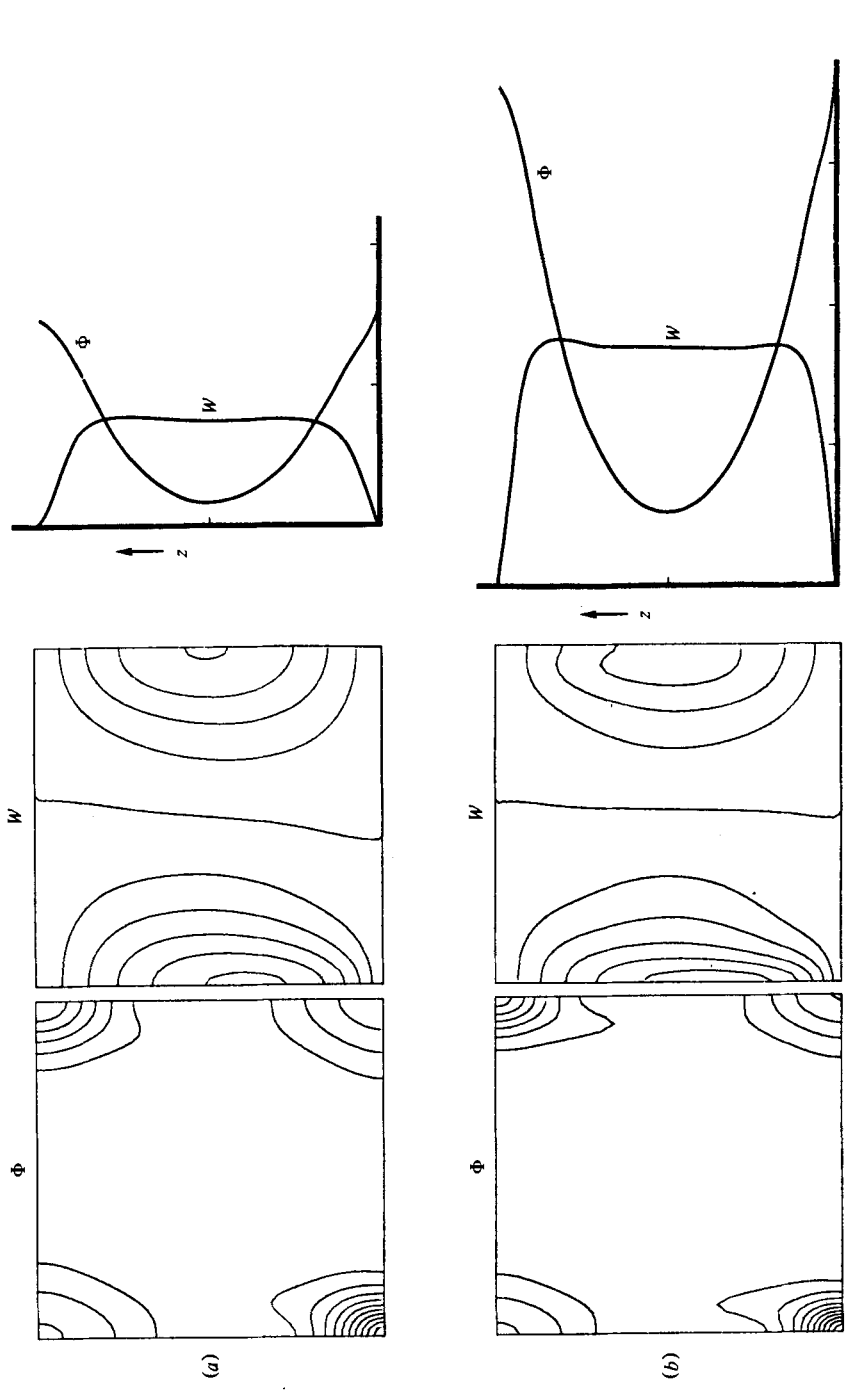

FIGURE 6. Spatial distribution of Φ, the rate of dissipative heating, and W, the vertically convected heat flux. W is proportional to the rate of working in adiabatic volume changes. (*a*) Contours and mean horizontal values of Φ and W for anelastic model *Bous*1 of figure 4(*b*). Contours: Φ, 0 (4·82) 48·2; W, −193 (51·0) 266. (*b*) Contours and mean horizontal values of Φ and W for anelastic model *Bous*2 of figure 5(*b*). Contours: Φ, 0 (37·5) 375; W, −675 (208) 1195. Φ and W are both in dimensionless units.

1975) a more reasonable value for T_0 is 1173 °K. This would give a near surface adiabatic gradient which is larger than those used in the previous cases by a factor of 4·3. To evaluate the importance of this effect, the model shown in figure 4 was re-run with $T_0 = 1173$ (figure 7). The close resemblance between the superadiabatic temperatures in figures 4 and 7 indicates that the validity of the Boussinesq approximation is not jeopardized by steep adiabatic gradients when $d/H_T \ll 1$.

4.2. *Non-Boussinesq results:* $0{\cdot}25 \leqslant d/H_T \leqslant 1{\cdot}50$

Three series of models were run over the range $6{\cdot}5 \times 10^4 \leqq R_0 \leqq 8{\cdot}8 \times 10^7$, one for each of the values of d/H_T equal to 0·25 (series A), 0·50 (series B) and 1·00 (series C). In addition one model was run with $d/H_T = 1{\cdot}50$. For each series d/H_T was held constant and R_0 was varied from model to model by increasing the heat flux F across the bottom boundary. The rate of internal heating ϵ_0 was set equal to zero and the upper surface temperature T_0 was 273 °K for all models. Most of the models were started by imposing a 1 °K horizontal temperature perturbation to a super-adiabatic temperature field such that a single convection roll resulted. Models at the high R_0 end of each series were initialized with the final solutions of lower R_0 models.

Model results. Parameter values for each of the models studied are listed in tables 7 and 8. Each model was run until the time-averaged temperature and kinetic energy became approximately constant.

Figure 8 illustrates the temporal development of three typical models. The kinetic energy E_k, mean temperature $\overline{T}$, efficiency E ($= \Phi/F$), and the ratio V_R and mean magnitude V_M of the left- and right-hand sides of (54) are plotted against time (in dimensionless units). In figure 8 (a), model $A3$ evolves to a steady state. The convective motions become steady after five or six overturns, while the mean temperature adjusts on a longer time scale which is controlled by *conductive* heat transfer out of the central core. The efficiency E settles to a constant value of 0·223, about 10% lower than predicted by (2). For this model, the ratio of the volume integrals of (54) has a constant value of 1·010 indicating a numerical discrepancy of 1·0%. Model $B7$ (figure 8b) is an example of an oscillatory time-dependent solution (see also figure 12(c) below). The mean temperature fluctuations are superimposed on a slow thermal adjustment as the time-averaged mean temperature approaches a constant equilibrium value. The efficiency E also oscillates in response to the changing velocities, but has a constant time-averaged value of 0·434. Similarly, the value of V_M varies, typically from 4·5 to 5·8 units. Values of V_R, although oscillating, never exceed 1·008 and have a mean of 1·005. Thus the balance indicated by (54) is maintained to within 0·8% for this oscillating solution even though the derivation of (54) is valid only for steady-state flows. Model $C10$ (figure 8c) is an example of a strongly time-dependent solution which has reached a time-averaged steady state. The time dependence is caused by cold parcels of fluid breaking away from the upper boundary layer. The efficiency E has a time-averaged value of 0·823, with instantaneous values ranging between 0·5 and 2·6. Though V_M shows considerable variations, fluctuations in V_R are limited to the range 0·98 to 1·07 with an approximate mean value of 1·005. The nature of the time dependence is discussed in § 4.2.2 below.

4.2.1. *Temperature and Entropy Profiles.* Horizontally averaged temperature profiles (figure 9) show that the approximately isothermal central regions of incompressible

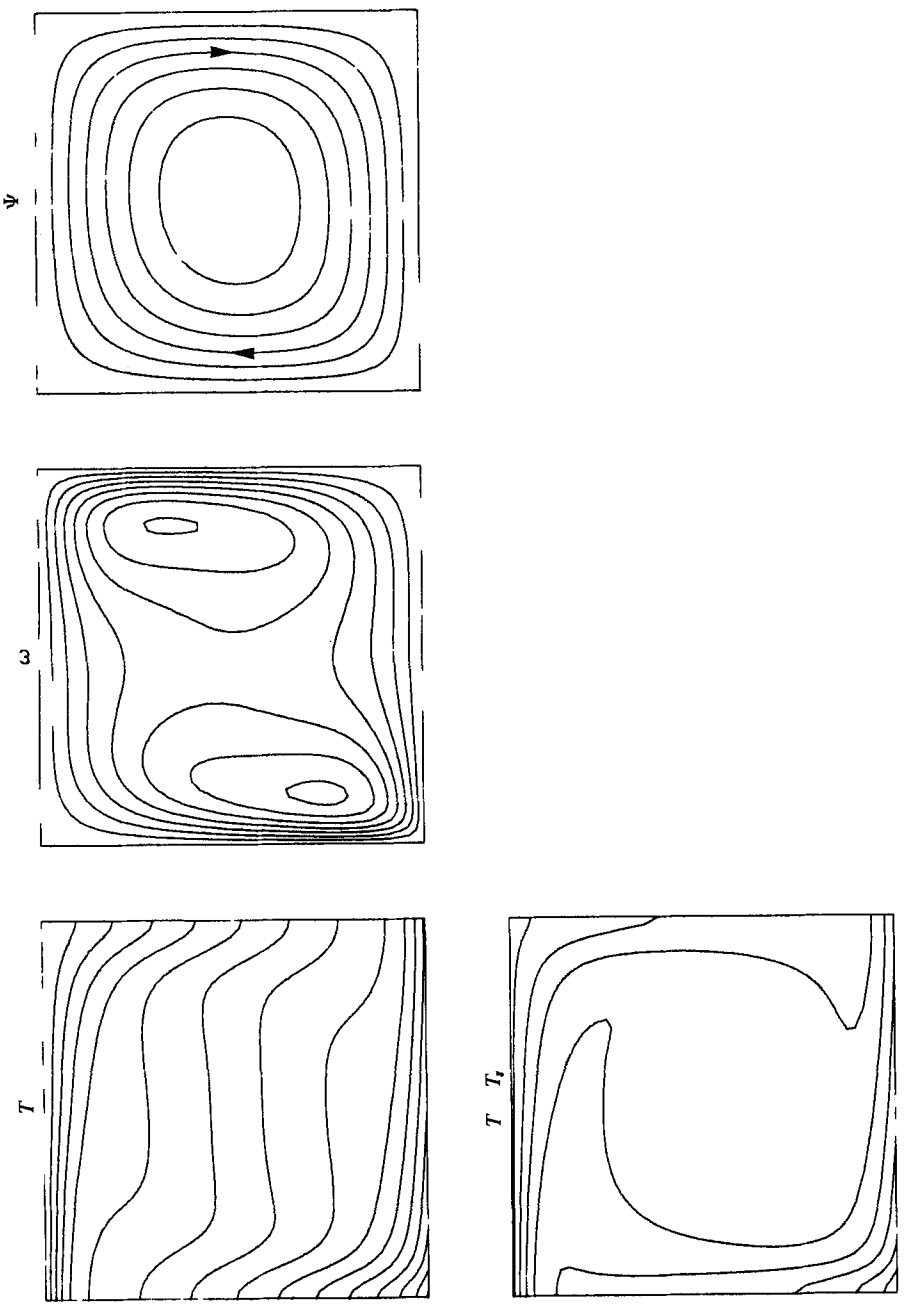

FIGURE 7. Anelastic model *Bous3*: $R_0 = 2{\cdot}7 \times 10^5$, $d/H_T = 0{\cdot}117$. Same as *Bous1* except for surface temperature $T_0 = 1173$ °K. Solution obtained on a 48×48 finite-difference grid. Contour levels as in figure 4.

Model	R_0	R_0/R_c^0	N	dF (%)	dV (%)	$F(=\Phi/F_u)$
*A*1	$6{\cdot}483\times10^4$	1·331	1·23	0·74	0·94	0·049
*A*2	$3{\cdot}242\times10^5$	6·657	3·60	1·85	0·98	0·202
*A*3	$6{\cdot}483\times10^5$	13·32	5·14	2·28	1·05	0·226
*A*4	$1{\cdot}297\times10^6$	26·63	6·87	2·20	1·07	0·240
*A*5	$2{\cdot}593\times10^6$	53·26	9·14	2·02	0·51	0·242
*A*6	$5{\cdot}187\times10^6$	106·5	11·05	2·56	0·52	0·244
*A*7	$7{\cdot}780\times10^6$	159·8	12·21	—	0·45	0·247
*B*1	$2{\cdot}802\times10^5$	1·070	1·03	0·29	1·89	0·011
*B*2	$4{\cdot}121\times10^5$	1·574	1·35	1·22	0·33	0·128
*B*3	$4{\cdot}945\times10^5$	1·889	1·54	0·93	0·85	0·185
*B*4	$6{\cdot}593\times10^5$	2·519	1·91	1·50	1·01	0·263
*B*5	$9{\cdot}889\times10^5$	3·778	2·55	2·68	0·86	0·330
*B*6	$1{\cdot}648\times10^6$	6·297	3·53	—	0·95	0·382
*B*7	$3{\cdot}296\times10^6$	12·59	5·06	—	0·65	0·431
*B*8	$6{\cdot}593\times10^6$	25·19	7·13	—	0·57	0·441
*B*9	$9{\cdot}889\times10^6$	37·78	8·36	—	0·66	0·461
*B*10	$1{\cdot}648\times10^7$	62·97	9·82	—	0·45	0·473
*B*11	$2{\cdot}637\times10^7$	100·8	11·34	—	0·07	0·483
*C*1	$1{\cdot}971\times10^6$	1·072	1·01	2·30	2·36	0·02
*C*2	$2{\cdot}190\times10^6$	1·189	1·03	6·27	1·96	0·05
*C*3	$2{\cdot}737\times10^6$	1·486	1·17	—	1·57	0·15
*C*4	$3{\cdot}285\times10^6$	1·784	1·31	—	1·59	0·17
*C*5	$3{\cdot}832\times10^6$	2·081	1·45	—	1·37	0·27
*C*6	$5{\cdot}475\times10^6$	2·973	1·93	—	0·13	0·44
*C*7	$8{\cdot}212\times10^6$	4·459	2·50	—	0·80	0·56
*C*8	$1{\cdot}642\times10^7$	8·918	3·78	—	0·14	0·76
*C*9	$2{\cdot}190\times10^7$	11·89	4·55	—	0·91	0·80
*C*10	$2{\cdot}737\times10^7$	14·86	5·22	—	0·10	0·82
*C*11	$3{\cdot}832\times10^7$	20·81	6·28	—	1·74	0·87
*C*12	$5{\cdot}475\times10^7$	29·73	7·30	—	2·49	0·89
*C*13	$8{\cdot}759\times10^7$	47·57	8·25	—	0·18	0·90
*Bous*1	$2{\cdot}683\times10^5$	27·9	5·15	1·04	0·23	0·107
*Bous*2	$1{\cdot}570\times10^6$	163·3	10·28	1·89	0·29	0·113
*Bous*3	$2{\cdot}683\times10^5$	—	3·77	4·44	0·23	0·094
*D*1	$2{\cdot}185\times10^8$	37·38	7·37	—	1·81	1·30

TABLE 7. Model characteristics. d/H_T is 0·25, 0·50, 1·00, 1·50 and 0·117 for series *A*, *B*, *C* and *D* and the anelastic *Bous* models respectively

models are replaced by approximately adiabatic central cores in the compressible models. The thin conductive thermal boundary layers at the upper surface vary little, while those at the bottom become less pronounced as d/H_T increases. This behaviour occurs because more heat is conducted down the steeper adiabatic gradient near the bottom where convection is (accordingly) less vigorous, an effect which becomes more important as d/H_T increases. Indeed if d/H_T is increased sufficiently, for a fixed bottom flux F, first the lower regions and then the entire layer are stabilized as the amount of heat which is capable of being conducted down the adiabatic gradient exceeds the actual heat flux F. For example, penetrative convection occurs for $d/H_T = 1{\cdot}00$ and R_0 between $2{\cdot}0\times10^6$ and $4{\cdot}5\times10^6$, that is, between curves *C*1 and *C*6 on figure 9(*d*).

If a parcel of descending (ascending) fluid is heated (cooled) adiabatically, its entropy

Model	F'	T_0'	Δz^{-1}
*A*1	105·11	273	24
*A*2	525·53	273	24
*A*3	1051·05	273	24
*A*4	2102·10	273	24
*A*5	4204·20	273	48
*A*6	8408·40	273	48
*A*7	12612·60	273	48
*B*1	178·68	273	24
*B*2	262·76	273	24
*B*3	315·32	273	24
*B*4	420·42	273	24
*B*5	630·63	273	48
*B*6	1051·05	273	48
*B*7	2102·10	273	48
*B*8	4204·20	273	48
*B*9	6306·30	273	48
*B*10	10510·51	273	48
*B*11	16816·81	273	48
*C*1	378·38	273	48
*C*2	420·42	273	48
*C*3	525·53	273	48
*C*4	630·63	273	48
*C*5	735·74	273	48
*C*6	1051·05	273	48
*C*7	1576·58	273	48
*C*8	3153·15	273	48
*C*9	4204·20	273	48
*C*10	5255·25	273	48
*C*11	7357·35	273	48
*C*12	10510·51	273	48
*C*13	16816·81	273	48
*Bous*1	1051·05	273	48
*Bous*2	6148·65	273	48
*Bous*3	1051·05	1173	48
*D*1	21021·02	273	96

TABLE 8. Values of dimensionless parameters. $\Gamma = 1{\cdot}10$ for all models. Values of $(d/H_{T,K_1}')$ are: (*a*) series *A*, (0·25, 0·00204); (*b*) series *B*, (0·50, 0·00102); (*c*) series *C*, (1·00, 0·00051); (*d*) model *D*1, (1·50, 0·00034); (*e*) anelastic *Bous* models, (0·117, 0·00436)

remains constant. Thus calculation of the horizontally averaged value of entropy as a function of depth can be used to determine the degree to which the central zone approximates a region of adiabatic heating and to better distinguish the gravitationally unstable boundary layers, notably the lower one.

Considering the temperature and pressure to be two parameters of state, the entropy S may be expressed as $S = S(T, P)$, whence

$$\frac{dS}{dz} = \left(\frac{\partial S}{\partial T}\right)_P \frac{dT}{dz} + \left(\frac{\partial S}{\partial P}\right)_T \frac{dP}{dz}. \tag{55}$$

Making use of the thermodynamic definitions of C_p and α, and Maxwell's relations, (55) may be written

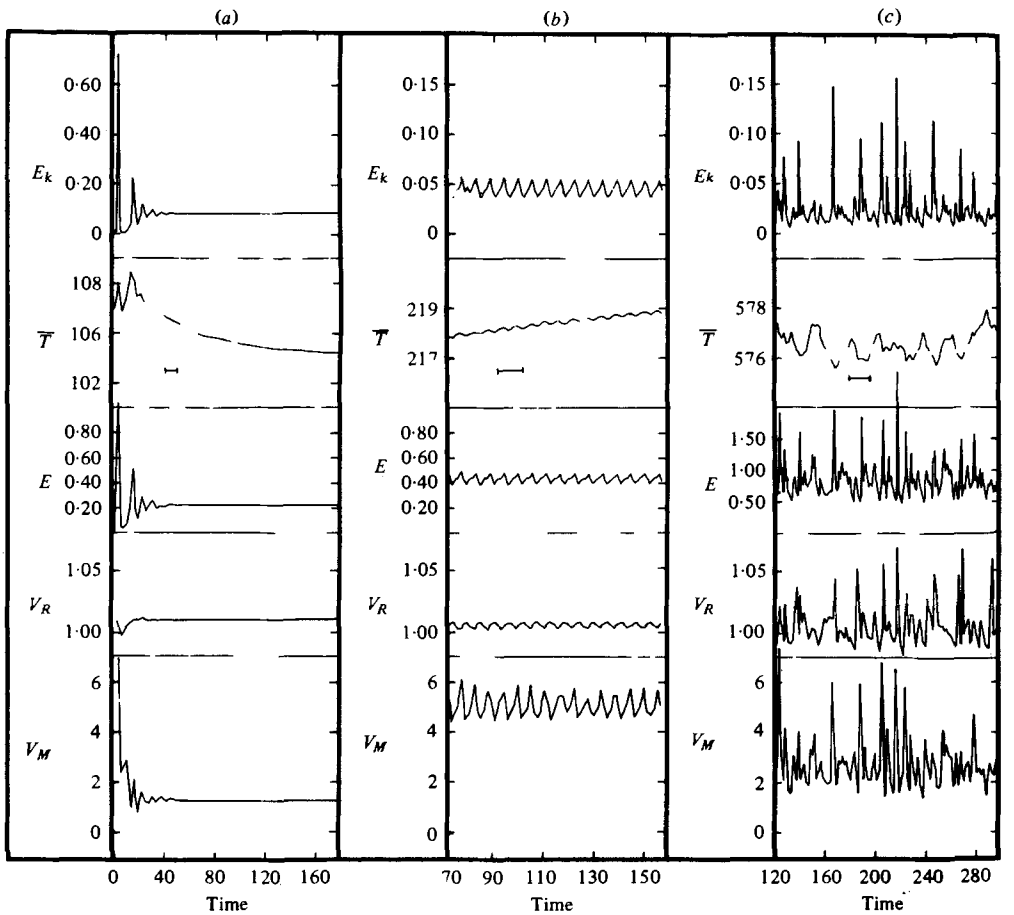

FIGURE 8. Temporal development of typical steady-state and time-dependent numerical solutions. Kinetic energy E_k, overall mean temperature $\bar{T}$, efficiency E ($= \Phi/F_u$), the ratio V_R of the two volume integrals in (54), and the mean magnitude of the same two volume integrals V_M are plotted against dimensionless time. E_k and $\bar{T}$ are in dimensionless units, E and V_R have no units and V_M is plotted with arbitrary units. The small horizontal bar on the temperature graphs indicates the approximate time for one overturn. $\bar{T}$, V_R and V_M were only evaluated every 50 time steps. This accounts for the clipped spikes in the plots of V_R and V_M. (*a*) Model *A*3 ($d/H_T = 0{\cdot}25$, $R_0/R_c^0 = 13{\cdot}3$): solution obtained on a 24×24 finite-difference grid; approximately 148 time steps per overturn. (*b*) Model *B*7 ($d/H_T = 0{\cdot}50$, $R_0/R_c^0 = 12{\cdot}6$): solution obtained on a 48×48 finite-difference grid; approximately 400 time steps per overturn. (*c*) Model *C*10 ($d/H_T = 1{\cdot}00$, $R_0/R_c^0 = 14{\cdot}9$): solution obtained on a 48×48 finite-difference grid; approximately 493 time steps per overturn.

$$\frac{dS}{dz} = \frac{C_p}{T}\frac{dT}{dz} - \frac{\alpha}{\rho}\frac{dP}{dz}. \tag{56}$$

With the assumption that $dP/dz = -\rho g$, integration of (56) from z to $z = d$ gives

$$S(d) - S(z) = C_p \ln(T_0/T) + \alpha g(d - z). \tag{57}$$

Equation (57) expresses, in dimensional form, the difference in entropy between the upper surface and any point (x, z). For an adiabatic temperature distribution, T

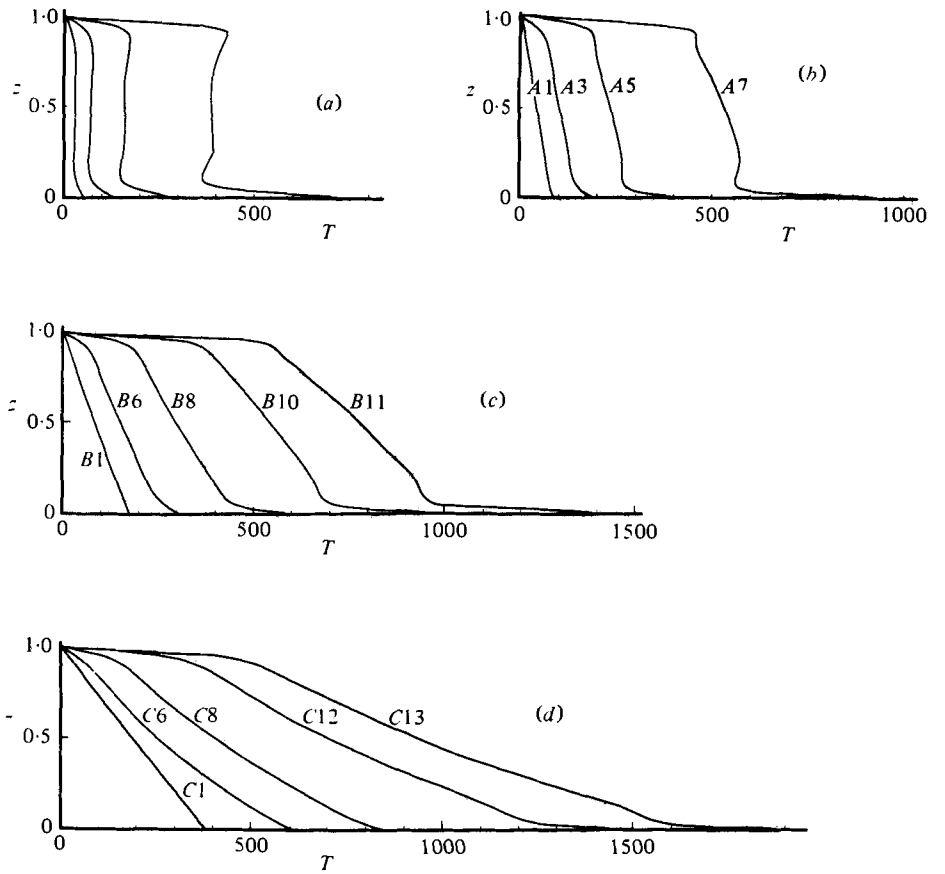

FIGURE 9. Vertical profiles of horizontally averaged temperature. (*a*) Boussinesq solutions from McKenzie *et al.* (1974). $d'H_T \ll 1$ (incompressible). (*b*) Anelastic solutions with $d/H_T = 0{\cdot}25$. (*c*) Anelastic solutions with $d/H_T = 0{\cdot}50$. (*d*) Anelastic solutions with $d/H_T = 1{\cdot}00$. Labels on the anelastic profiles indicate the specific models. Temperature and height are in dimensionless units.

would have the form $T = T_0 \exp[(d-z)\alpha g/C_p]$ and the right-hand side of (57) would vanish for all z. To express (57) in dimensionless form, a dimensionless entropy S' can be defined as $S' = S/C_p$ and, using the substitutions of § 2.1, we have (suppressing primes)

$$\Delta S = S(z) - S(1) = \ln[(T+T_0)/T_0] - (1-z)D, \tag{58}$$

where, as before, $D = d/H_T$ and T_0 is the temperature of the upper surface.

Vertical profiles of the horizontally averaged value of ΔS for several models of each series are displayed in figure 10. The similarity of these curves to temperature profiles of Boussinesq fluids (figure 9*a*) illustrates the parallel roles of entropy in compressible fluids and temperature in incompressible fluids. The central regions of the compressible models are isentropic, analogous to the isothermal region of Boussinesq fluids. This behaviour also occurs in compressible gases (Graham 1975). Interior zones of positive entropy gradient (corresponding to sub-adiabatic temperature gradients) analogous to the positive temperature gradients in Boussinesq fluids can also be seen on the

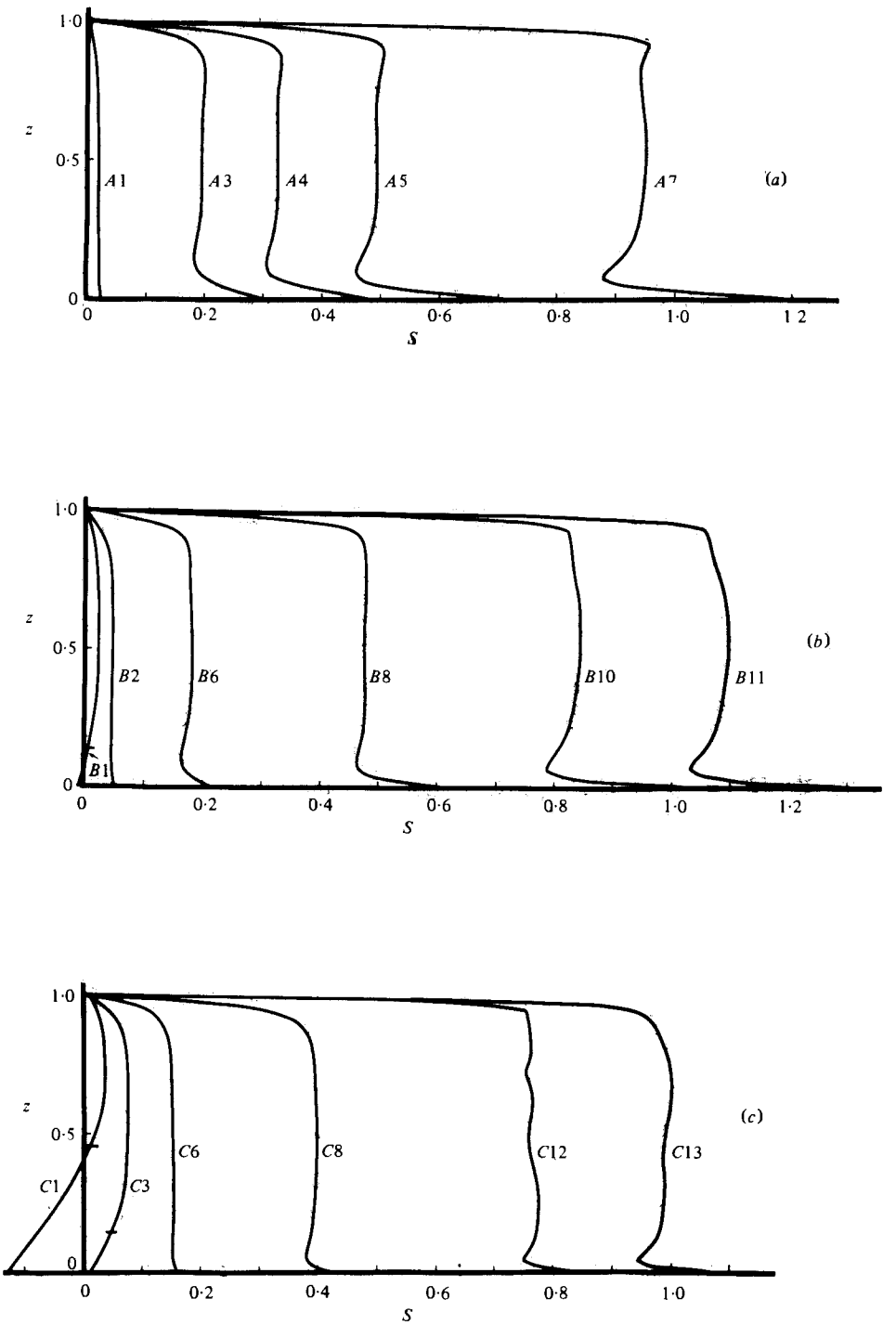

FIGURE 10. Vertical profiles of horizontally averaged entropy (measured relative to the value at the upper boundary). (*a*) Anelastic solutions with $d/H_T = 0{\cdot}25$. (*b*) Anelastic solutions with $d/H_T = 0{\cdot}50$. (*c*) Anelastic solutions with $d/H_T = 1{\cdot}00$. The Rayleigh number increases from left to right in each set of profiles. Labels on the curves indicate the specific models. Entropy and height are in dimensionless units. The horizontal bars on profiles *B*1, *C*2 and *C*3 indicate the depth of convective overshooting into the stable region.

profiles of figure 10. The gravitationally unstable boundary layers are also clearly demarcated on figure 10. In addition *stable* lower regions are evident in models $B1$, $C1$ and $C3$; these have no counterpart in the Boussinesq models.

4.2.2. *Two-dimensional fields.* Figures 11 to 13 show contours of temperature, vorticity, stream function, entropy, rate of viscous dissipation and rate of working in adiabatic volume changes [see equation (54)] for several of the models from each series.

(*a*) *Series A* ($d/H_T = 0{\cdot}25$). Figures 11(*a*) and 11(*b*) show the steady-state solutions of models $A1$ and $A3$. Figures 11(*c*, *d*) show two views of the time-dependent solution of model $A7$. For the range of Rayleigh numbers studied a single roll occupying the whole box persisted. However at the high Rayleigh number end of the series ($R_0 \gtrsim 5 \times 10^6$) the flow becomes time dependent. The time dependence takes the form of instabilities developing in the upper boundary layer and being swept into the downgoing plume. The resulting oscillations of mean kinetic energy and temperature are similar to those shown in figure 8(*b*).

Details of the flow solutions are best revealed in the vorticity field which varies most markedly through figures 11(*a*) to 11(*d*). The vorticity is generated primarily by horizontal temperature gradients (see equation (51)] and is thus dominated by the plume structure. In the classical Rayleigh–Bénard problem constant temperatures are applied across an incompressible fluid. The symmetry of the upper and lower boundary conditions results in a symmetric plume structure and, for large Rayleigh numbers, two local vorticity maxima of equal magnitude occur. If the constant-temperature bottom boundary condition is replaced by a constant-flux condition, the centre of the rising plume is hotter than in the Rayleigh–Bénard case and the vorticity has a maximum associated with the rising plume (figures 4, 5).

The models in this study were all heated entirely from below, with the constant-flux bottom boundary condition. However, the vorticity fields shown in figures 11(*a*) and 11(*b*) resemble those of incompressible liquids which are partially heated from within (McKenzie *et al.* 1974). The descending rather than ascending plumes dominate the flow and accordingly the vorticity is largest in the upper right. Since only the heat flux in excess of that which can be conducted down the adiabatic gradient is available to drive the convective motions, convection is least vigorous at the bottom. Moving upwards, the magnitude of the adiabatic gradient decreases and the energy driving the motion increases. Consequently the upper thermal boundary layers are more pronounced and produce the dominant plumes. This effect is most clearly seen in model $A1$ (see figures 9, 10, 11) for which the Rayleigh number R_0 is only greater than the critical value for the onset of convection, R_c^0, by a factor of 1·3.

As the Rayleigh number is increased through models $A3$ and $A7$, the bottom boundary layer develops and the rising plume becomes stronger. In model $A7$ the Rayleigh number is sufficiently large for the effect of the adiabatic gradients on the vorticity to be overcome by the rate of bottom heating. However the vertical extent of the zone of large vorticity next to the rising plume is considerably less than that of the corresponding zone next to the descending plume. A qualitatively similar feature was found in the partially internally heated Boussinesq models studied by McKenzie *et al.* (1974), arising from the geometry of the heat source disribution. In the present study, however, this feature is a direct consequence of the compressibility of the liquid. This may be seen by considering a cold parcel of compressible fluid, of

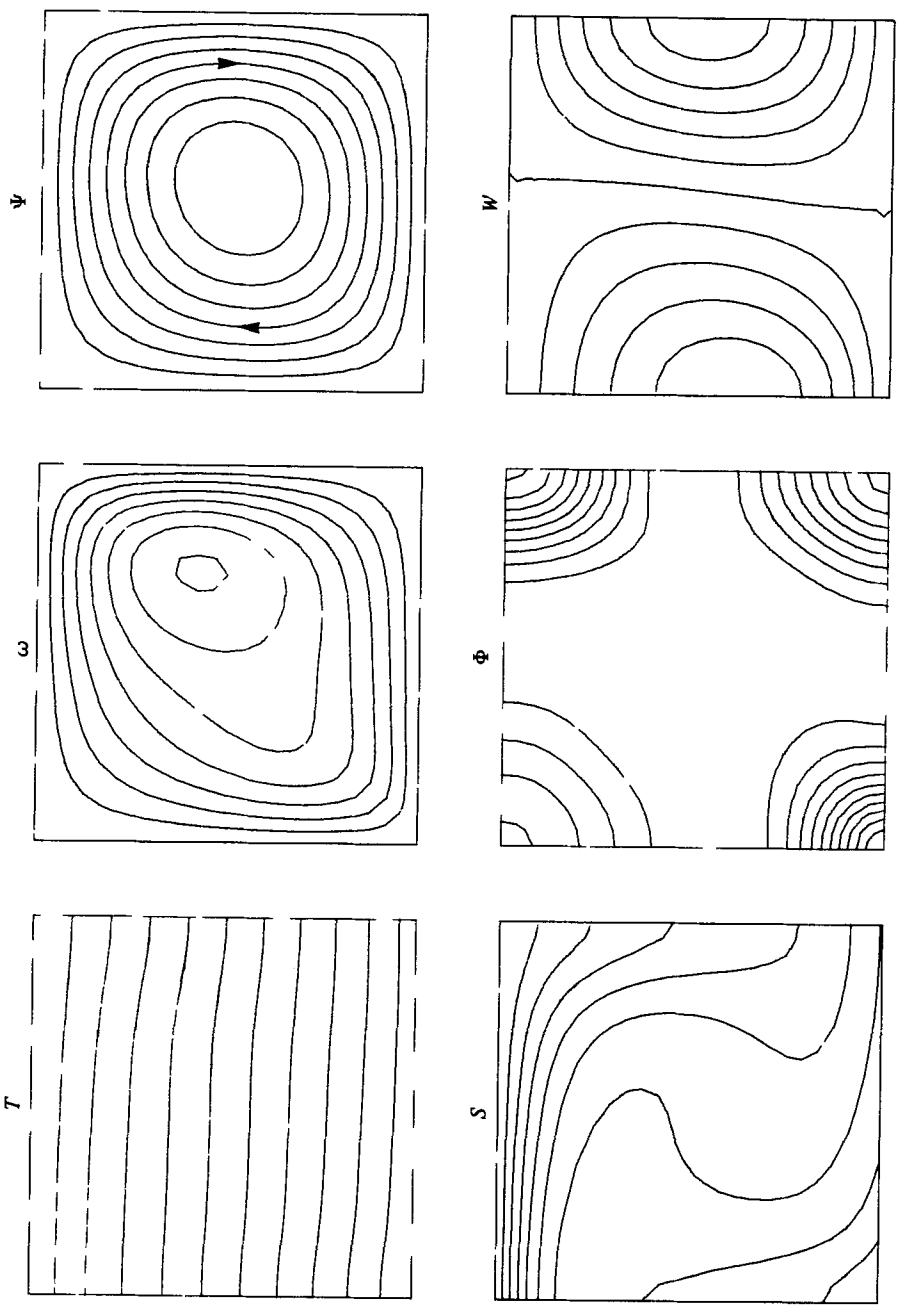

(*a*)

For legend see p. 550.

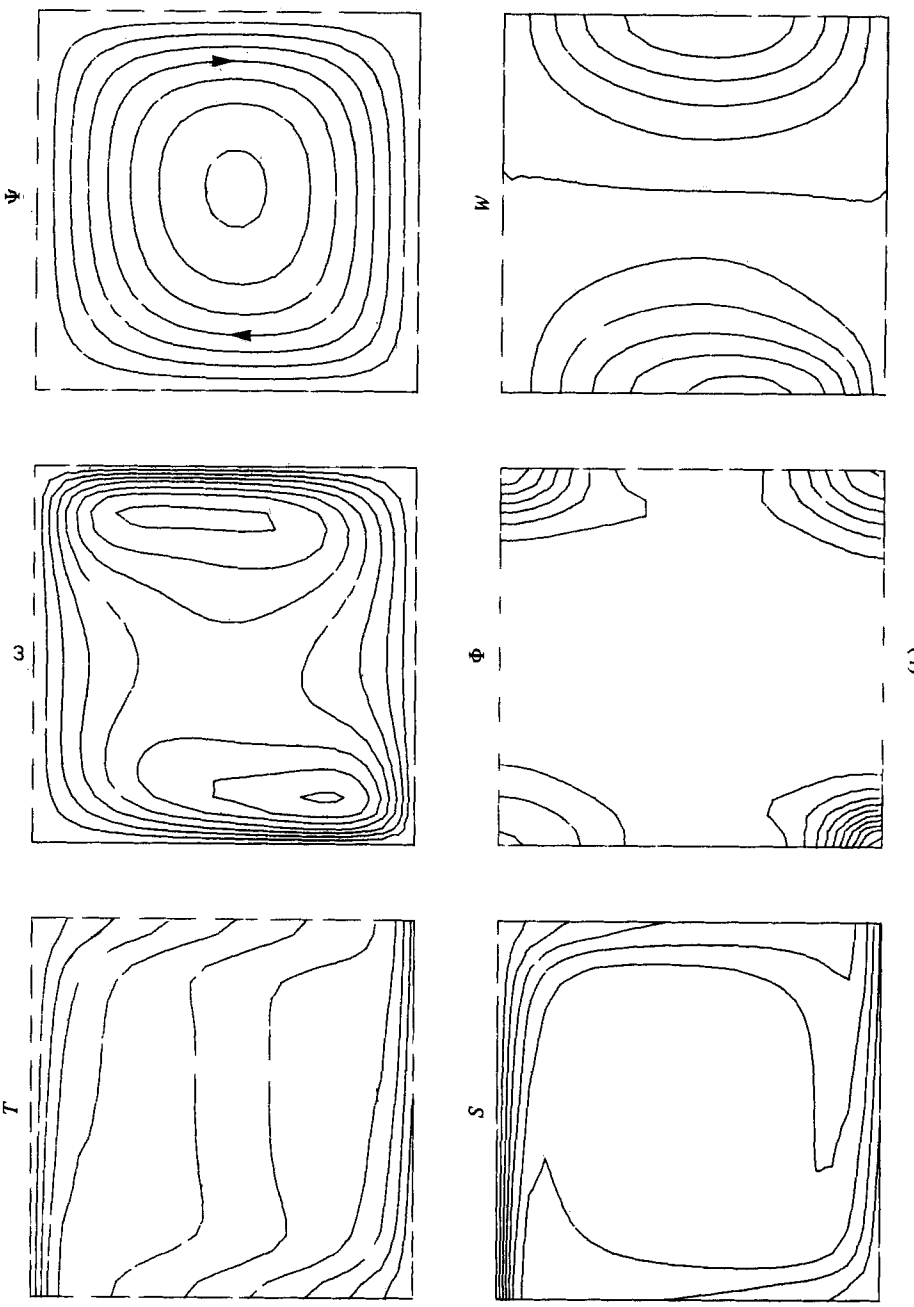

(b)

For legend see p. 550.

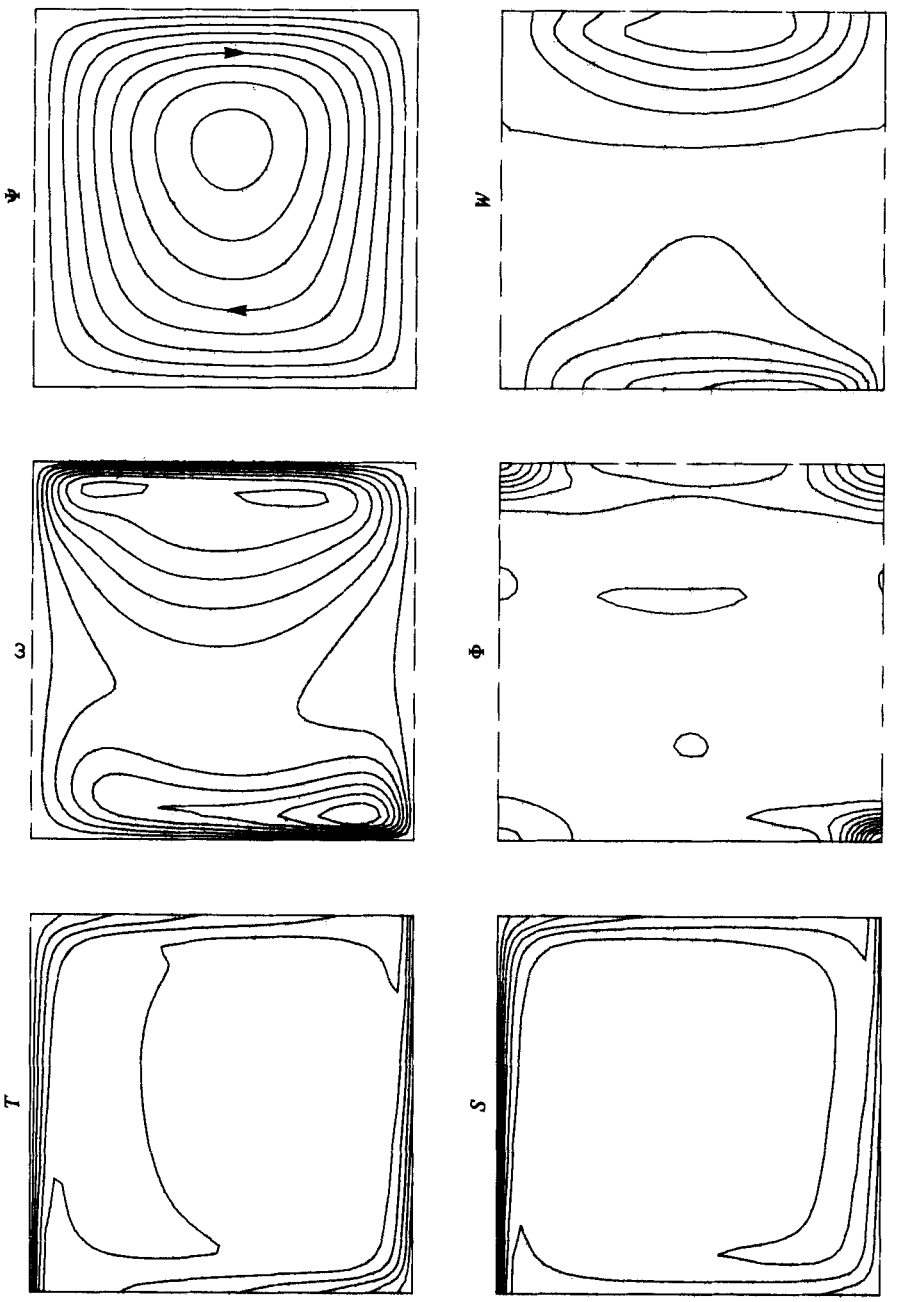

(*c*)

For legend see p. 550.

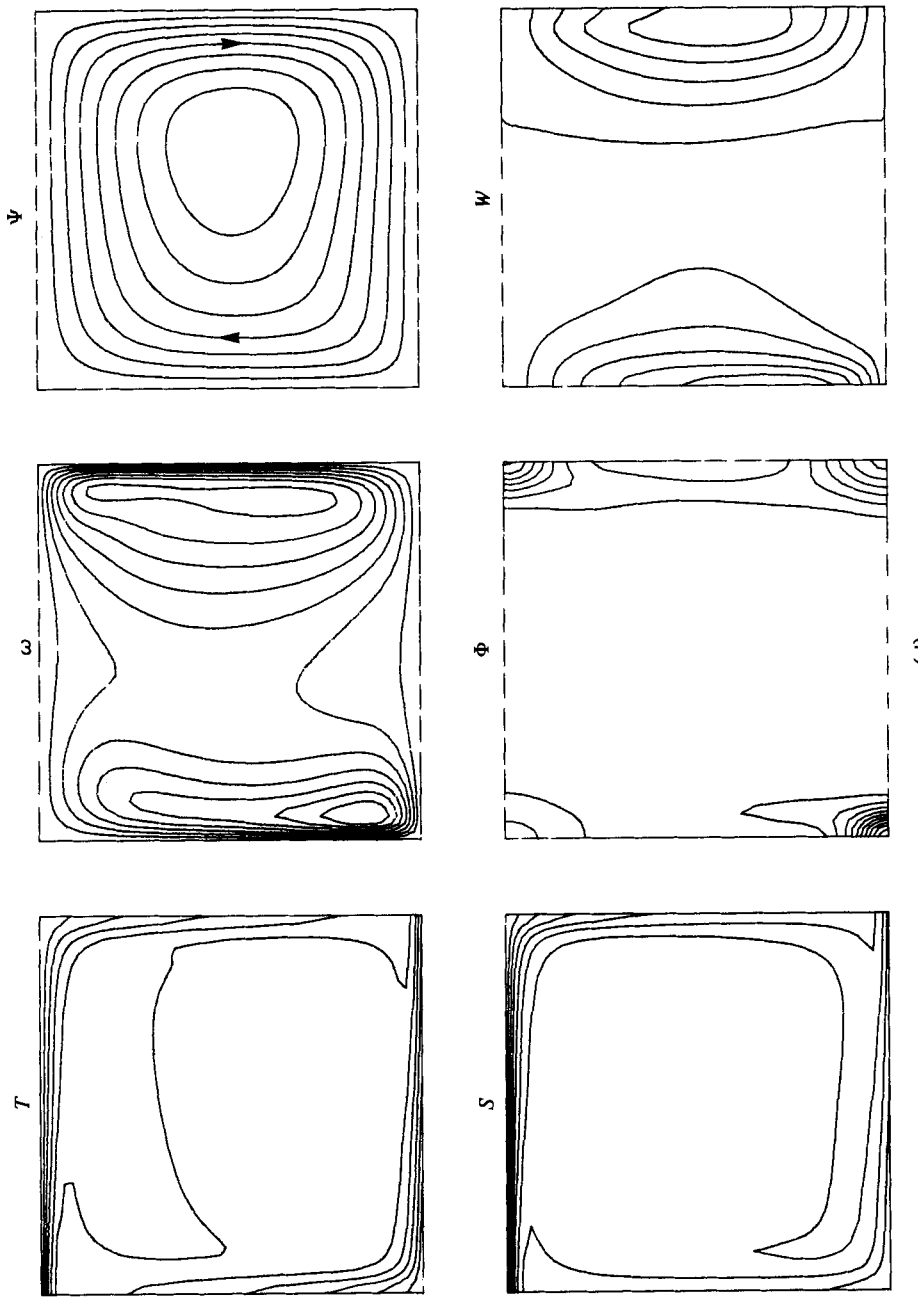

FIGURE 11. Numerical solution of anelastic models with $d/H_T = 0{\cdot}25$ (series A). Contours plot dimensionless temperature T, vorticity ω, stream function ψ, entropy S, rate of viscous dissipation Φ and vertically convected heat flux W. (*a*) Model *A*1: $R_0/R_c^0 = 1{\cdot}33$. Steady-state solution obtained on a 24×24 finite-difference grid. Contours: T, 0 (8·07) 80·7; ω, 0 (0·05) 0·35; ψ, 0 (0·002) 0·014; S, 0 (0·035) 0·281; Φ, 0 (0·020) 0·200; W, −27·0 (4·50) 18·0. Values in parentheses indicate contour intervals. (*b*) Model *A*3: $R_0/R_c^0 = 13{\cdot}3$. Steady-state solution obtained on a 24×24 finite-difference grid. Contours: T, 0 (19·4) 194; ω, 0 (0·30) 2·10; ψ, 0 (0·013) 0·091; S, 0 (0·0365) 0·292; Φ, 0 (1·77) 17·7; W, − 160 (40·0) 200. (*c*, *d*) Model *A*7: $R_0/R_c^0 = 160$. Time-dependent solution obtained on a 48×48 finite-difference grid. Two views are shown at times t_1 (*c*) and t_2 (*d*). $t_2 - t_1 = 1{\cdot}33$ dimensionless time units (about $\frac{1}{3}$ of an overturn time). Contours: T, 0 (99·5) 995; ω, 0 (1·25) 8·75; ψ, 0 (0·0344) 0·275; S, 0 (0·151) 1·21; Φ, 0 (37·5) 375; W, − 1200 (300) 1500.

initial density ρ_0 and typical dimension $(\Delta x)_0$, falling a distance δ through an adiabatically stratified layer. If the temperature of the parcel is initially less than the environment by an amount $(\Delta T)_0$, then an order of magnitude estimate of the initial vorticity ω_0 is $\rho_0(\Delta T)_0/(\Delta x)_0^2$ [obtained from (51)]. Ignoring conductive or frictional heat gain, the temperature difference at depth δ is

$$(\Delta T)_\delta = (\Delta T)_0 \exp(1-\delta) D/\Gamma > (\Delta T)_0.$$

Since conservation of mass in two dimensions requires $\rho \Delta x^2$ to be constant, and $(\Delta x)_\delta < (\Delta x)_0$, $\omega_\delta > \omega_0$. In the reverse situation of a hot parcel of fluid with a dimension and excess temperature of $(\Delta x)_0$ and $(\Delta T)_0$, rising a distance of δ, $(\Delta T)_\delta < (\Delta T)_0$ and $(\Delta x)_\delta > (\Delta x)_0$ so that $\omega_\delta < \omega_0$. Thus comparing two plumes of comparable positive and negative buoyancy, the cold plume becomes narrower and generates more vorticity as it falls while the hot plume becomes wider and generates less vorticity as it rises. Though undoubtedly too simple, this argument can explain the major qualitative features of plume behaviour.

The combined effects of a more pronounced upper boundary layer and the narrowing of the downgoing plume produces vertical velocities which are larger in the descending plumes than in the rising plumes. Conservation of mass thus requires that the centre of circulation be shifted towards the cold plume (figure 11*c*). In his numerical study of compressible gases, Graham (1975) also found higher velocities in the descending plumes and a shift of the centre of circulation towards the higher velocities.

The role played by the upper boundary layer in the time dependence of model *A*7 is also indicated in the plots of vorticity in figures 11 (*c*, *d*). The zone of large vorticity surrounding the descending plume remains essentially unchanged. The upper boundary layer instabilities develop as cold parcels of liquid which either fall through the layer, breaking up the convection rolls, or get swept across to the nearest downgoing plume. The latter behaviour occurs in model *A*7, causing pulses of high velocity in the descending plumes.

An important feature of compressible convection in viscous fluids is the viscous dissipation of mechanical energy, which must play an important role in local energy balances. Contours of Φ are shown in figure 11. Most of the shear heating is concentrated into narrow zones near the vertical boundaries and in the corners where the liquid is forced to turn sharply. The more dominant descending plume produces more frictional heating at the lower right than does the rising plume at the upper left. The contours of Φ in figure 11 are similar to those computed by Hewitt *et al.* (1975) for a Boussinesq liquid with $d/H_T = 0{\cdot}117$. The major difference is the asymmetry of diagonally opposite corners in figure 11 which is not apparent in Hewitt *et al.*'s incompressible results. However their results for models with partial internal heating look qualitatively similar to those presented here due to a similar asymmetry in the plume structure. The flow solutions of the series *A* models ($d/H_T = 0{\cdot}25$) do not show any obvious influence of the viscous dissipation on their structure.

In steady state the global integral of Φ must balance the global integral of the rate of work done against the adiabatic gradient. Equation (54) shows that the latter quantity is proportional to the integral of $\rho_r C_p T w$. Contours of a dimensionless function, W, proportional to $\rho_r C_p T w$ (figures 11*a–d*) show a relatively smooth distribution in contrast to those of Φ.

(*b*) *Series B* ($d/H_T = 0{\cdot}50$). Unlike series *A*, most of the models of series *B* have time-dependent solutions. Time dependence of the final solution occurs in models *B*6–*B*11, model *B*6 having a ratio of Rayleigh number to critical Rayleigh number R_0/R_c^0 equal to the relatively low value of 6·3.

Figures 12(*a*) and 12(*b*) show the steady-state solutions for models *B*1 and *B*3. In model *B*1, convection is very weak ($R_0/R_c^0 = 1{\cdot}07$, $N = 1{\cdot}03$) and concentrated in the upper part of the layer. Weak counter-cells at the bottom, stable part of the layer, driven by viscous coupling to the major cells above, can be seen in the stream function contours of figure 12(*a*). Values of ψ in the small counter-cells are about two orders of magnitude smaller than in the upper cells. Penetration of the downgoing plumes into the stable lower layer is indicated by the asymmetry of the larger cells seen in the stream function and vorticity contours.

As the Rayleigh number is increased, the convecting region penetrates deeper into the layer. For model *B*3, with $R_0/R_c^0 = 1{\cdot}9$, the entire layer is convecting (figure 12*b*). However as revealed by the graph of relative contributions to the total heat flux in figure 14, convection in the lower region is still quite weak and nowhere in this model does convective exceed conductive heat transport.

Models *B*1–*B*8 were all begun with a single convection cell occupying the entire box. Models *B*1–*B*4 rapidly broke up into two cells before settling down to a steady-state two-cell convection pattern. A similar tendency for single cells to break up into multiple cells was noted by McKenzie *et al.* (1974) in their internally heated Boussinesq models. At higher Rayleigh numbers, the flow is sufficiently vigorous to form bottom boundary layers similar to the heated-from-below Boussinesq models.

A single time-dependent cell persisted in models *B*6–*B*8 with behaviour similar to, but more pronounced than, that of model *A*7 discussed above. Instabilities of the upper boundary layer are swept into the downgoing plume causing pulses in the vertical velocities. As the Rayleigh number is increased the pulses become larger and more frequent. The time-dependent nature of the solutions of these models is clearly seen in figures 12(*c*, *d*) which shows two views of model *B*7 at different times. At time t_1 an instability is being swept down the right-hand side of the box. A region of large vorticity is associated with the downgoing plume and, unlike the series *A* models, a small region of vorticity of opposite sign exists in the central region. The asymmetry of the plume structure, shown by the vorticity field, is more pronounced in the series *B* than in the series *A* models. Contours of Φ in figure 12(*c*) show that internal heating by friction is concentrated near the descending plume. As a result of this localized heating, a rise in isotherms adjacent to the descending plume persists down to the bottom of the layer rather than dying out towards the bottom as would be expected. Consequently a small temperature gradient is generated across the cell of opposite sign to that caused by the plumes at the edges, hence the opposite sign of the vorticity in the central region.

At time t_2 in figure 12(*d*), the bulk of the cold instability has reached the bottom of the layer and vertical velocities in the plume are less. Frictional heating in the bottom right-hand corner has generated a noticeable kink in the isotherms. This in turn results in a larger reversed vorticity in the central region and accounts for the concave shape of the stream function contours. Thus at $d/H_T = 0{\cdot}50$, viscous dissipation directly affects the flow patterns. For model *B*7, $R_0/R_c^0 = 12{\cdot}6$; this is

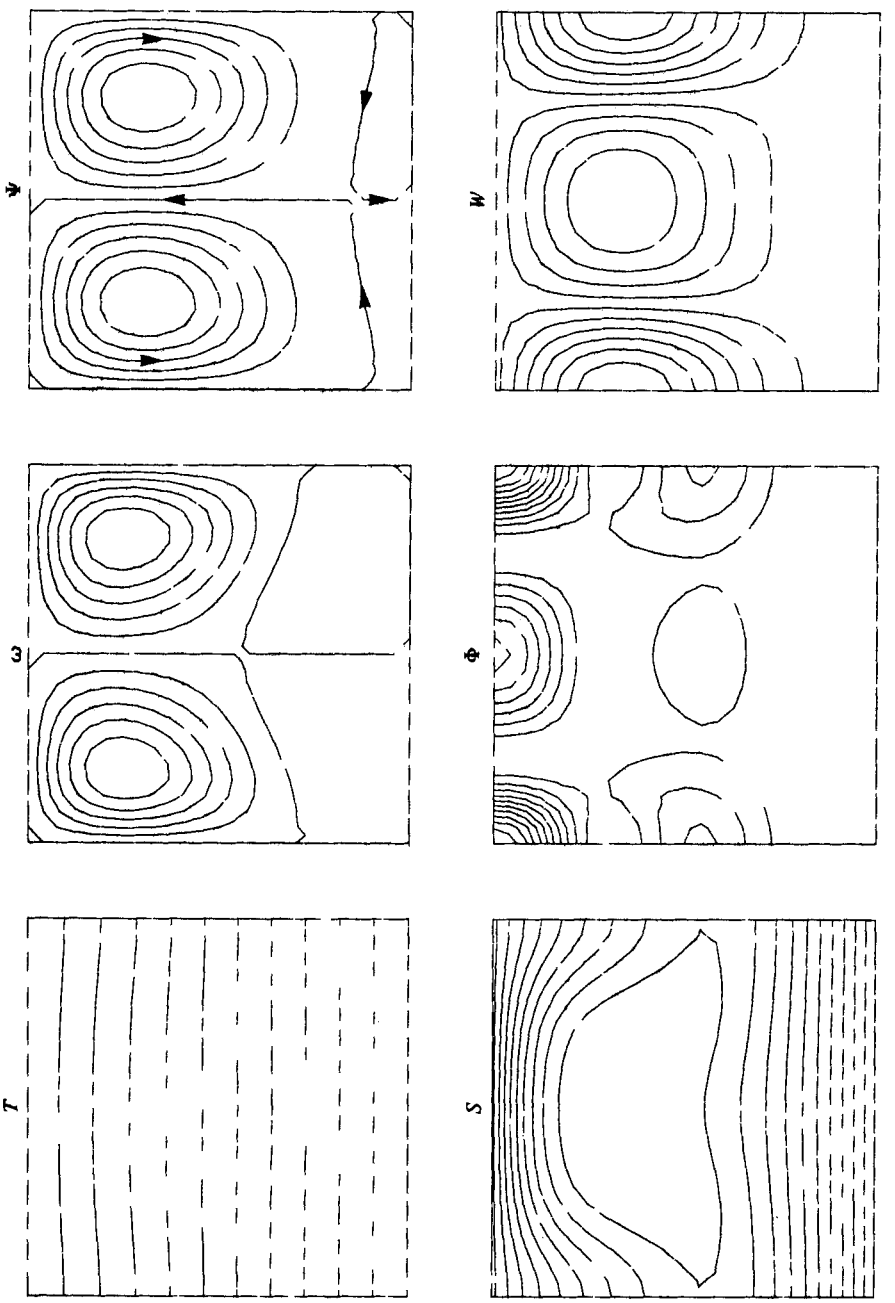

(*a*)

For legend see p. 556–7.

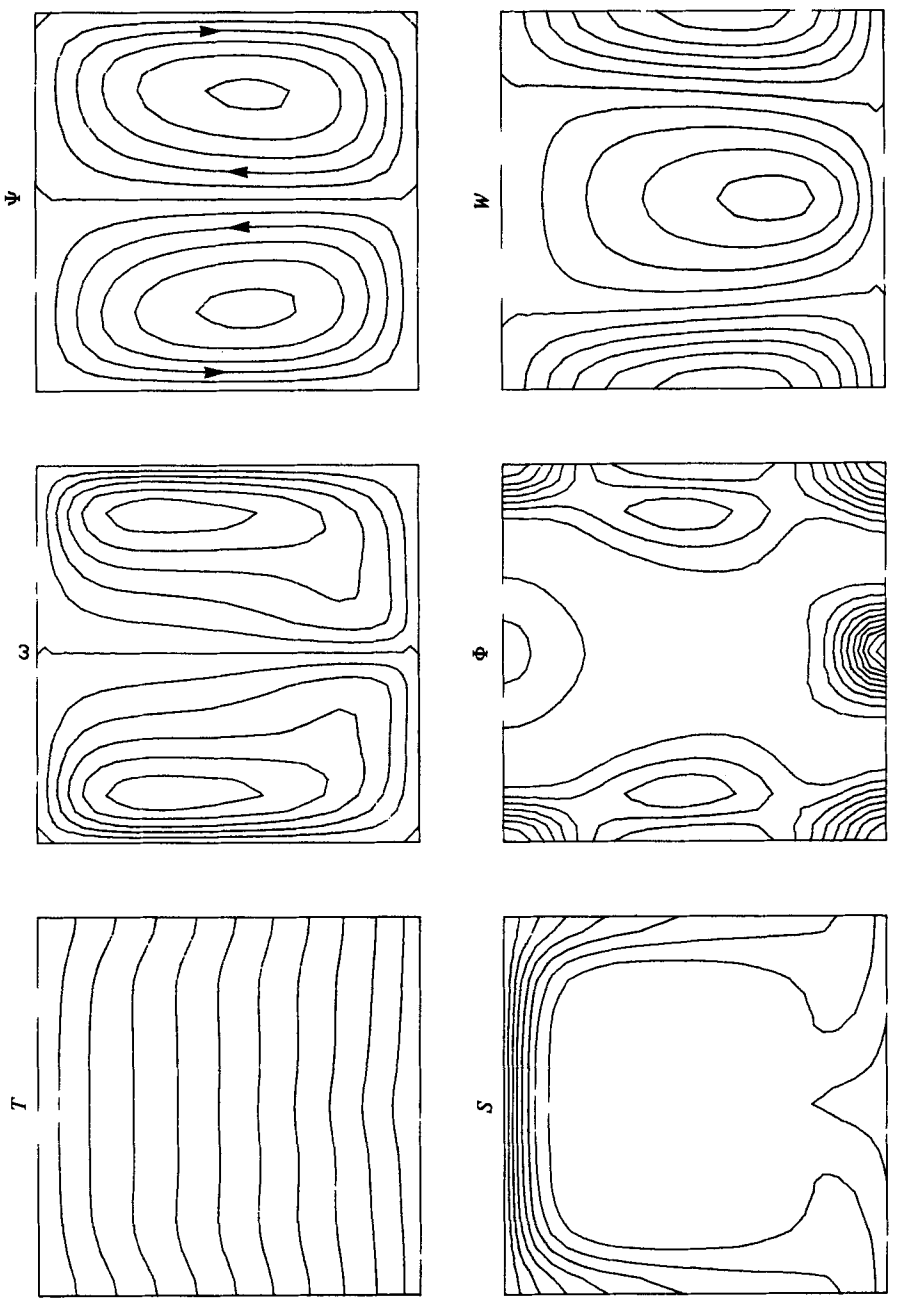

(b)

For legend see p. 556–7.

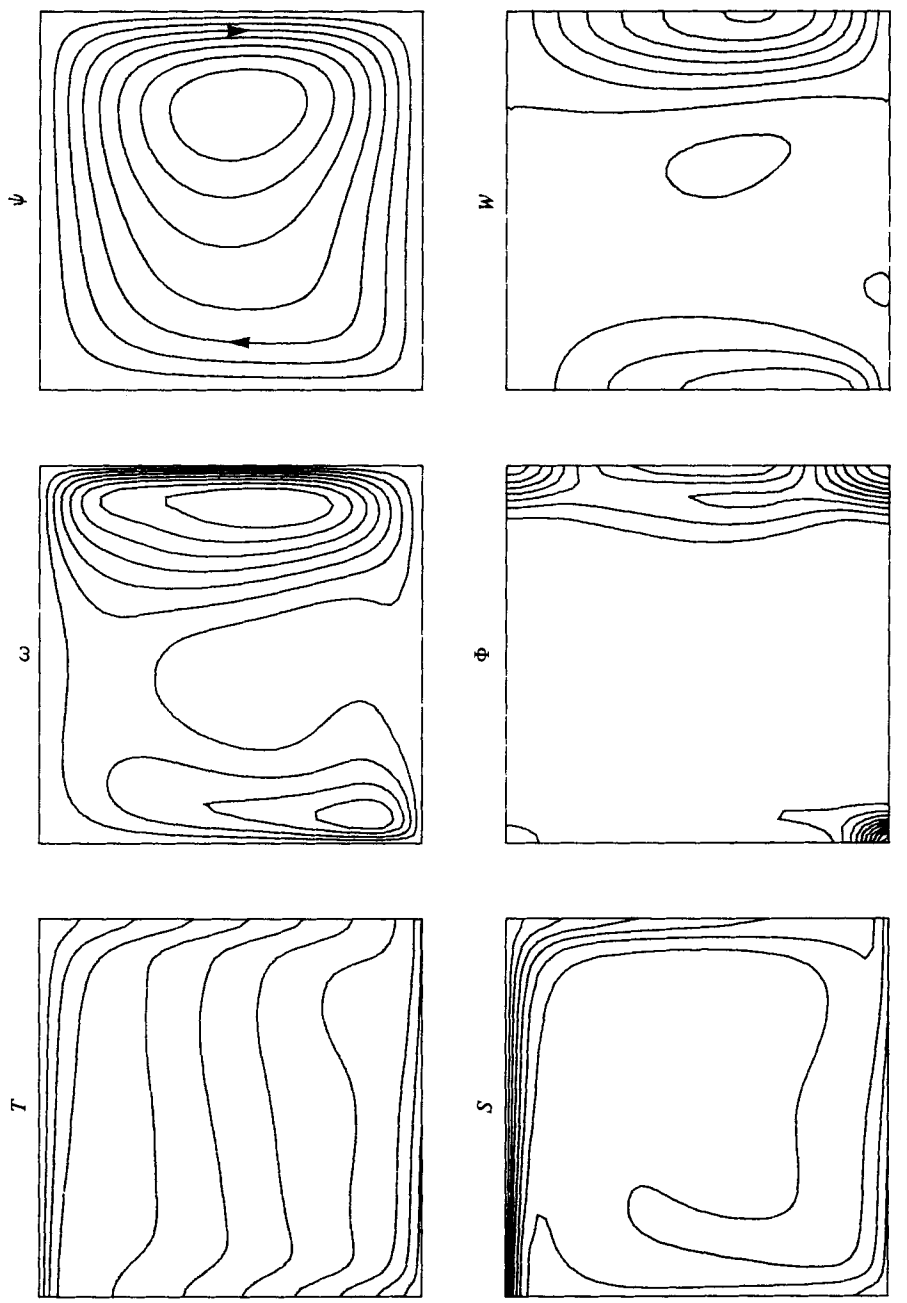

(*c*)

For legend see p. 556–7.

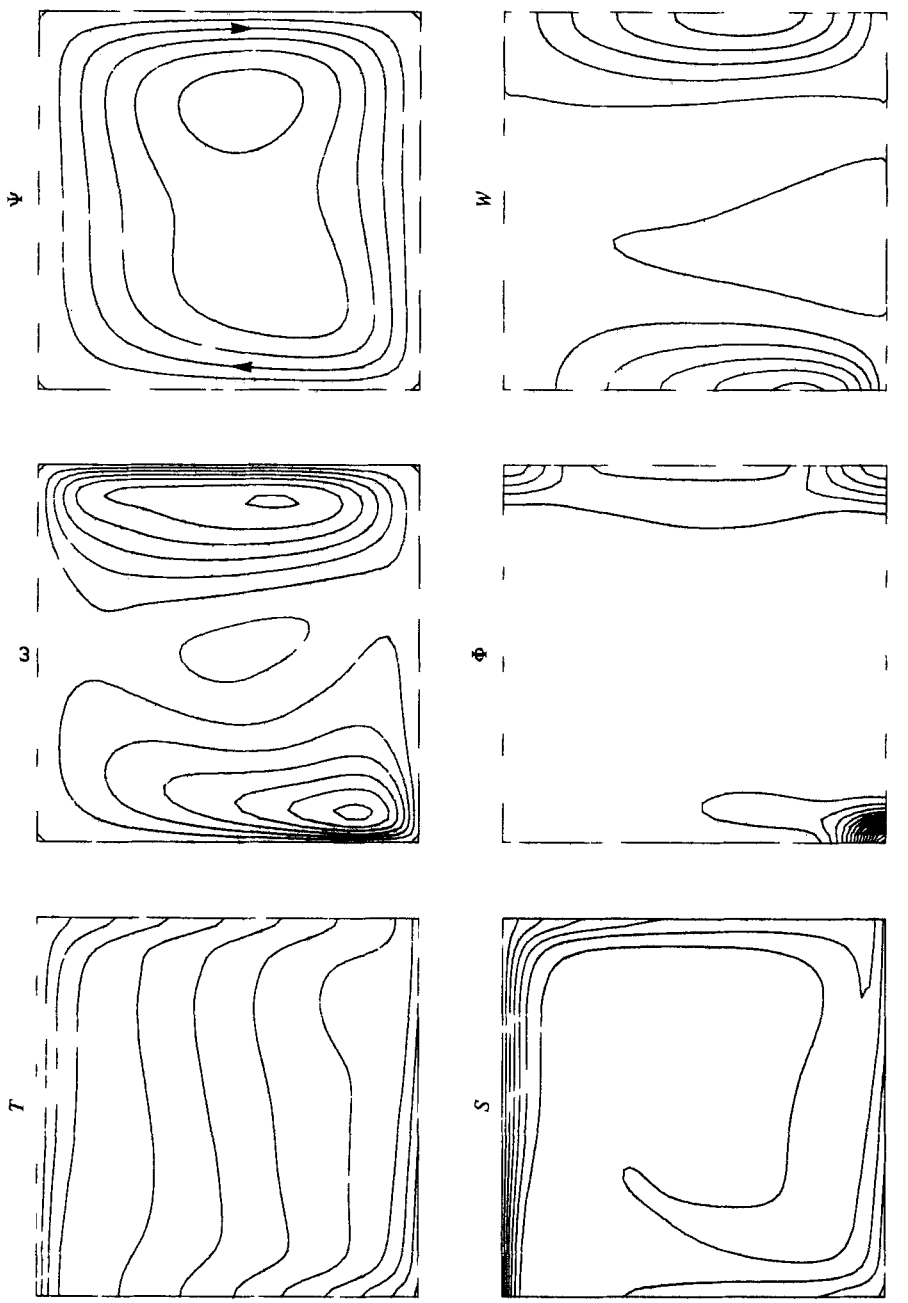

FIGURE 12. Numerical solution of anelastic models with $d/H_T = 0{\cdot}50$ (series B). Contours plot dimensionless temperature T, vorticity ω, stream function ψ, entropy S, rate of viscous dissipation Φ and vertically convected heat flux W. (*a*) Model $B1$: $R_0/R_c^0 = 1{\cdot}07$. Steady-state solution obtained on a 24×24 finite-difference grid. Contours: T, 0 (15·9) 159; ω, $-0{\cdot}136$ (0·0273) 0·136; ψ, $-0{\cdot}0015$ (0·0003) 0·0015; S, $-0{\cdot}0018$ (0·0026) 0·0219; Φ, 0 (0·00168) 0·0168; W, $-5{\cdot}52$ (1·03) 3·75. (*b*) Model $B3$: $R_0/R_c^0 = 1{\cdot}89$. Steady-state solution obtained on a 24×24 finite-difference grid. Contours: T, 0 (19·6) 196; ω, $-0{\cdot}60$ (0·12) 0·60; ψ, $-0{\cdot}009$ (0·0018) 0·009; S, 0 (0·0092) 0·074; Φ, 0 (0·0452) 0·452; W, $-39{\cdot}5$ (7·90) 31·6. (*c*) Model $B7$: $R_0/R_c^0 = 12{\cdot}6$.

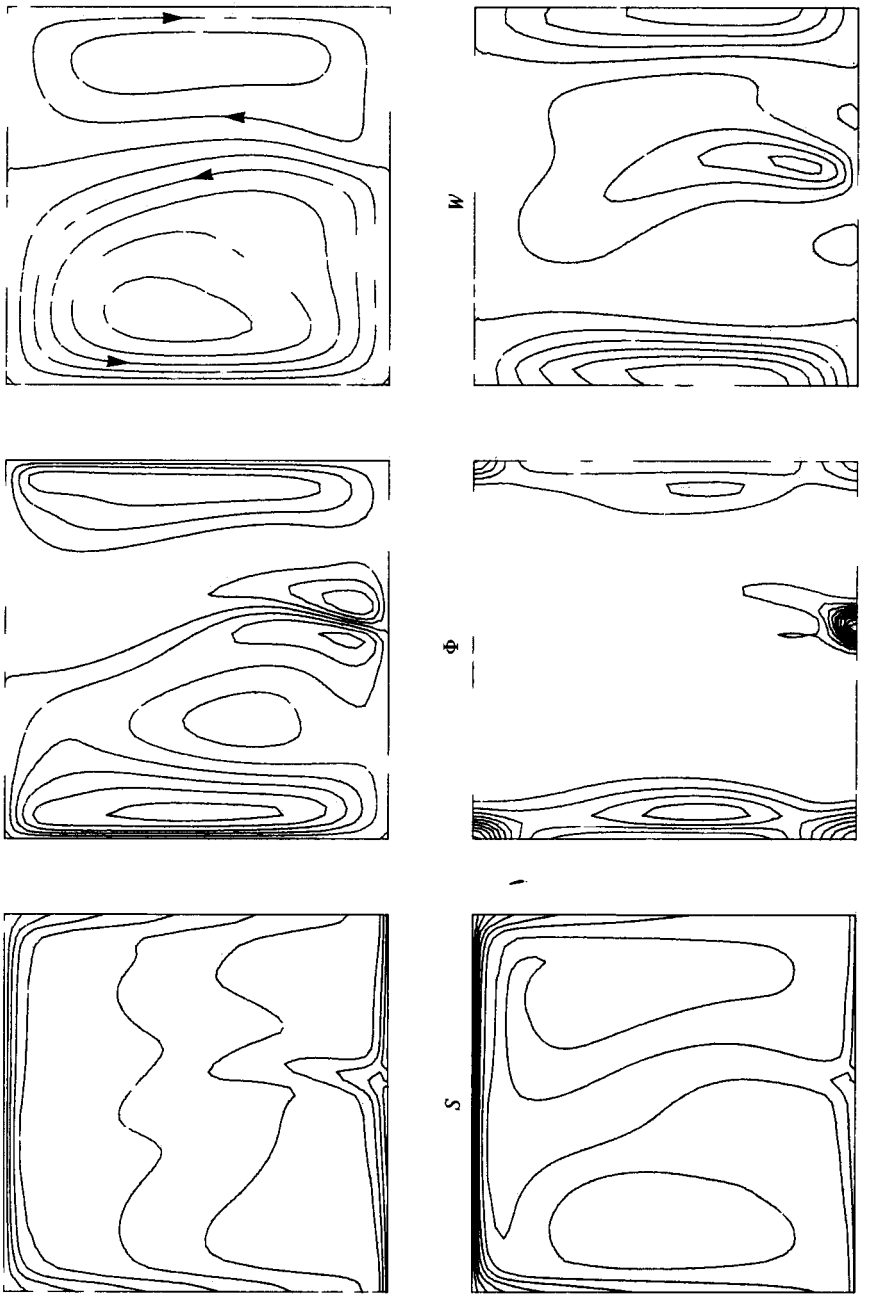

(*e*)

Time-dependent solution obtained on a 48×48 finite-difference grid. Two views are shown at times (*c*) t_1 and (*d*) t_2. $t_2 - t_1 = 2{\cdot}63$ dimensionless time units (about $\frac{1}{4}$ of an overturn time). Contours: T, 0 (39·9) 399; ω, 0 (0·488) 3·413; ψ, 0 (0·0083) 0·0581; S, 0 (0·051) 0·407; Φ, 0 (1·95) 19·5; W, −360 (60·0) 180. (*e*) Model B11: $R_0/R_c^0 = 101$. Time-dependent solution obtained on a 48×48 finite-difference grid. Contours: T, 0 (142·1) 1421; ω, −10·0 (2·00) 6·00; ψ, −0·0825 (0·0165) 0·0330; S, 0 (0·156) 1·25; Φ, 0 (14·5) 145; W, −1225 (245) 980.

approximately the same value as that for model $A3$ ($R_0/R_c^0 = 13{\cdot}3$) in which no obvious effects of viscous dissipation were observed.

Increasing the Rayleigh number through models $B9$–$B11$, instabilities developing in the upper boundary layer quickly break the original one cell into two smaller cells. These two-cell flows are also time dependent. The exact number of cells into which the original cell splits is strongly influenced by the side-wall boundaries of the model. The general trend for the upper boundary layer to become more unstable with increasing Rayleigh number and increasing value of d/H_T is however believed to be qualitatively correct.

Figure 12(*e*) shows a typical view of the solutions for model $B11$, for which

$$R_0/R_c^0 = 100.$$

Convection is vigorous with a substantial bottom boundary layer and central rising plume. As a cold instability descends the downgoing plume at the left and spreads out at the bottom, the base of the other cell is squeezed to the right. Unequal-sized cells result. Viscous heating is significant in such vigorous convection; the regions of reversed vorticity in the centres of the cells, and the concave sides of the convection cells themselves, again result from the localized heating adjacent to the descending plumes. The effects of viscous dissipation are also registered on the entropy contours as regions of increased entropy adjacent to the downgoing plumes.

(*c*) *Series C* ($d/H_T = 1{\cdot}00$). The series C models all have time-dependent solutions with the exception of models $C1$ and $C2$, which convect marginally with values of $R_0/R_c^0 = 1{\cdot}1$ and $1{\cdot}2$ and $N = 1{\cdot}01$ and $1{\cdot}03$ respectively. Models $C1$–$C8$ were all begun with an initial roll occupying the whole box which quickly broke up into smaller rolls. Models $C9$–$C13$ were each begun with the final solutions of the previous model in the series.

Figure 13(*a*) shows the steady-state solution of model $C1$. As in model $B1$, the variation of the adiabatic gradient across the layer stabilizes the lower regions. The effect is more pronounced in model $C1$ however, and convection is restricted to the upper half of the layer. The entropy contours indicate the region of buoyant convection as an isentropic layer overlying a gravitationally stable zone. The zero contours of ψ reveal three pairs of counter-cells (of decreasing strength with depth) driven by viscous coupling to the upper convection cells. The descending limbs of the upper convection cells penetrate into the stable region and distort the first pair of counter-cells. This can be seen most clearly in the contours of ω. The first pair of counter-cells, however, do not distort the lower cells in the same manner. Figure 14 shows that convective heat transport is negligible in the lower half of the layer in this model, and contributes less than 25 % to the total heat flux in the upper half.

A preferred roll aspect ratio of approximately unity may account for two rolls having developed in the upper region. The variation of adiabatic gradient across the unstable layer acting as an internal heat source may also tend to reduce the aspect ratio. This effect however appears to be more important in models $C5$ and $C6$, in which convection extends to the bottom of the layer.

As the Rayleigh number is increased, the main convection cells penetrate deeper into the stable bottom layer and the flow becomes time dependent at relatively low Rayleigh numbers. Figure 13(*b*) shows a typical view of the solutions for model $C4$.

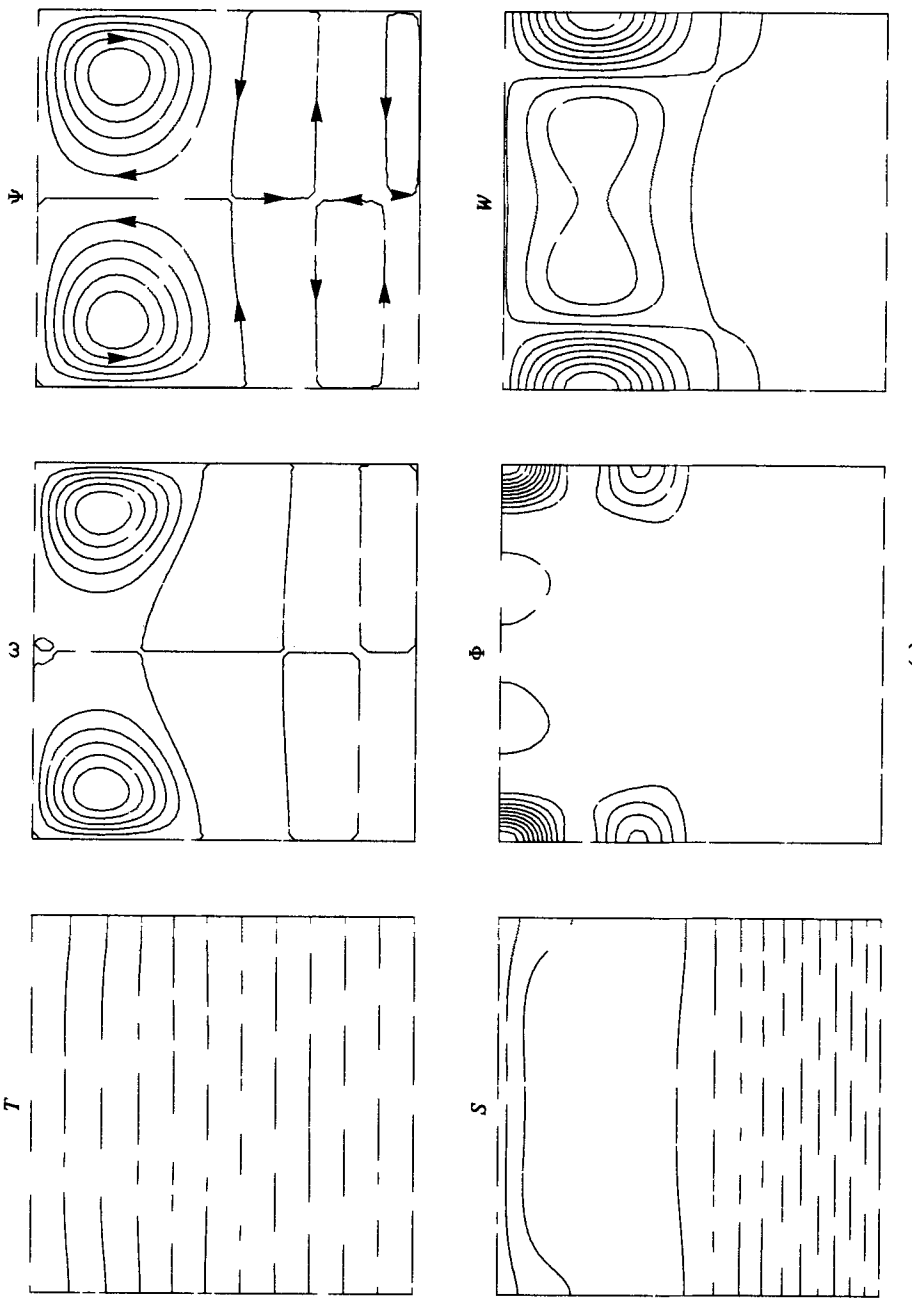

(*a*)

For legend see p. 563–4.

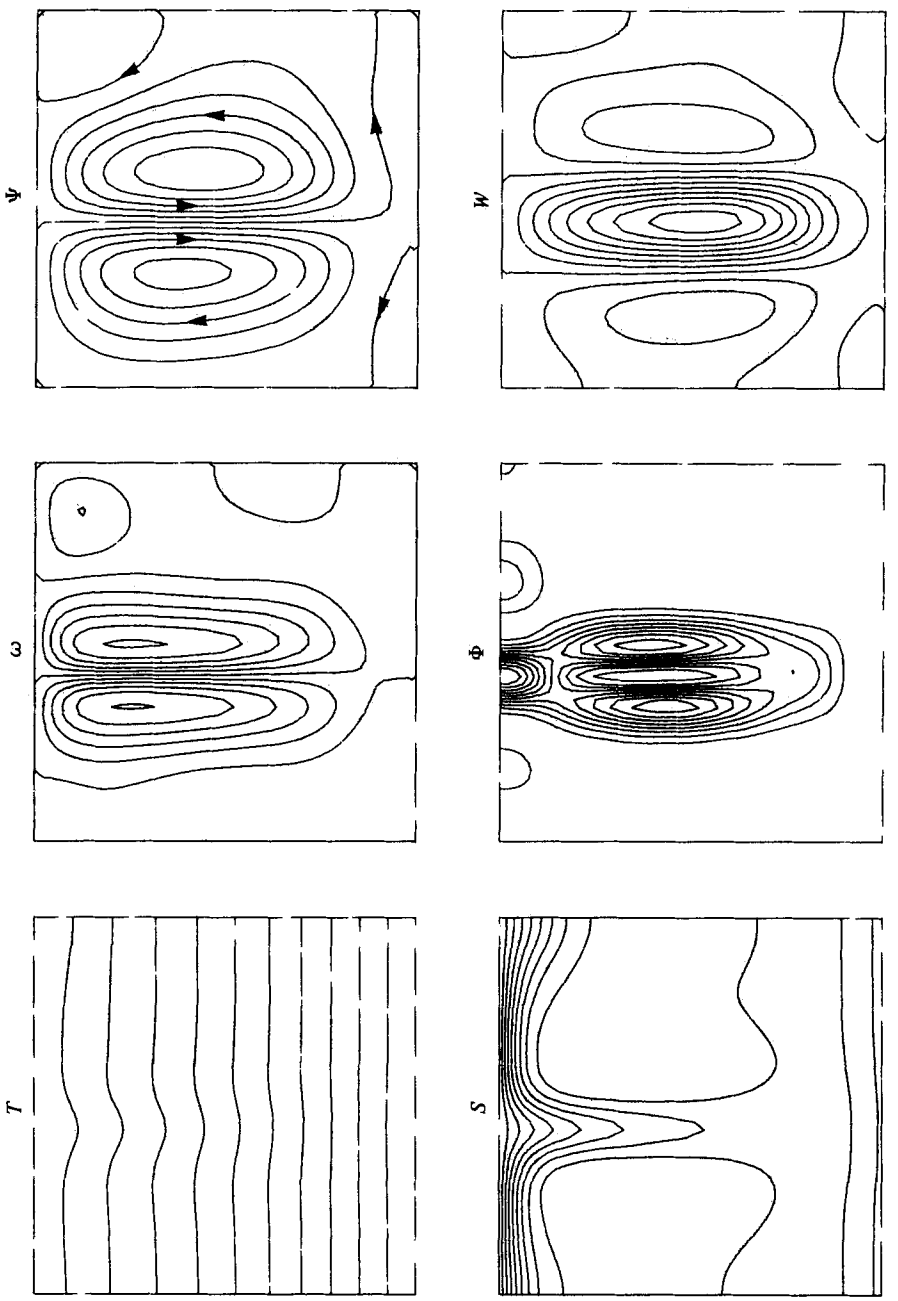

(b)

For legend see p. 563–4.

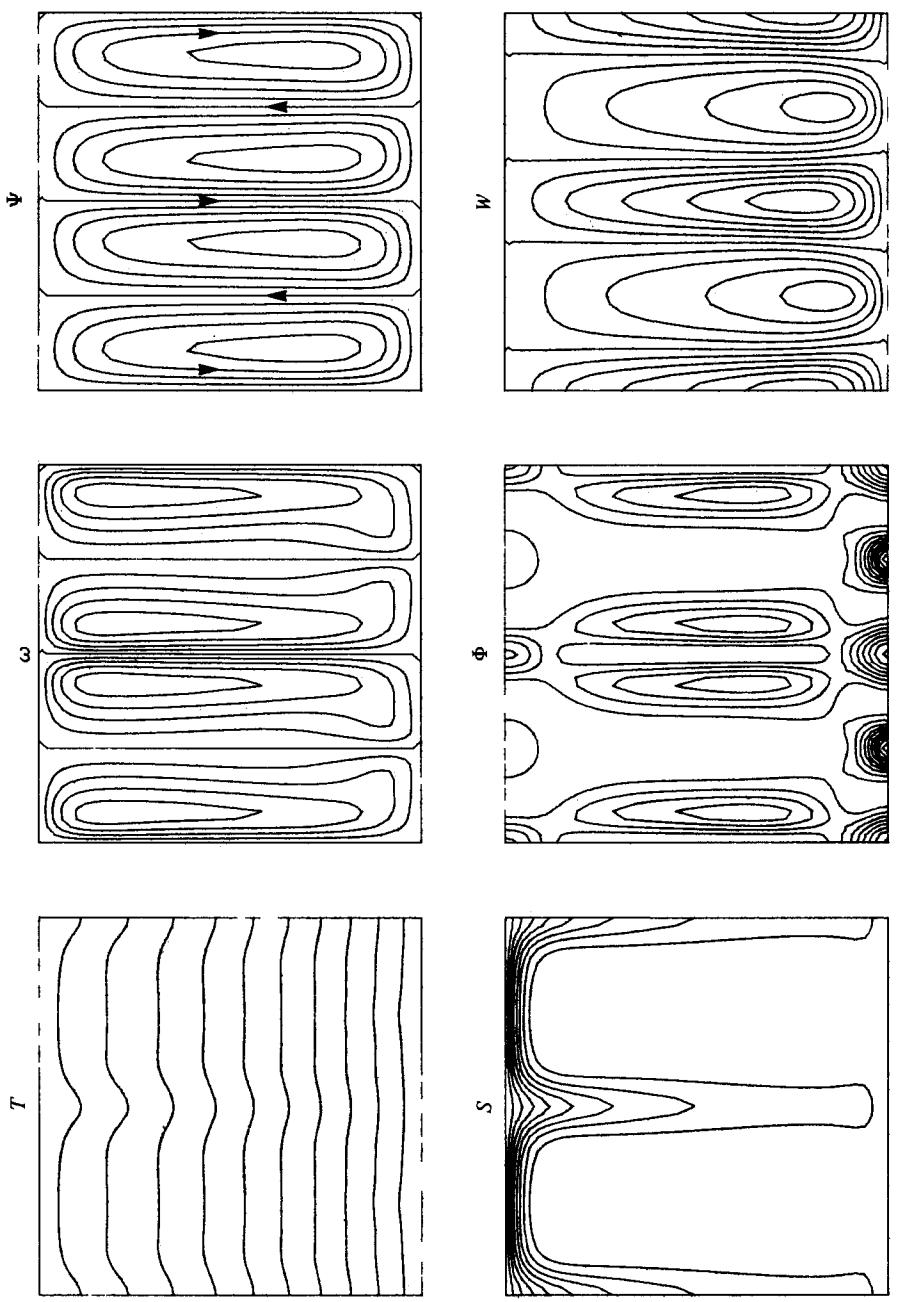

(*c*)

For legend see p. 563–4.

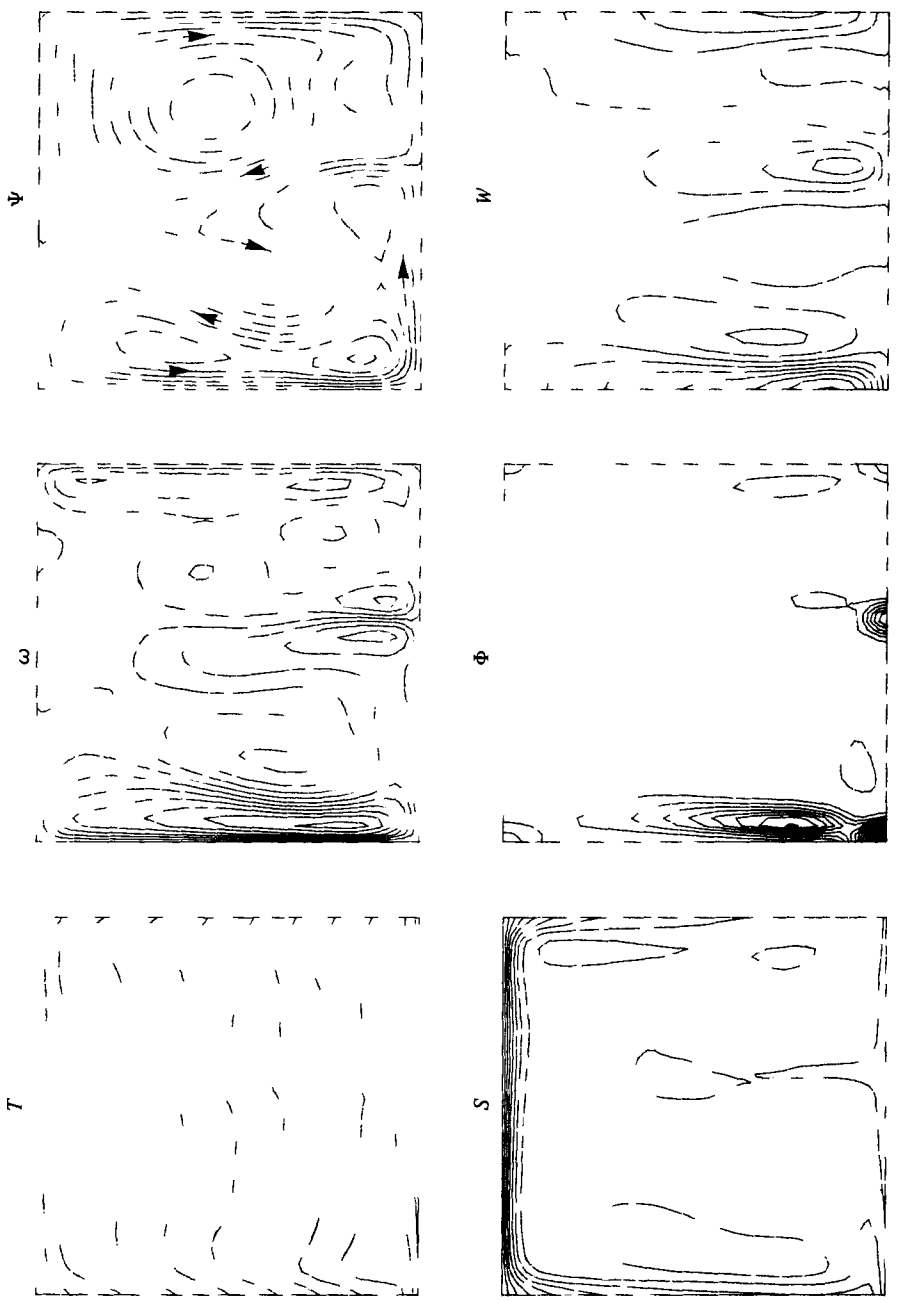

(d)

For legend see p. 563–4.

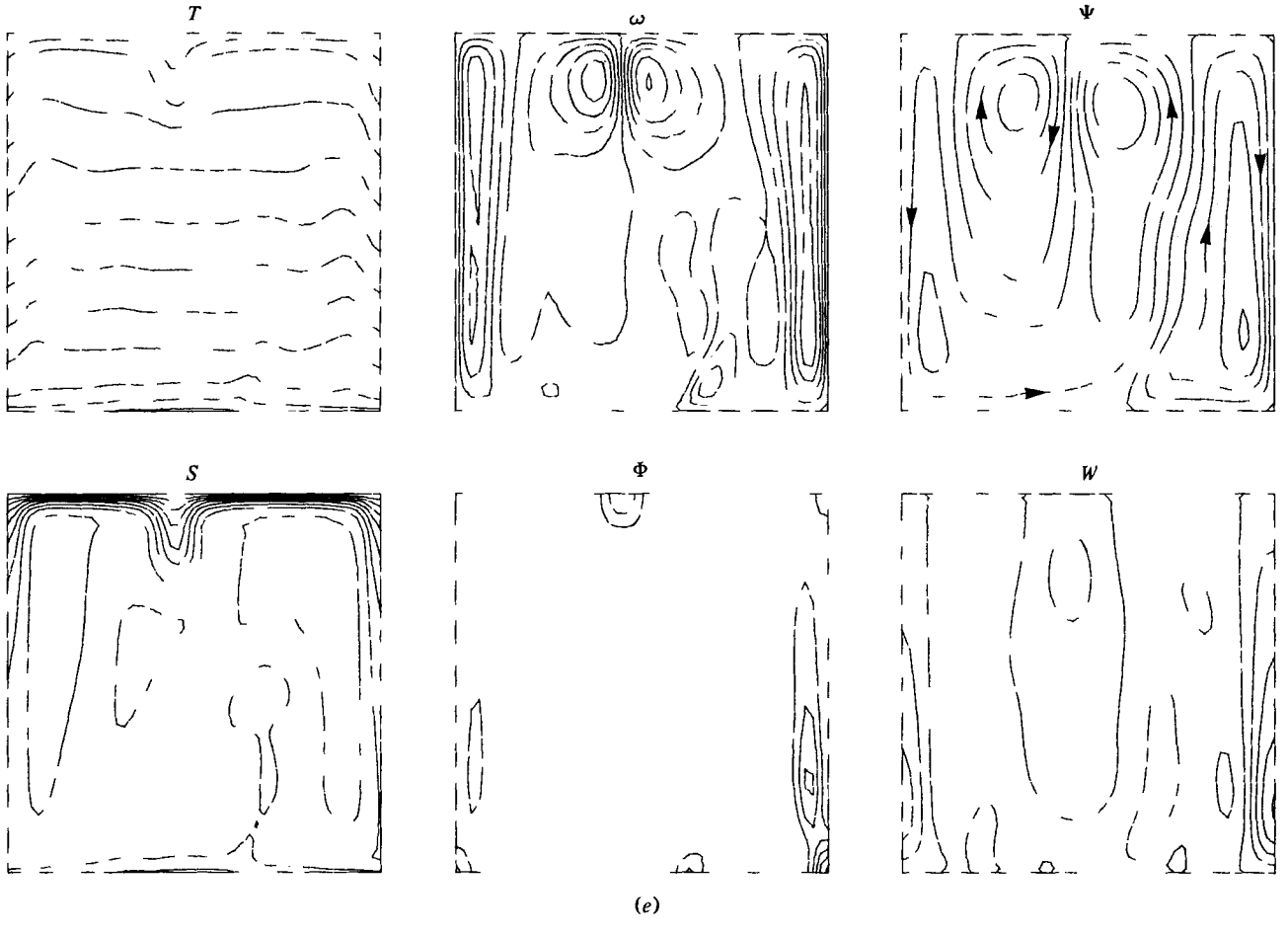

FIGURE 13. Numerical solution of anaelastic models with $d/H_T = 1{\cdot}00$ (series C). Contours plot dimensionless temperature T, vorticity ω, stream function ψ, entropy S, rate of viscous dissipation Φ and vertically convected heat flux W. (*a*) Model $C1$: $R_0/R_c^0 = 1{\cdot}07$. Steady-state solution obtained on a 48 × 48 finite-difference grid. Contours: T, 0 (34·4) 344; ω, −0·1755 (0·0351) 0·1755; ψ, −0·00066 (0·00013) 0·00066; S, −0·114 (0·016) 0·026; Φ, 0 (0·00119) 0·0119; W, −5·94 (0·863) 1·82. (*b*) Model $C4$: $R_0/R_c^0 = 1{\cdot}78$. Time-dependent solution obtained on a 48 × 48 finite-difference grid. Contours: T, 0 (47·6) 476; ω, −0·685 (0·137) 0·685; ψ, −0·0025 (0·00050) 0·0025; S, 0 (0·0121) 0·0968; Φ, 0 (0·0125) 0·125; W, −38·5 (5·50) 11·0. (*c*) Model $C6$: $R_0/R_c^0 = 2{\cdot}97$. Time-dependent solution obtained on a 48 × 48 finite-difference grid. Contours: T, 0 (54·9) 549; ω, −0·80 (0·20) 0·80; ψ, −0·00268

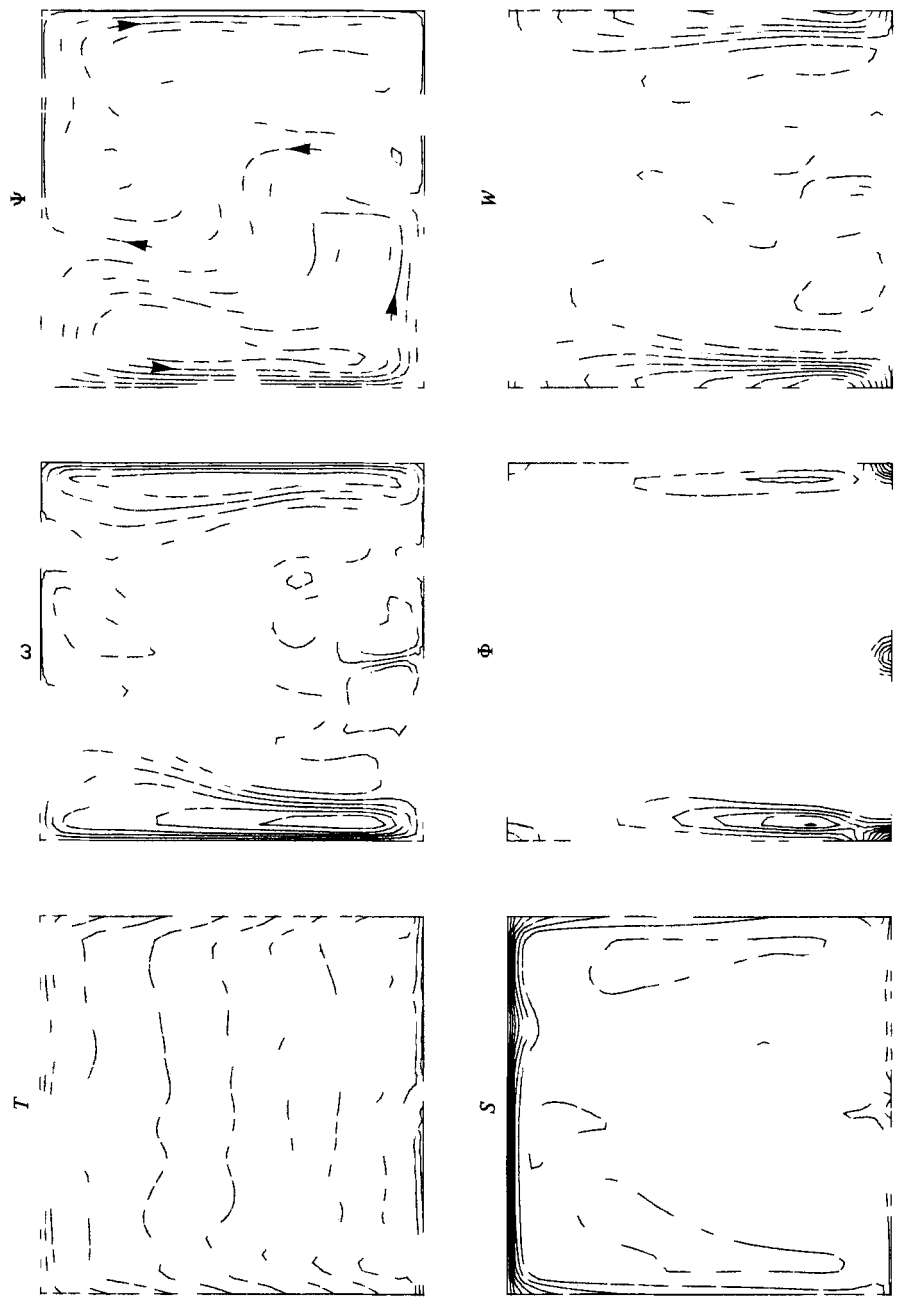

(0·00067) 0·00268; S, 0 (0·0186) 0·149; Φ, 0 (0·0601) 0·601; W, −65·0 (13·0) 52·0. (*d*, *e*) Model *C*10: $R_0/R_c^0 = 14{\cdot}9$. Time-dependent solution obtained on a 48 × 48 finite-difference grid. Two views shown at times (*d*) t_1 and (*e*) t_2. $t_2 - t_1 = 20{\cdot}5$ dimensionless time units (about 1 overturn time). Contours: T, 0 (95·0) 1045; ω, −4·893 (0·699) 2·796; ψ, −0·0108 (0·0018) 0·0126; S, 0 (0·0638) 0·574; Φ, 0 (1·65) 33·1; W, −540 (90·0) 270. (*f*) Model *C*13: $R_0/R_c^0 = 47{\cdot}6$. Time-dependent solution obtained on a 48 × 48 finite-difference grid. Contours: T, 0 (187·2) 1872; ω, −8·31 (1·68) 5·11; ψ, −0·020 (0·004) 0·013; S, 0 (0·127) 1·018; Φ, 0 (8·80) 88·0; W, −1423 (231) 656.

Although the streamlines almost reach the bottom of the box, convection is very weak at the deepest points (figure 14) and nowhere contributes more than 33 % to the total heat flux. In such weakly convecting systems, the effect of convection on the temperature field is best revealed by the contours of entropy. The central descending plume and upper boundary layer can be seen in the entropy contours of figure 13(*b*). An adiabatic region on either side of the plume and a gravitationally stable lower layer are also indicated. At the upper right a boundary-layer instability is forming. This will eventually fall through the fluid generating an additional, but transient, roll. The absence of any rising plume is apparent in the contours of both ω and S.

Early in the development of models $C5$ and $C6$ instabilities of the upper boundary layer break the flow pattern into four time-dependent rolls which persist from then on, the relative sizes and positions shifting with time. Figure 13(*c*) shows the solutions of model $C6$ at one time. Convection extends throughout the layer in this model and in the upper half of the layer transports more heat than conduction. In the lower regions conduction is still the dominant heat transfer mechanism (figure 14).

As the Rayleigh number is increased, convection becomes more vigorous and gravitationally unstable boundary layers develop at the bottom of the layer. The variation of adiabatic gradients across the layer becomes less important and the model solutions look less like those of internally heated models. As in series B, once the Rayleigh number is sufficiently high for vigorous convection to occur throughout the layer, fewer rolls occupy the box than in the weakly convecting models. Models $C7$–$C13$ all have two main rolls occupying the box. However cold parcels of liquid intermittently breaking away from the unstable upper boundary layer and falling through the convection cells create temporary but complex flow patterns consisting of three or four smaller rolls. The frequency of these disruptions increases with Rayleigh number.

Figures 13(*d*, *e*) show solutions for model $C10$, for which $R_0/R_c^0 = 15$, at two different times. At time t_1 two rolls occupy the box. The extremely concave side of the left-hand roll is a result of intense frictional heating adjacent to the descending plume. The temperature contours show a marked local rise in temperature next to the descending plumes which is most intense at the left. This generates vorticity of the opposite sense to the main circulation of the left-hand cell. Concave streamlines result. The same, though less intense, effect occurs in the right-hand cell. At time t_2, in figure 13(*e*), an instability has developed in the unstable boundary layer. This recurrent formation of cold 'thermals' resembles Howard's (1966) description of time-dependent convection.

Figure 13(*f*) shows one view of the time-dependent solution for model $C13$. This model has a value of $R_0/R_c^0 = 48$, the largest in series C, and is at the limits of resolution of the numerical scheme on a 48×48 finite-difference grid. Qualitatively the solution is quite similar to those shown in figures 13(*d*, *e*) for model $C10$. The flow is more vigorous and the upper boundary more unstable.

(*d*) *Series A–C: summary.* The most striking result of increasing the compressibility factor d/H_T through series A to C is the development of time-dependent flow at relatively low Rayleigh numbers. Schlüter, Lortz & Busse (1965) first showed that two-dimensional rolls were the only stable stationary solutions of the Boussinesq equations of motion at Rayleigh numbers close to the critical value. For rigid

boundaries Busse (1967, 1971) and Clever & Busse (1974) determined the region of stability of two-dimensional rolls in the Rayleigh number, wavenumber plane, and gave theoretical descriptions of the instabilities defining the boundaries. These authors considered perturbations of the form $e^{i(dx+by)}$, where d and b are horizontal wavenumbers, applied to rolls aligned in the y direction. For given values of Rayleigh number, k and b, Busse (1967) found that rolls were most unstable to disturbances for which $d = 0$. This is of particular relevance to our two-dimensional numerical model since only disturbances with $b = 0$ and $d \neq 0$ are possible. At high Prandtl numbers, the stability boundary defined by this, the Ekhaus type of instability, lies outside those for the three-dimensional zig-zag instability (at low wavenumbers) and cross-roll instability (at high wavenumbers) (Busse 1971; Clever & Busse 1974). Consequently our numerical solutions are artificially stabilized with respect to the latter two types of disturbances. Furthermore the horizontal periodicity of the mathematical model eliminates all Eckhaus disturbances with $k < \pi/\lambda$, where λ is the dimensionless width of the box.

Straus (1972) and Skilbeck (1976) found that the region of stability (of two-dimensional rolls) is extended to higher Rayleigh numbers when free boundaries are assumed. The simplifications of the numerical model thus all tend to stabilize the flow. Nevertheless time-dependent solutions occur for values of R_0/R_c^0 as low as 1·5 in series C ($d/H_T = 1{\cdot}00$) and 6·3 in series B ($d/H_T = 0{\cdot}50$). The series A models ($d/H_T = 0{\cdot}25$) behave more like incompressible solutions with steady flows persisting up to $R_0/R_c^0 = 107$. It may be concluded that for each series of numerical solutions, the Rayleigh number at which time-dependent flow first occurs is probably an upper bound to the range of Rayleigh numbers for steady flow, and that the region of stability in the Rayleigh number, wavenumber plane diminishes with increasing d/H_T.

The fact that all the vigorously convecting models of series B and C have time-dependent solutions illustrates the importance of retaining the time-dependent terms in the equations. Although steady-state solutions obtained after discarding all partial time-derivatives will satisfy the governing equations (Turcotte *et al.* 1974), so will a purely conductive solution. A somewhat surprising result obtained from the series B and C solutions is the close balance of the overall rates of viscous dissipation and work done in adiabatic volume changes at all times during non-steady flows. In the anelastic–liquid approximation the non-hydrostatic pressure P_1 is ignored in the thermal energy equation. Thus integrating (5) (with no internal heat generation) over the volume V of the convecting region gives

$$\int_V \rho C_p \frac{DT}{Dt} dV = \oint_S K \nabla T . \mathbf{n}\, dS + \Phi + \int_V \alpha T \mathbf{u} . \nabla P_H \, dV, \tag{59}$$

where the operator $D/Dt = (\partial/\partial t + \mathbf{u} . \nabla)$ is the total derivative following the motion, S is the surface bounding V, $\mathbf{n}$ is an outward pointing unit vector normal to S and Φ represents the volume integral of $\tau_{ij} \partial u_i / \partial x_j$. Applying Reynolds' transport theorem to the left-hand side and expanding the last term on the right of (59) we have

$$\frac{d}{dt} \int_V \rho C_p T \, dV = \oint_S K \nabla T . \mathbf{n}\, dS + \Phi - \frac{d}{H_T} F_a, \tag{60}$$

where $F_a = \overline{A \langle \rho_r C_p T w \rangle}$ is the overall average of the vertically convected heat flux (the overbar representing a vertical average). Under steady-state conditions the left-

hand side of (60) and the first term on the right both vanish; equation (54) results. The first term on the right vanishes because, in the absence of internal heat sources, an equal flux is conducted out of the top boundary as is conducted in through the bottom. In the time-dependent models, however, a constant heat flux is maintained at the bottom boundary (as a boundary condition) while the heat conducted through the upper boundary layer changes with time as instabilities develop within the layer. Consequently the left-hand side and first term on the right of (50) are both non-zero in the time-dependent case. Nevertheless the numerical results of the time-dependent models indicate that (54) continues to hold true regardless of the nature of the flow (see table 7). The mean magnitude of the last two terms of (59), V_M, and their ratio, V_R, are plotted against time in figure 8 for typical time-dependent models. Although the magnitude of these terms may vary widely with time, their ratio remains very nearly unity.

For steady-state models, the percentage deviation of the two volume integrals of (54), dV, was used as a measure of the internal consistency of the numerical scheme. The constancy of energy flux through the layer was another internal check. The latter indicator is lost in the time-dependent models since at any time the heat flux may vary significantly with depth. However since (54) remains approximately valid for the time-dependent solutions, dV continues to be a useful monitor of the numerical scheme. Values of dV are tabulated for all models in table 7 along with dF for the steady-state models.

Another distinctive feature of the above results is the effect of variation of adiabatic gradients across the layer on models with relatively low values of R_0/R_0^c. Figure 14 shows plots of the conductive and convective contributions to the total energy flux F' through the convecting regions for each of the three series. In the series A models (figure 14a), with $d/H_T = 0{\cdot}25$, there is no visible effect of the adiabatic variation on the strength of convection in the lower regions. In figure 14(b) for series B, the marginally convecting model $B1$ is seen to be convecting only in the upper regions. At a slightly higher Rayleigh number, model $B3$ is convecting (weakly) throughout the layer with a convective flux which decreases with depth. A similar but more extreme reduction of convective flux with depth is shown in figure 14(c) for the low Rayleigh number models of series C.

Also included in the plots of figure 14 is the contribution by viscous stresses to the total vertical energy flux [see (52)]. The magnitude of this source of energy flux never exceeds 2·5 % for any of the models studied and it would therefore provide a relatively unimportant means of energy transport.

The importance of viscous *heating* however clearly increases with d/H_T. In the series A models, shear heating is insignificant, whereas, in the vigorously convecting models of series C, local heating near descending plumes is of sufficient intensity to modify both temperature and flow solutions. This is particularly true when an instability of the upper boundary layer is swept downwards with the flow. The amount of viscous dissipation thus changes with time and contributes to the complexity of the time-dependent flow solutions of the compressible models.

A quantitative measure of the importance of viscous dissipation is given by (2), which for the present study takes the form

$$E = \Phi/F_u \doteqdot (d/H_T). \tag{61}$$

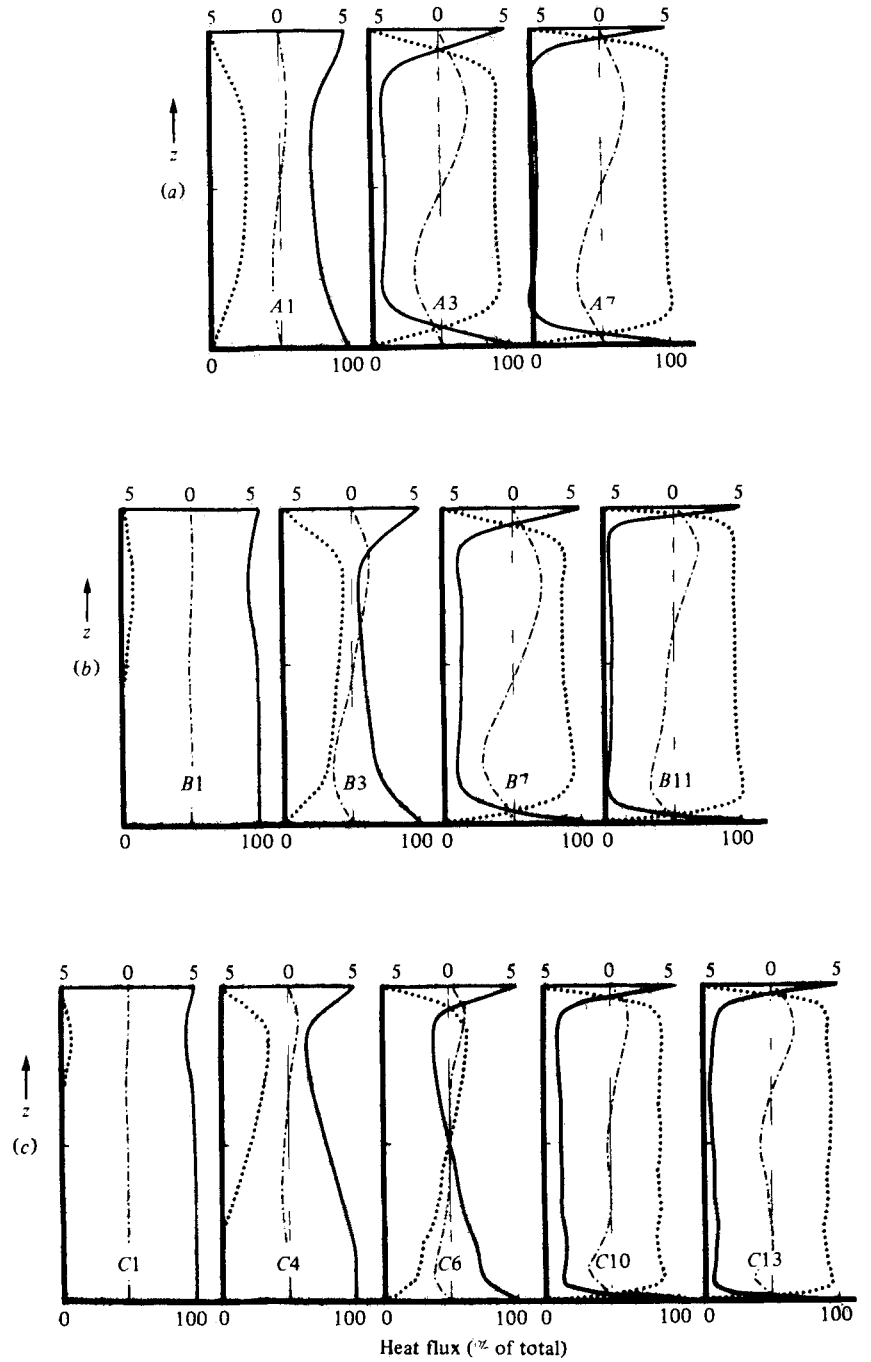

FIGURE 14. Relative contributions to vertical energy flux due to convection (...), conduction (——), and viscous stresses (–·–). The scale for convection and conduction ranges from 0 to 100 % and is indicated at the bottom of each plot. The contribution due to viscous stresses is plotted on an expanded scale ranging from $-5{\cdot}0\,\%$ to $+5{\cdot}0\,\%$ and is displaced to the right such that $0{\cdot}0\,\%$ is centred on each plot. The scale for this contribution is indicated at the top of each graph. (*a*) Series *A* ($d/H_T = 0{\cdot}25$). (*b*) Series *B* ($d/H_T = 0{\cdot}50$). (*c*) Series *C* ($d/H_T = 1{\cdot}00$). R_0 increases from left to right in each series of graphs.

Hewitt *et al.* (1975) proposed this equation for vigorously convecting systems in which most of the heat is carried by convection. The anelastic computations presented above enable a check on the validity of (61) for $d/H_T \leqslant 1{\cdot}50$. For every model the ratio of the global viscous dissipation rate, Φ, to the heat flux out of the upper surface, F_u, was computed at each time step. Running averages of Φ/F_u were also computed. For the steady-state models, Φ/F_u remains constant and F_u is the same as the heat F entering the bottom of the box. In the time-dependent models, the time average of Φ/F_u remains constant when averaged over times long compared to typical periods of oscillation. In figure 15, values of E are plotted against Rayleigh number for all the models of each series, except for those convecting marginally, in which $\Phi \doteqdot 0$. Model $D1$, with $d/H_T = 1{\cdot}50$, and the two anelastic models run in the incompressible limit of $d/H_T = 0{\cdot}117$ are also included in figure 15. Of particular interest is the value of $E = 1{\cdot}30$ plotted for model $D1$; this model provides the first known physical example of a convecting system in which $E > 1{\cdot}00$. This graph provides strong evidence that (61) is valid for $d/H_T \leqslant 1{\cdot}50$. The value of d/H_T appears to be an upper limit which is approached asymptotically by the vigorously convecting systems. Values of E for the low Rayleigh number models fall well below the upper limit because a significant proportion of the total heat flux is conducted along the adiabatic gradients, violating the condition that convection carries the total heat flux across the layer. The verification of (61) by figure 15 confirms that the arguments proposed by Hewitt *et al.* (1975) continue to hold when $d = O(H_T)$.

The model solutions presented above depend on the five dimensionless parameters D, κ_0, F, Γ and T_0 [see $(A1)$–$(A4)$ in table 1 and (32)]. D is the compressibility factor d/H_T, κ_0 is the dimensionless thermal diffusivity, F the dimensionless heat flux prescribed at the bottom boundary, Γ Gruneisen's parameter and T_0 the dimensionless temperature of the upper surface. Each model is characterized by its set of five parameters, the values of which are listed in table 8. Γ and T_0 have constant values throughout series A, B and C. The remaining three dimensionless parameters, which vary from model to model, are defined as

$$D = dg\alpha/C_p, \tag{62}$$

$$\kappa_0' = \nu_0\kappa_0/(g\alpha T_1 d^3), \tag{63}$$

and

$$F' = Fd/(\rho_0 C_p \kappa_0 T_1), \tag{64}$$

where we have here reverted to the notation of primed variables for dimensionless quantities and unprimed variables for dimensional quantities.

The model results can be scaled to dimensional values for particular cases by determining the appropriate values of D, κ_0' and F' from the relevant geophysical parameters. Since the temperature scaling factor $T_1 = 1$ °K, and $T_0' = 273$ in every case, model temperatures scale directly (by a factor of 1·0) from numerical values to degrees celsius. The mean temperature of the convecting region is therefore independent of the (dimensional) thermodynamic and geometric variables. (This of course requires that, for a given value of F', F varies as d^{-1}.)

Although the numerical model is too simple to model convection in the Earth's mantle accurately, an interesting example to consider is small-scale convection in the upper 700 km. This enables a direct comparison with the incompressible results of McKenzie *et al.* (1974). In (62)–(64) T_1, ρ_0 and ν_0 are constants, ρ_0 and ν_0 being

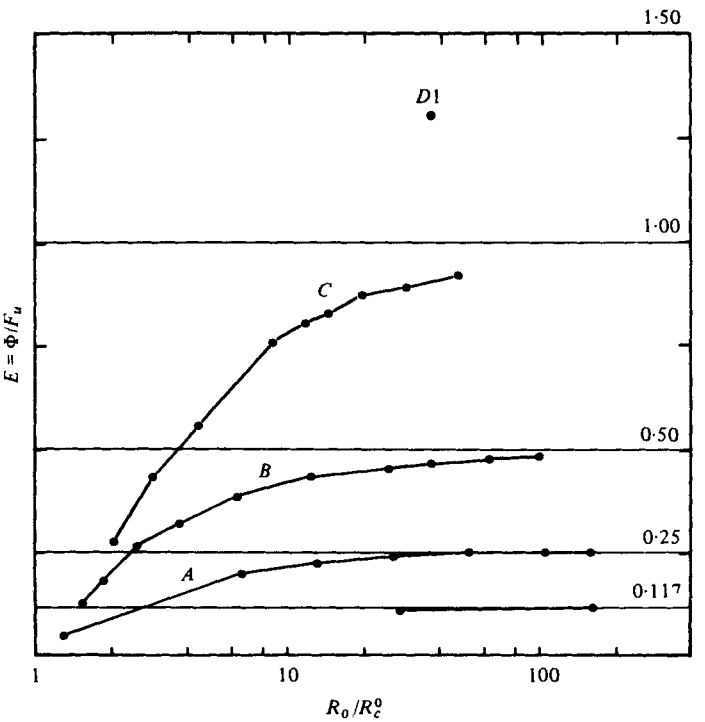

FIGURE 15. Efficiency E ($= \Phi/F_u$) as a function of R_0/R_c^0. Each solid circle represents the value of E computed from one model. The lines labelled A, B and C connect points from models with the same values of d/H_T; the letters indicate the series to which the models belong. Points for the two anelastic models *Bous*1 and *Bous*2 (§ 4.1) are also included. The horizontal lines labelled with values of E indicate the theoretically predicted limit for each series at high values of R_0/R_c^0. Curve A includes models $A1$–$A7$, curve B models $B2$–$B11$, and curve C models $C5$–$C13$.

surface values; in the Earth's mantle g and C_p can also be assumed constant (Birch 1952). The four remaining physical variables are d, α, κ_0 and F. For the upper mantle problem $d = 700$ km. The specification of α therefore determines the compressibility factor D (by 62). Unfortunately, there is considerable uncertainty in choosing an appropriate value of α. Turcotte & Oxburgh (1972) give a table of estimates of α which range from $4{\cdot}7 \times 10^{-5}$ °C^{-1} at the surface to $0{\cdot}9 \times 10^{-5}$ °C^{-1} at a depth of 2600 km. These authors use a value of $3{\cdot}5 \times 10^{-5}$ °C^{-1} in their upper mantle calculations. Peltier (1972) takes $\alpha = 4 \times 10^{-5}$ °C^{-1}, corresponding to pure olivine at high temperature. McKenzie *et al.* (1974) use $\alpha = 2 \times 10^{-5}$ °C^{-1}, the value for the β-spinel phase of olivine at room temperature and pressure, but remark that, at depths where the olivine and spinel phases are in equilibrium, the effective value of α is about 3×10^{-4} °C^{-1}, or an order of magnitude larger than the above values. Finally, Hewitt *et al.* (1975) note that if the upper mantle is everywhere an equilibrium assemblage, as Griggs (1972) has suggested for sinking slabs, then a representative value of α for the upper mantle is 4×10^{-4} °C^{-1}. This uncertainty in α results in a corresponding uncertainty in D (although as discussed in § 1 an estimate of D may be obtained from the density increase across the mantle). For the purposes of the following discussion we will therefore consider D to be a free parameter.

$C_p = 1{\cdot}2 \times 10^3$ J kg^{-1} °C^{-1}	$g = 10$ m s^{-2}
$\nu_0 = 2 \times 10^{17}$ m^2 s^{-1}	$\kappa_0 = 1{\cdot}5 \times 10^{-6}$ m^2 s^{-1}
$\rho_0 = 3{\cdot}7 \times 10^3$ kg m^{-3}	$T_1 = 1$ °K
$d = 7{\cdot}0 \times 10^3$ km	

TABLE 9. Physical and thermodynamic variables

The value of κ_0, like α, is a function of temperature and pressure. However following McKenzie *et al.*, since κ_0 increases with pressure, we take $\kappa_0 = 1{\cdot}5 \times 10^{-6}$ m^2 s^{-1}, an estimated value for the β-spinel phase. The values of κ_0' listed in table 8 were chosen to be consistent with a constant value of κ_0 for all models. In the present example of upper mantle convection in which d is also taken to be the same in every model, the change in κ_0' from series to series arises from the change in α.

Using the values of thermodynamic variables given in table 9 and the dimensionless parameters of table 8, the mean temperature $\overline{T}$ and (dimensional) flux F were determined for each model. These values are plotted in figure 16 on a graph of $\overline{T}$ versus F. Since $\overline{T}$ is a function of both F and D, each series is represented by a separate $\overline{T}$–F curve. The bottom curve, labelled 'incompressible', is the curve for Boussinesq fluids taken from McKenzie *et al.* (1974). The top line, labelled 'conduction', is the locus of mean temperature that would occur in the absence of convection. With the model's constant-flux bottom boundary condition, convection has the effect of reducing the mean temperature of the box. For a given flux, the Boussinesq model convects most vigorously and hence has the lowest mean temperature, since it does not experience the retarding effect of adiabatic gradients. The 'conduction' and 'incompressible' curves on figure 16 thus define the range of all other curves.

The most obvious feature of figure 16 is the increasing effect of adiabatic gradients in retarding the flow as d/H_T increases. For a given value of F, the mean temperature moves closer to the conduction curve as d/H_T increases from series A to C. Since temperature is plotted on a logarithmic scale in figure 16, the Nusselt number may be represented by $N = 10^{\Delta}$, where Δ is proportional to the vertical distance between a $\overline{T}$–F curve and the conduction curve. The reduced vigour of the flow as d/H_T increases thus corresponds to a reduced Nusselt number. The shaded area on figure 16 indicates regions of time-dependent flow. The high-flux ends of the curves are all time dependent and, since time dependence begins at lower values of F as d/H_T increases, increasing d/H_T for a fixed flux F also results in increased time dependence of the flow.

These observations are relevant to the geophysical problem since the surface heat flux has a fixed and relatively well-defined value, whereas the appropriate value of d/H_T is uncertain. The vertical dashed line in figure 16 indicates the mean heat flux at the surface of the Earth ($5{\cdot}85 \times 10^{-2}$ W m^{-2}). The Boussinesq and series A models at this value of F both have steady-state solutions, whereas the series B and C are time dependent. This example shows that if $d = O(H_T)$ the details of upper mantle convection are qualitatively different from those of Boussinesq fluids.

Other interesting features of figure 16 occur at both low and high values of F. A lower bound on the value of F for which convection can occur is the amount of heat conducted down the adiabatic gradient at the upper surface, KT_0/H_T. For a fixed value of d, as d/H_T increases, H_T decreases and the lower bound increases. Accordingly

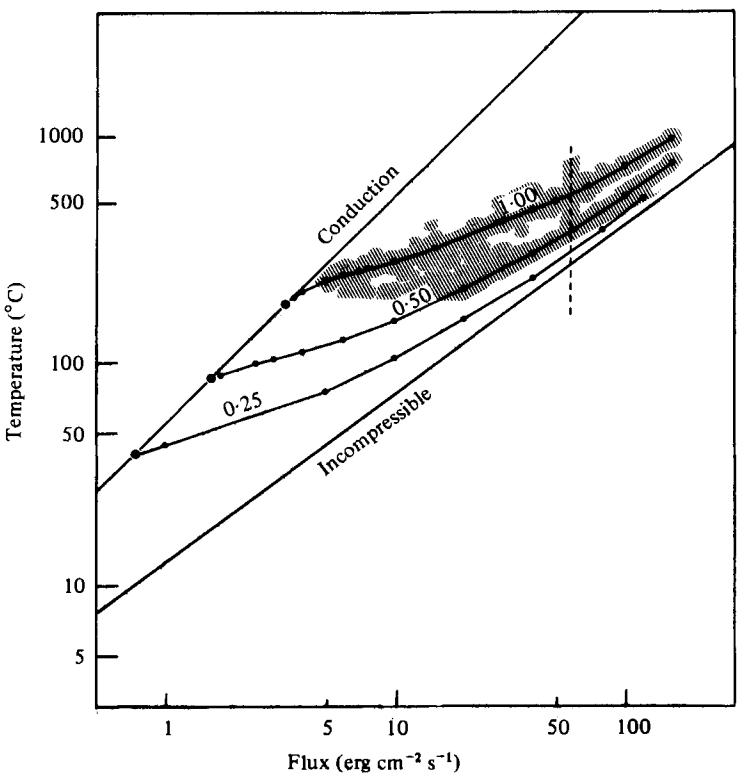

FIGURE 16. Mean temperature as a function of the heat flux which is supplied as a bottom boundary condition. The line labelled 'conduction' indicates the temperatures which would occur in the absence of convection. The line labelled 'incompressible' is taken from the Boussinesq results of McKenzie *et al.* (1974). The large solid circles on the conduction line indicate the critical points for the onset of convection. The small solid circles indicate the mean temperature and bottom heat flux for each model. Points from models with the same value of d/H_T are connected with lines labelled with the appropriate values of d/H_T. All models from each series are included.

the curves for larger d/H_T join the conduction line at higher values of F. Values of the critical flux F_c for the onset of convection, obtained from the linear marginal stability analysis of § 3, show good agreement with the nonlinear model results at low F. A small zone of reversed curvature is apparent at the lowest values of F in the curves of both series B and C. This occurs in the region of penetrative convection solutions.

At high heat flux the curves all tend to parallel the incompressible curve. The flow is sufficiently vigorous for most of the heat to be transported by convection (see figures 14, 15). The boundary-layer arguments of McKenzie *et al.* (1974) will therefore apply and the same power-law dependence results. The fact that the curves do not all overlie each other at high F is due to the adiabatically stratified central region which exists regardless of the vigour of the flow. For a fixed value of F, this effect raises the mean temperature of the box and reduces the Nusselt number, as d/H_T increases. The percentage reduction from series to series however becomes less as F increases and in the limit of very large F would be negligible.

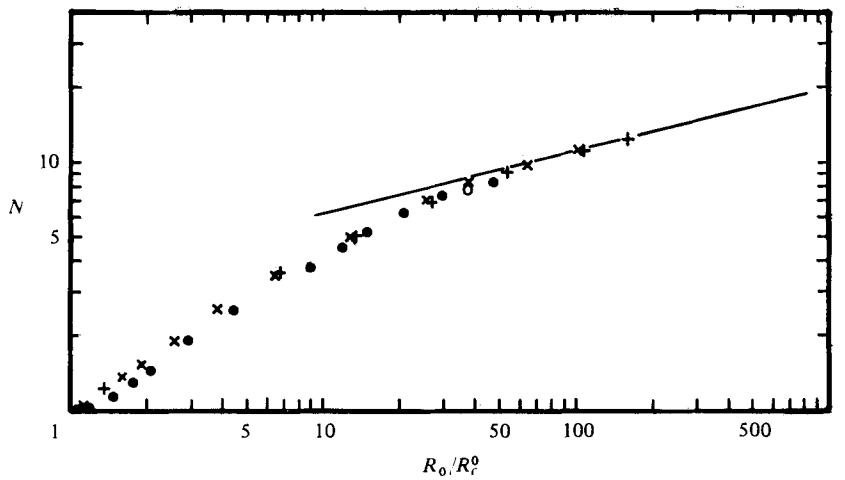

FIGURE 17. Graphs of Nusselt number N, versus R_0/R_c^0, for the three series of models. The symbols identify the series from which each point originates: +, series A; ×, series B; ●, series C; and ○, model $D1$. The straight line has a slope of 0·25 and indicates the power-law behaviour to be expected if $N \propto (R_0/R_c^0)^{\frac{1}{4}}$.

The Nusselt number N, plotted against R_0/R_c^0 for the three series of models, follows similar curves (see figure 17). The point for model $D1$ (with $d/H_T = 1{\cdot}50$) falls on the same curve. The straight line in figure 17 has a slope of 0·25 and indicates the power-law dependence of N on R_0/R_c^0 predicted by the boundary-layer arguments of McKenzie *et al.* (1974). The approach to the predicted power-law behaviour at high values of R_0/R_c^0 is again apparent.

4.3. *Influence of initial conditions and spatial resolution*

The final form of most of the flow solutions presented above are strongly dependent on the initial fields from which they have evolved. The restriction to two dimensions and the fixed lateral extent of the model solutions make it difficult for one regular flow pattern to evolve into another with a different number of rolls. In series B, for example, either one-, two- or three-roll *steady* solutions can be obtained for models $B2$–$B6$. At higher Rayleigh numbers in this series (i.e. models $B7$–$B11$) both single- and multiple-roll solutions become time dependent. Figure 18 shows fluctuations of the mean kinetic energy for both one- and two-roll solutions of model $B9$. Although the upper boundary layers are equally unstable for single- or multiple-roll solutions, the greater separation of descending plumes in the single-roll case allows the instabilities more time to develop. This results in larger pulses of kinetic energy in the single-roll solution as seen in figure 18. In the two-roll solution, smaller parcels of cold liquid breaking away from the upper surface more frequently result in smaller fluctuations.

The solutions of *marginally* convecting models appear to be independent of the initial conditions. For model $B1$ ($R_0/R_c^0 = 1{\cdot}1$) a two-roll-wide pattern evolves regardless of whether the initial flow field is one, two or three rolls wide and regardless of the initial mean temperature. This solution is evidently influenced by both the linear stability and the fixed lateral extent of the box.

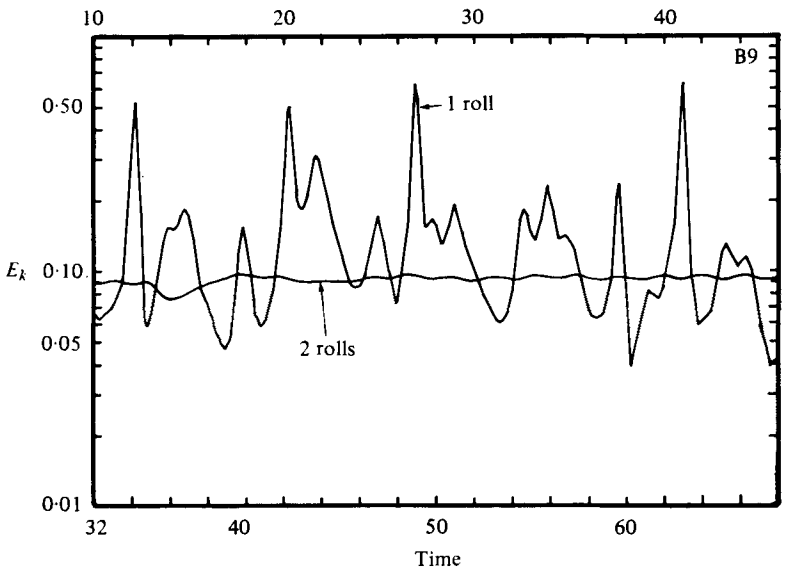

FIGURE 18. A comparison of kinetic energy fluctuations for one-roll and two-roll solutions for model $B9$ ($d/H_T = 0{\cdot}50$; $R_0/R_c^0 = 37{\cdot}8$). Kinetic energy E_k and time t are in dimensionless units. The curve with the large amplitude fluctuations in E_k is from the one-roll solution. The more gently fluctuating curve is from the two-roll solution. The upper and lower time scales refer to the one-roll and two-roll solutions respectively.

Because of the non-uniqueness of the nonlinear solutions, the preferred horizontal scale cannot be determined from the models. However general features such as the increased time dependence as both R_0 and d/H_T increase, and the decrease in horizontal wavelength of the rolls as d/H_T increases, appear to be independent of the initial conditions.

The spatial resolution of the finite-difference mesh also affects the nature of the final solution. In figure 19, kinetic energy is plotted against time for model $B5$ when solved on both coarse (24×24) and fine (48×48) finite-difference grids. On the coarse grid an apparently regular oscillatory solution is obtained. The amplitude of oscillation, however, is gradually diminishing with time. After 316 dimensionless time units the coarse grid solution was interpolated onto the fine grid and then allowed to evolve as shown in figure 19(b). The oscillations die out after a few overturns and a steady one-roll solution evolves. The mean kinetic energy of the oscillatory solution is approximately equal to that of the final steady solution. This difference in behaviour is due to the poorer representation on the coarse grid of short wavelength instabilities developing in the upper boundary layer. Accordingly, the fine grid was used for all models which displayed time-dependent behaviour on the coarse grid, as well as for all models in which fewer than three grid points on the coarse mesh spanned the upper boundary layers (Moore & Weiss 1973).

Although the 48×48 grid is the finest mesh used in most of the models studied, we believe the time dependence obtained at high values of R_0 and d/H_T to be a feature of the physics of compressible flow and not simply a numerical manifestation due to limited spatial resolution. The temporal development of model $C10$, for example

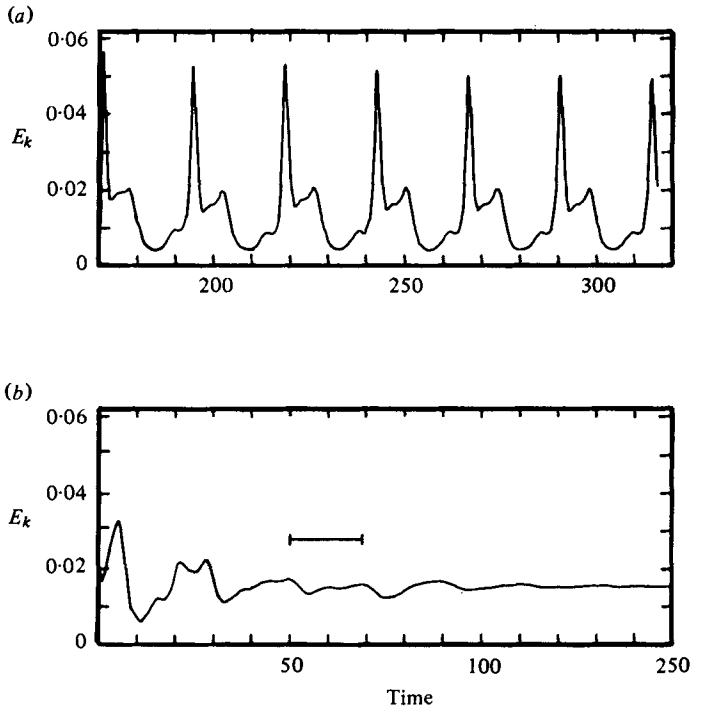

FIGURE 19. A comparison of kinetic energy fluctuations of a single-roll solution for model $B5$ ($d/H_T = 0{\cdot}50$; $R_0/R_c^0 = 3{\cdot}78$) when (a) obtained on a (coarse) 24×24 finite-difference grid, and (b) obtained on a (fine) 48×48 grid. The horizontal bar indicates one overturn time.

(figure 8c), shows no sign of decaying amplitudes of oscillation as was noted above for model $B5$ on the coarse grid. Also, model $D1$, run on a grid with 96 vertical grid points, exhibits the same form of time dependence. Furthermore, the low-Rayleigh-number models of series C (i.e. $C3$–$C6$) which exhibit time-dependent behaviour are convecting very weakly (figure 14) and hence are well resolved on the 48×48 grid. The point of transition from steady to non-steady solutions may be affected by limited resolution but this effect is thought to be small compared to that of the imposed two-dimensionality and side-wall boundaries.

5. Geophysical implications and conclusions

A major drawback of upper mantle convection as a driving mechanism for plate tectonics is the limited scale of plate motion that could be achieved with the preferred aspect ratio of approximately unity (Richter 1973; McKenzie *et al.* 1974). One might think that this problem could be overcome by assuming that convection extends down to the core–mantle boundary; an aspect ratio of one would then allow coherent surface motions over distances of approximately three thousand kilometres. However, both linear and nonlinear analyses above indicate that the aspect ratio of two-dimensional rolls is reduced as the depth of the convection zone is increased. Hence the assumption of mantle-wide convection does not appear to resolve the problem of scale.

Cold plumes descending from gravitationally unstable upper boundary layers dominate the flow solutions. Internal heating in the mantle would accentuate this effect. At high Rayleigh numbers lower boundary layers and rising plumes also occur. However the geometrical effect of decreasing density with height causes rising plumes to expand and dissipate their buoyancy. Thus narrow plumes rising to the surface are not a feature of compressible flow. They appear to be restricted to shallow layers which are at least partially heated from below (McKenzie *et al.* 1974). This suggests that if thermal plumes are responsible for oceanic hot-spots such as the Hawaii–Emperor sea-mount chain, then these plumes cannot have originated at great depths (e.g. the core–mantle boundary), but rather are generated in the upper mantle.

In the model solutions, viscous dissipation is concentrated in narrow vertical zones adjacent to sinking sheets of cold material. There is no evidence of horizontal planes of dissipation as suggested by the one-dimensional shear flow models of Froidevaux & Schubert (1975). Localized kinks in the isotherms, and consequently odd-shaped convection rolls, appear to be the prime effect of viscous dissipation in deep layers. The contribution of horizontally averaged viscous stresses to the total energy flux across the layer [equation (52)] is insignificant for $d/H_T \leqslant 1{\cdot}0$ (figure 14). Consequently the principle (valid for Boussinesq fluids) that the total energy flux at any depth is the sum of conducted plus convected heat flux at that depth, remains approximately true for deep layers with $d/H_T \leqslant 1{\cdot}0$. In particular this will be true for the Earth's mantle and hence details of viscous stress fields can be neglected when constructing thermal models of the Earth.

The influence of density stratification is primarily geometric for the range of values of d/H_T studied. The contraction of descending plumes causes shear heating along the plumes to increase with depth. However since the thermal capacity per unit volume of the fluid also increases with depth, there is no strong depth dependence of the effects of viscous heating on temperature (see figure 13*d* for example). The linear analysis of § 3 indicates that density stratification does not have a significant stabilizing influence when $d/H_T \leqslant 1{\cdot}0$. At $d/H_T = 3{\cdot}0$, however, the density variation introduces a high degree of stability (table 6). This result indicates that, although relevant to the Earth's mantle (for which $d/H_T \leqslant 1{\cdot}0$), the conclusions of this study may not be valid for layers for which $d/H_T \gg 1{\cdot}0$.

The linear results suggest that there is a new regime of flow at values of $d/H_T > 1{\cdot}0$. The flow solutions of model *D*1 at $d/H_T = 1{\cdot}50$ also support this suggestion. Figure 20 shows a typical view of the time-dependent solution for this model. Unlike any of the series *A* to *C* models, several rolls occur stacked one upon the other. Cold parcels of fluid breaking away from the upper boundary layer fall alternately down the left- and right-hand edges of the box, generating rolls with opposite sense of rotation. The cold liquid descends in individual parcels rather than forming continuous plumes, and the entire flow pattern moves downwards with the cold parcels. Model *D*1 was run primarily to establish the fact that E as given by (61) can be greater than one. The solution was obtained in a narrow (24×96) box in order to minimize computer time. The side walls are very restrictive in this case and it is not clear whether the unique features of this solution would occur in wider boxes. A detailed study of convection in deep layers with $d/H_T > 1{\cdot}00$ would be an interesting subject for future research.

Of the non-Boussinesq features included in the present model, the variation of the

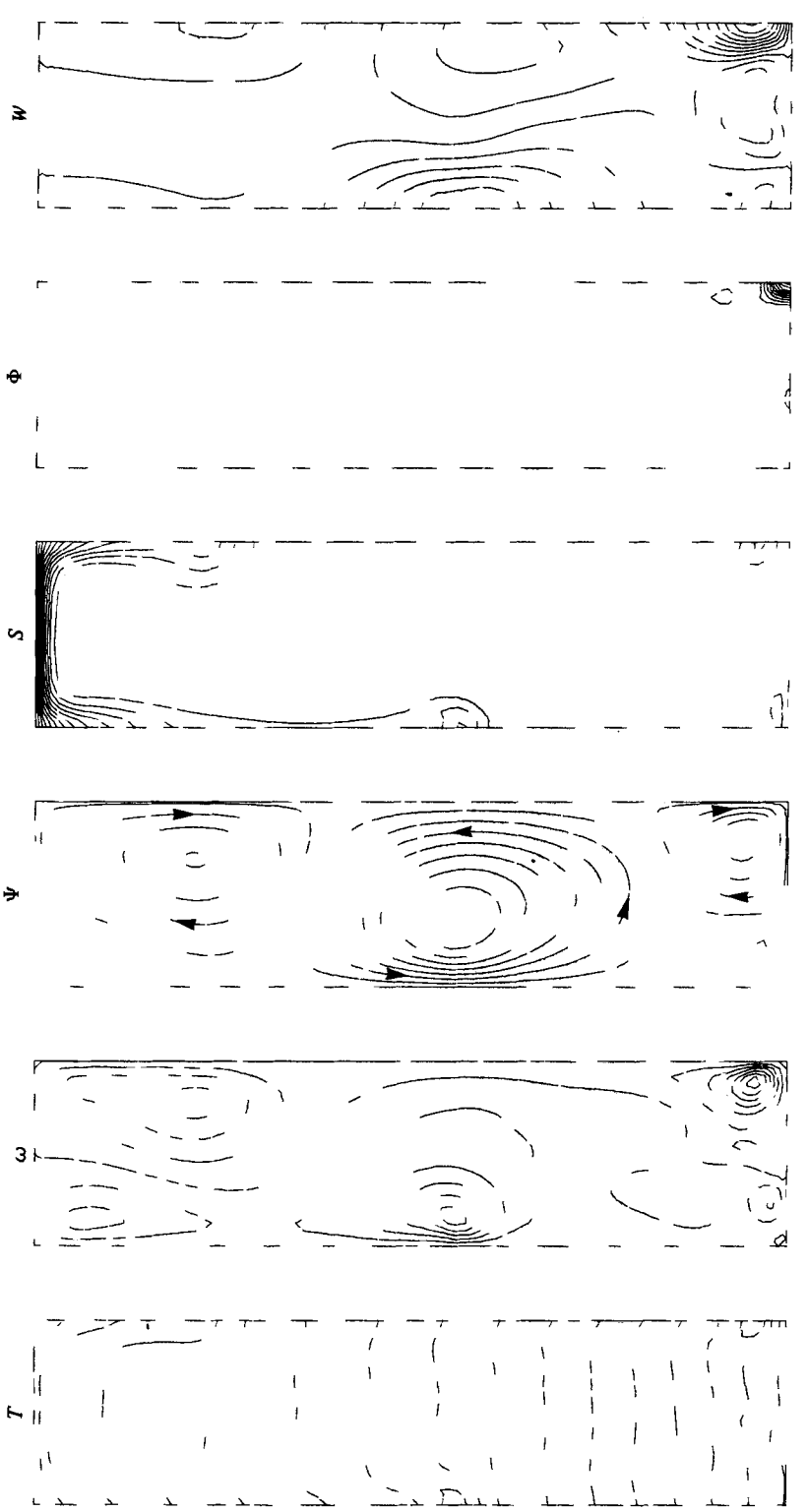

FIGURE 20. Numerical solution of anelastic model *D*1, with $d/H_T = 1{\cdot}50$. Time-dependent solution obtained on a 24×96 finite-difference grid. Contours plot dimensionless temperature T, vorticity ω, stream function ψ, entropy S, rate of viscous dissipation Φ, and vertically convected heat flux W. Contours: T, 0 (203·5) 3052·5; ω, −8·70 (1·74) 12·18; ψ, −0·00926 (0·00136) 0·00433; S, 0 (0·0815) 0·978; Φ, 0 (17·1) 171; W, −2565 (285) 570. Values in parentheses indicate contour intervals.

adiabatic gradient has the dominant effect on the character of the flow. Viscous dissipation and density stratification appear to affect only details of the two-dimensional flow structure, while the decrease in magnitude of the adiabatic gradient with height acts as an internal source of buoyancy.

This study has shown time dependence to be a common feature of convection in deep layers. The balance between dissipated heat and work done against the adiabatic gradient is nevertheless preserved. A consequence of this balance is that at high values of the ratio R_0/R_c^0 the compressible flow obeys the same power laws as incompressible flow. Finally the theoretical prediction of (2) is verified by these numerical experiments for $d = O(H_T)$.

We thank N. O. Weiss for many helpful discussions, and B. Parsons and F. Richter for their comments and suggestions. We also are grateful to D. R. Moore for the use of his subroutine for solving Poisson's equation. This work was carried out while one of us (G.J.) was supported by a Commonwealth Scholarship for postgraduate studies, and represents a part of a continuing study of mantle convection supported by NERC.

Appendix A. Numerical solutions of linear equations

A modified version of the numerical scheme developed by Skilbeck (1976) to investigate the stability of steady basic states was used. The sixth-order set of linear equations [equations (43)–(45)] is replaced by a set of six simultaneous first-order ordinary differential equations. Defining a 6-component vector $\mathbf{f}$ as

$$\mathbf{f}(z) = [\theta(z), U(z), W(z), X(z)\ Y(z), Z(z)]^{\mathrm{T}}, \tag{65}$$

where $X = d_z\theta$, $Y = d_z U$ and $Z = d_z Y$, we can write

$$d_z\mathbf{f} = \mathbf{A}\mathbf{f}, \tag{66}$$

where $\mathbf{A}$ is a coefficient matrix given by

$$\mathbf{A} = \begin{bmatrix} 0 & 0 & 0 & 1 & 0 & 0 \\ 0 & 0 & 0 & 0 & 1 & 0 \\ 0 & -ik & D/\Gamma & 0 & 0 & 0 \\ (\rho\sigma/\kappa_0 + k^2) & 0 & \rho\kappa_0^{-1}\{-\beta_0 + D[T_0 + (1-z)\beta_0]\} & 0 & 0 & 0 \\ 0 & 0 & 0 & 0 & 0 & 1 \\ ik\rho & 2k^2 D/\Gamma & ik(\tfrac{2}{3}(D/\Gamma)^2 - k^2) & 0 & 2k^2 & -D/\Gamma \end{bmatrix}. \tag{67}$$

A 6×6 propagator matrix for (66), $\mathbf{P}(z; z_0)$, must satisfy

$$d_z\mathbf{P} = \mathbf{A}\mathbf{P} \tag{68}$$

and

$$\mathbf{P}(z_0; z_0) = \mathbf{I}_6, \tag{69}$$

where z_0 is the z co-ordinate of one boundary and $\mathbf{I}_6$ is the 6×6 identity matrix. Given matrix $\mathbf{A}$ and the appropriate boundary conditions, (68) is solved for $\mathbf{P}(z; z_0)$, from which $\mathbf{f}(z)$ is determined as

$$\mathbf{f}(z) = \mathbf{P}(z; z_0)\,\mathbf{f}(z_0). \tag{70}$$

From (70) the boundary conditions at $z = z_1$ can be written as

$$\left.\begin{aligned} 0 &= P^*_{11} f_1(z_0) + P^*_{12} f_2(z_0) + P^*_{16} f_6(z_0), \\ 0 &= P^*_{31} f_1(z_0) + P^*_{32} f_2(z_0) + P^*_{36} f_6(z_0), \\ 0 &= P^*_{51} f_1(z_0) + P^*_{52} f_2(z_0) + P^*_{56} f_6(z_0), \end{aligned}\right\} \tag{71}$$

where P^*_{ij} has been written for $P_{ij}(z_1; z_0)$ and f_i is the ith component of f. The system of equations (71) has non-trivial solutions for $f_1(z_0)$, $f_2(z_0)$ and $f_6(z_0)$ only if the determinant of the coefficients is zero; that is, if

$$\begin{vmatrix} P^*_{11} & P^*_{12} & P^*_{16} \\ P^*_{31} & P^*_{32} & P^*_{36} \\ P^*_{51} & P^*_{52} & P^*_{56} \end{vmatrix} = 0. \tag{72}$$

Different boundary conditions require different minors of $\mathbf{P}^*$ to vanish.

Numerical solutions of $\mathbf{P}$ were obtained from (68) using a Runge–Kutta–Gill procedure (Romanelli 1960); the number of spatial increments varied from a minimum of 25, at small values of D, to a maximum of 200 at large D. For given values of β_0, k, D, Γ, T_0 and κ_0, the numerical scheme searches for values of σ for which the matrix $\mathbf{P}^*$, generated by propagating the identity matrix from $z = z_0$ to $z = z_1$ [via equation (68)] satisfies the condition (72).

Appendix B. Numerical solution of the non-linear equations

Equation ($A1$) shows that vorticity is generated by horizontal gradients of temperature and [recalling (28)] pressure, the importance of the pressure gradient increasing with D. Since calculation of the horizontal pressure gradients requires a prior knowledge of the velocity field, ($A1$) and ($A2$) are solved in an iterative manner. A first estimate of ω is obtained from a truncated version of ($A1$),

$$\nabla^2 \omega = \rho_r \partial T / \partial x. \tag{$A1$)'}$$

Using ($A1$)' and ($A2$) an approximate solution of ψ (and hence of $\mathbf{u}$) is obtained from which a first estimate of the pressure gradients is computed. This estimate is substituted into the right-hand side of ($A1$) and new values of ω, ψ and $\mathbf{u}$ computed. This iterative cycle continues until the r.m.s. (root-mean-square) value of two successive estimates of $\psi(x, z)$ converge to within 1 %. (Two iterative cycles are required to obtain 1 % convergence; three cycles give 0·1 % convergence.)

From initial model solutions we found that the r.m.s. value of $\partial P_1/\partial x$ was at least two orders of magnitude less than the r.m.s. value of $\partial T/\partial x$ in every case. We therefore assume that the overall effect of horizontal pressure gradients on ω, and ultimately on $\mathbf{u}$, is small and replace ($A1$) with ($A1$)'. This simplifies the mathematics and results in considerable savings of computer resources, but can only be justified *a posteriori*. The ratio of the r.m.s. values of $\partial P_1/\partial x$ and $\partial T/\partial x$ is largest for the high-Rayleigh-number models at the largest value of D (1·00), but even when models $C10$ and $C11$ (see § 4.2) were advanced a further 200 time steps with the pressure term included and compared with the solutions obtained without it, differences in mean temperature and kinetic energy were found to be less than 1 % and 5 % respectively. However for model $C12$, which is close to the limits of resolution of the numerical scheme, the

inclusion of the additional term in $(A1)$ and the iteration cycle led to a numerical instability which became apparent after approximately 75 additional time steps. The solution of this model had previously remained stable for 5500 time steps. The validity of the assumption that $\partial P_1/\partial x$ may be ignored is therefore in some doubt for this model, and for models $C13$ and $D1$, which have higher Rayleigh numbers still. For all other models the assumption is justified. The linear analysis of § 3 was also repeated using $(A1)'$ rather than $(A1)$. The two sets of results differ by less than 0·03 % at $D = 1{\cdot}00$ and less still at lower values of D.

Equations $(A1)$ or $(A1)'$, $(A2)$, $(A3)$ and $(A4)$ are solved using the finite-difference methods described by Moore, Peckover & Weiss (1974). A staggered two-dimensional finite-difference mesh with equal spatial increments $\Delta x = \Delta z = h$ and temporal increment Δt was used. Points on the mesh have co-ordinates $x_j = jh$, $z_k = kh$ and

$$t^n = \sum_{i=1}^{n} \Delta t_i,$$

for integer values of j and k ($\geqslant 0$) and $n = \frac{1}{2}m$ for integer values of m ($\geqslant 0$). Values of the variables T, ω, ψ and $\mathbf{u}$ at points on the mesh are written in the notation $T^n_{j,k} = T(x_j, z_k, t^n)$. Thus the finite-difference analogue of $(A3)$ is

$$\begin{aligned}
T^{n+1}_{j,k} = T^n_{j,k} + \frac{\Delta t}{4(h^2+2\kappa\Delta t)}\frac{1}{\rho_k}\Big[\Big[& e^{D/\Gamma}\{(\psi^{n+\frac12}_{j+1,k-1} - \psi^{n+\frac12}_{j-1,k-1})\,T^{n+\frac12}_{j,k-1} \\
& - (\psi^{n+\frac12}_{j+1,k-1} - \psi^{n+\frac12}_{j+1,k+1})\,T^{n+\frac12}_{j+1,k} - (\psi^{n+\frac12}_{j+1,k+1} - \psi^{n+\frac12}_{j-1,k+1})\,T^{n+\frac12}_{j,k+1} \\
& + (\psi^{n+\frac12}_{j-1,k-1} - \psi^{n+\frac12}_{j-1,k+1})\,T^{n+\frac12}_{j-1,k} - \tfrac12 hD\,e^{D/\Gamma} \\
& \times\{(\psi^{n+\frac12}_{j+1,k-1} - \psi^{n+\frac12}_{j-1,k-1})\,(T^{n+\frac12}_{j,k-1} + T_0) + (\psi^{n+\frac12}_{j+2,k} - \psi^{n+\frac12}_{j,k})\,(T^{n+\frac12}_{j+1,k} + T_0) \\
& + (\psi^{n+\frac12}_{j+1,k+1} - \psi^{n+\frac12}_{j-1,k+1})\,(T^{n+\frac12}_{j,k+1} + T_0) + (\psi^{n+\frac12}_{j,k} - \psi^{n+\frac12}_{j-2,k})\,(T^{n+\frac12}_{j-1,k} + T_0)\} \\
& + 4\kappa_0(T^{n+\frac12}_{j,k+1} + T^{n+\frac12}_{j,k-1} + T^{n+\frac12}_{j+1,k} + T^{n+\frac12}_{j-1,k} - 4T^n_{j,k}) + 4h^2 e_0 \\
& + \frac{1}{h^2}e^{2khD/\Gamma}\left\{\left[(\psi^{n+\frac12}_{j+1,k+1} - \psi^{n+\frac12}_{j-1,k+1} - \psi^{n+\frac12}_{j+1,k-1} + \psi^{n+\frac12}_{j-1,k-1}) + \frac{Dh}{\Gamma}(\psi^{n+\frac12}_{j+1,k} - \psi^{n+\frac12}_{j-1,k})\right]^2\right. \\
& + \left[2(\psi^{n+\frac12}_{j+1,k} + \psi^{n+\frac12}_{j-1,k} - \psi^{n+\frac12}_{j,k+1} - \psi^{n+\frac12}_{j,k-1}) + \frac{Dh}{\Gamma}(\psi^{n+\frac12}_{j,k+1} - \psi^{n+\frac12}_{j,k-1})\right]^2 \\
& \left.\left. + \frac13\left[\frac{Dh}{\Gamma}(\psi^{n+\frac12}_{j+1,k} - \psi^{n+\frac12}_{j-1,k})\right]^2\right\}\Big]\Big]. \qquad (73)
\end{aligned}$$

Equation (73) is solved to give the temperature at the $(n+1)$th time level. A leap-frog difference scheme is used on the staggered mesh, centred in space and time, with second-order accuracy (Roberts & Weiss 1966). For integral time levels ($n = 0, 1, 2, \ldots$), $T^n_{j,k}$ is only defined at points with $j+k$ even (grid A); at intermediate times

$$(n = \tfrac12, \tfrac32, \ldots),$$

$T^n_{j,k}$ is defined on the interlocking mesh points with $j+k$ odd (grid B). Thus if T is known at time levels n and $n+\frac12$, and ψ is known at mesh points on both interlocking grids, A and B, at time level $n+\frac12$, then $T^{n+1}_{j,k}$ can be computed from (73). Unlike the equation used by Roberts & Weiss, $(A3)$ cannot be written in conservative form and hence (73) is likely to be less accurate than the corresponding Boussinesq expression.

Equations $(A1)'$ and $(A2)$ in implicit finite-difference form become

$$\omega_{j+1,k+1}+\omega_{j+1,k-1}+\omega_{j-1,k-1}+\omega_{j-1,k+1}-4\omega_{j,k} = h(T_{j+1,k}-T_{j-1,k})\,e^{(1-kh)D/\Gamma} \quad (74)$$

and

$$\psi_{j+1,k+1}+\psi_{j+1,k-1}+\psi_{j-1,k-1}+\psi_{j-1,k+1}-4\psi_{j,k} = -2h^2\omega_{j,k}e^{-khD/\Gamma}-Dh(\psi_{j,k+1}-\psi_{j,k-1})/\Gamma. \quad (75)$$

The time level superscript is dropped in these two equations since all values are at the same time level. Equation (74) was solved using an efficient algorithm for solving Poisson's equation, supplied by D. R. Moore and described elsewhere (Moore 1971; Moore *et al.* 1974), which uses fast Fourier analysis in the x direction and tri-diagonal elimination in the z direction. If T is known on grid A, the solution of (74) gives values of ω on grid B (only). When $(A1)$ is approximated, an additional term $P_{j,k}$ is added to the right-hand side of (74) on the second and successive cycles of the ω–ψ–**u** iteration described above. $P_{j,k}$ is the pressure gradient term and is represented as

$$\begin{aligned}P_{j,k} = \frac{D}{\Gamma}e^{zD/\Gamma}\Big\{&\frac{1}{2h^3}[(\psi_{j+1,k+1}-\psi_{j+1,k-1})-2(\psi_{j,k+1}-\psi_{j,k-1})+(\psi_{j-1,k+1}-\psi_{j-1,k-1})]\\ &-\frac{D}{3\Gamma h^2}(\psi_{j+1,k}-2\psi_{j,k}+\psi_{j-1,k})+\frac{1}{2h^3}[(\psi_{j,k+2}-\psi_{j,k-2})-2(\psi_{j,k+1}-\psi_{j,k-1})]\\ &+\frac{2D}{\Gamma h^2}(\psi_{j,k+1}-2\psi_{j,k}+\psi_{j,k-1})+\frac{1}{2h}(D/\Gamma)^2(\psi_{j,k+1}-\psi_{j,k-1})\Big\}. \quad (76)\end{aligned}$$

Equation (75) was solved by an iterative procedure. Initially ignoring the second term on the right-hand side of (75) gives a first estimate, $\psi^{(1)}$, on grid B. $\psi^{(1)}$ is then interpolated onto grid A with a fourth-order interpolation formula

$$\psi_{j,k} = \tfrac{1}{4}(\psi_{j+1,k}+\psi_{j-1,k}+\psi_{j,k+1}+\psi_{j,k-1})-\tfrac{1}{32}(\omega^*_{j+1,k}+\omega^*_{j-1,k}+\omega^*_{j,k+1}+\omega^*_{j,k-1}) \quad (77)$$

derived from $(A2)$, where ω^* represents the version of the right-hand side of (75) used to compute ψ. Then the second term on the right of (75) can be computed and a second estimate $\psi^{(2)}$ obtained. This procedure is continued until the RMS values of $\psi^{(n)}$ and $\psi^{(n-1)}$ converge to within 1 %.

Finally, velocity components u and w are determined from ψ as

$$\left.\begin{aligned}u &= -e^{khD/\Gamma}(\psi_{j,k+1}-\psi_{j,k-1})/2h,\\ w &= e^{khD/\Gamma}(\psi_{j+1,k}-\psi_{j-1,k})/2h.\end{aligned}\right\} \quad (78)$$

The velocities computed from (78) govern the time step, Δt, used to advance the temperature field. To ensure that the finite-difference representation of the advective terms in (73) is stable we impose the Courant–Friedrich–Lewy criterion

$$\Delta t \leqslant h/\max(|u|_{\max}, |w|_{\max}) \quad (79)$$

(Roberts & Weiss 1966), where $|u|_{\max}$ and $|w|_{\max}$ are the largest absolute values of u and w computed at the current time step. We also impose the condition

$$\Delta t \leqslant 0{\cdot}5h^2/\kappa_0 \quad (80)$$

to ensure accuracy of the Dufort–Frankel representation of the diffusion terms in (73). In practice (79) is generally the more stringent condition. In the time-dependent solutions Δt changes continuously to resolve details of the flow.

REFERENCES

BACKUS, G. E. 1975 Gross thermodynamics of heat engines in the deep interior of the Earth. *Proc. Nat. Acad. Sci. U.S.A.* **72**, 1555–1558.

BÉNARD, M. H. 1901 Les tourbillons cellulaires dans une nappe liquide transportant de la chaleur par convection en régime permanent. *Anns Chim. Phys.* 7e série, XXIII, 62–144.

BIRCH, F. 1952 Elasticity and constitution of the Earth's interior. *J. geophys. Res.* **57**, 227–286.

BOUSSINESQ, J. 1903 *Théorie analytique de la Chaleur mise en Harmonie avec la Thermodynamique et avec la Théorie mécanique de la Lumière*, tome II, pp. 157–176. Paris: Gauthier-Villars.

BUSSE, F. H. 1967 On the stability of two-dimensional convection in a layer heated from below. *J. Math. & Phys.* **46**, 140–150.

BUSSE, F. H. 1971 Stability regions of cellular fluid flow. *Proc. IUTAM Symp., Herrenalb*, 1969. In *Instability of Continuous Systems* (ed. H. Leipholz), pp 41–47. Springer.

CHANDRASEKHAR, S. 1961 *Hydrodynamic and Hydromagnetic Stability*. Clarendon.

CLEVER, R. M. & BUSSE, F. H. 1974 Transition to time-dependent convection. *J. Fluid Mech.* **65**, 625–645.

FROIDEVAUX, C. & SCHUBERT, G. 1975 Plate motion and structure of the continental asthenosphere: a realistic model of the upper mantle. *J. Geophys. Res.* **80**, 2553–2564.

GILBERT, F. & BACKUS, G. E. 1966 Propagator matrices in elastic wave and vibrator problems. *Geophys.* **31**, 326–332.

GOUGH, D. O. 1969 The anelastic approximation for thermal convection. *J. Atmos. Sci.* **26**, 448-456

GRAHAM, E. 1975 Numerical simulation of two-dimensional compressible convection. *J. Fluid Mech.* **70**, 689–703.

GRIGGS, D. T. 1972 The sinking lithosphere and the focal mechanism of deep earthquakes. In *The Nature of the Solid Earth* (ed. E. C. Robertson), pp. 361–384. McGraw-Hill.

HEWITT, J. M., MCKENZIE, D. P. & WEISS, N. O. 1975 Dissipative heating in convective flows. *J. Fluid Mech.* **68**, 721–738.

HOWARD, L. N. 1966 Convection at high Rayleigh numbers. In *Proc. 11th Int. Cong. Appl. Mech., Munich*, 1964 (ed. H. Görtler), pp. 1109–1115. Springer.

JEFFREYS, H. 1926 On the stability of a layer of fluid heated below. *Phil. Mag.* VII, **2**, 833-844.

JEFFREYS, H. 1928 Some cases of instability in fluid motion. *Proc. Roy. Soc.* A **118**, 195–208.

JEFFREYS, H. 1930 The instability of a compressible fluid heated below. *Proc. Cam. Phil. Soc.* **26**, 170–172.

LANDAU, L. D. & LIFSHITZ, E. M. 1959 *Fluid Mechanics*. Pergamon.

LOW, A. R. 1929 On the criterion for stability of a layer of viscous fluid heated from below. *Proc. Roy. Soc.* A **125**, 180–195.

MCKENZIE, D. P., ROBERTS, J. M. & WEISS, N. O. 1974 Convection in the Earth's mantle: towards a numerical simulation. *J. Fluid Mech.* **62**, 465–538.

MCKENZIE, D. P. & WEISS, N. O. 1975 Speculations on the thermal and tectonic history of the Earth. *Geophys. J. Roy. Astr. Soc.* **42**, 131–174.

MALKUS, W. V. R. 1964 Boussinesq equations. *Geophys. Fluid Dynamics, Woods Hole Oceanographic Institute Rep.* no. 64–46.

MALKUS, W. V. R. 1973 Convection at the melting point: a thermal history of the Earth's core. *Geophys. Fluid Mech.* **4**, 267–278.

MIHALJAN, J. M. 1962 A rigorous exposition of the Boussinesq approximations applicable to a thin layer of fluid. *Astrophys. J.* **136**, 1126–1133.

MOORE, D. R. 1971 Numerical investigation of astrophysical convection. Ph.D. thesis, University of Cambridge.

MOORE, D. R., PECKOVER, R. S. & WEISS, N. O. 1974 Difference methods for time-dependent two-dimensional convection. *Comp. Phys. Commun.* **6**, 198–220.

MOORE, D. R. & WEISS, N. O. 1973 Two-dimensional Rayleigh–Bénard convection. *J. Fluid Mech.* **58**, 289-312.

OGURA, Y. & PHILLIPS, N. A. 1962 Scale analysis of deep and shallow convection in the atmosphere. *J. Atmos. Sci.* **19**, 173–179.

PELLEW, A. & SOUTHWELL, R. V. 1940 On maintained convective motion in a fluid heated from below. *Proc. Roy. Soc.* A **176**, 312–343.

PELTIER, W. R. 1972 Penetrative convection in the planetary mantle. *Geophys. Fluid Dyn.* **5**, 47–88.

PRESS, F. 1970 Earth models consistent with geophysical data. *Phys. Earth & Planet. Interiors*, **3**, 3–22.

RAYLEIGH, LORD 1916 On convection currents in a horizontal layer of fluid when the higher temperature is on the under side. *Phil. Mag.* VI, **32**, 529–546.

RICHTER, F. M. 1973 Dynamical models for sea floor spreading. *Rev. Geophys. & Space Phys.* **11**, 223–287.

ROBERTS, K. V. & WEISS, N. O. 1966 Convective difference schemes. *Math. Comput.* **20**, 272–299.

ROMANELLI, M. J. 1960 Runge-Kutta methods for the solution of ordinary differential equations. In *Mathematical Methods for Digital Computers* (ed. A. Ralston & H. S. Wilf), pp. 110–120. Wiley.

SCHLÜTER, A., LORTZ, D. & BUSSE, F. 1965 On the stability of steady finite amplitude convection. *J. Fluid Mech.* **23**, 129–144.

SCHMIDT, R. J. & MILVERTON, S. W. 1935 On the instability of a fluid when heated from below. *Proc. Roy. Soc.* A **152**, 586–594.

SCHMIDT, R. J. & SAUNDERS, O. J. 1938 On the motion of a fluid heated from below. *Proc. Roy. Soc.* A **165**, 216–228.

SKILBECK, J. M. 1976 The stability of mantle convection. Ph.D. thesis, University of Cambridge.

SPIEGEL, E. A. 1971 Convection in stars. I. Basic Boussinesq convection. *A. Rev. Astron. & Astrophys.* **9**, 323–352.

SPIEGEL, E. A. & VERONIS, G. 1960 On the Boussinesq approximation for a compressible fluid. *Astrophys. J.* **131**, 442–447.

STRAUS, J. M. 1972 Finite amplitude doubly diffusive convection. *J. Fluid Mech.* **56**, 353–374.

TURCOTTE, D. L., HSUI, A. T., TORRANCE, K. H. & SCHUBERT, G. 1974 Influence of viscous dissipation on Bénard convection. *J. Fluid Mech.* **64**, 369–374.

TURCOTTE, D. L. & OXBURGH, E. R. 1972 Mantle convection and the new global tectonics. *Ann. Rev. Fluid Mech.* **4**, 33–68.